Plasmonic Nanocatalysts for Sustainable Energy Conversion

Yicui Kang

Munich, 2025

Plasmonic Nanocatalysts for Sustainable Energy Conversion

Yicui Kang

Dissertation
to obtain the doctoral degree of natural sciences (Dr. rer. nat.)
at the Faculty of Physics
of the Ludwig–Maximilians–Universität München

submitted by
Yicui Kang

München, den 27/01/2025

First referee: Prof. Dr. Emiliano Cortés

Second referee: Prof. Dr. Barbara A. J. Lechner

Date of oral examination: 11/03/2025

Plasmonische Nanokatalysatoren für nachhaltige Energieumwandlung

Yicui Kang

Dissertation
zur Erlangung des Doktorgrades der Naturwissenschaften (Dr. rer. nat.)
an der Fakultät fur Physik
der Ludwig-Maximilians-Universität
München

vorgelegt von
Yicui Kang

München, den 27/01/2025

Erstgutachter: Prof. Dr. Emiliano Cortés

Zweitgutachter: Prof. Dr. Barbara A. J. Lechner

Tag der mündlichen Prüfung: 11/03/2025

Contents

List of Figures

Publications, Conferences, and Awards

Publications Included in This Dissertation

Kang, Y., João, S.M., Lin, R., Liu, K., Zhu, L., Fu, J., Cheong, W.C., Lee, S., Frank, K., Nickel, B., Liu, M., Lischner, J., Cortés, E. Effect of Crystal Facets in Plasmonic Catalysis. **Nature Communications**, 2024, 15(1), 3923.

Kang, Y., Tan, Y., Tian, W., Zhang, H., Wang, J., Kammerer, D., Akkerman, Q., Fan, C., Zhu, L., Fu, J., Liu, M., Cortés, E. Plasmon-Boosted Directional Transfer of Photo-Generated Electrons for Improved H_2O_2 Production in Au@TiO_2 Hybrid Systems. **To be submitted**.

Ezendam, S., Herran, M., Nan, L., Gruber, C., **Kang, Y.**, Gröbmeyer, F., Lin, R., Gargiulo, J., Sousa-Castillo, A., Cortés, E. Hybrid Plasmonic Nanomaterials for Hydrogen Generation and Carbon Dioxide Reduction. **ACS Energy Letters**, 2022, 7(2), 778-815.

Additional Publications

Cai, C., Liu, B., Liu, K., Li, P., Fu, J., Wang, Y., Li, W., Tian, C., **Kang, Y.**, Stefancu, A., Li, H., Kao, C.W., Chan, T.S., Lin, Z., Chai, L., Cortés, E., Liu, M. Heteroatoms Induce Localization of the Electric Field and Promote a Wide Potential-Window Selectivity Towards CO in the CO_2 Electroreduction **Angewandte Chemie**, 2022, 134(44), e202212640.

Guan, T., Liang, S., **Kang, Y.**, Pensa, E., Li, D., Liang, W., Liang, Z., Bulut, Y., Reck, K.A., Xiao, T., Guo, R. High-Power Impulse Magnetron Sputter Deposition of Ag on Self-Assembled Au Nanoparticle Arrays at Low-Temperature Dewetting Conditions. **ACS Applied Materials & Interfaces**, 2024, 16(30), 40286-40296.

Wang, J., Liu, K., Liao, W., **Kang, Y.**, Xiao, H., Chen, Y., Wang, Q., Luo, T., Chen, J., Li, H., Chan, T.S., Chen, S., Pensa, E., Chai, L., Liu, F., Jiang, L., Liu, C., Fu, J., Cortés, E., Liu, M. Hole Mobility Enhancement via Metal Vacancies in Semiconductor Oxides for Efficient Photoelectrochemical Water Splitting. **Nature Catalysis**, accepted.

Zhu, L., Liu, K., Huang, J.L., Mei, Z., **Kang, Y.**, Chen, Q., Wang, X., Zhang, H., Zi, X., Wang, Q., Fu, J., Pensa, E., Stefancu, A., Liu, M., Cortés, E. Plasmon-Enhanced C_2H_4 Generation in CO_2 Electroreduction Reaction on a CuPd Catalyst. **To be submitted**.

Conference Presentations

23–26 Sep 2024, Venice – The International e-conversion/CeNS Conference
Poster: "Plasmonic Catalysis: Achieving the Impossible in Conventional Catalysis"

17–22 Mar 2024, Berlin – Deutsche Physikalische Gesellschaft (DPG)
Talk: "Atomic Scale Plasmonic Catalysis"

13–16 Feb 2024, Garmisch-Partenkirchen – The e-conversion Winter Retreat
Poster: "Crystal Facet Effect in Plasmonic Catalysis"

6–9 Mar 2023, Bayrischzell – The e-conversion Winter Retreat
Poster: "Crystal Facet Effect in Plasmon-Assisted Electrocatalytic CO_2RR"

30 Aug – 2 Sep 2022, Munich – The International Nanoscience Students Conference (INASCON)
Short Talk & Poster: "Facet Effect of Au Nanocrystals in Plasmon-Assisted Electrocatalysis"

4–7 Oct 2022, Venice – The International e-conversion Conference
Poster: "The Role of Crystal Facets in Plasmonic Electrocatalytic CO_2 Reduction"

Awards and Grants

2025 – LMU Sustainability Fund
Applicants: Dr. Wenjie Tian, Prof. Dr. Emiliano Cortés, Yicui Kang

2025 – Cambridge-LMU Strategic Partnership Fund
Applicants: Prof. Dr. Emiliano Cortés, Yicui Kang

2023 – E-conversion International Exchange Fund
Applicants: Prof. Dr. Emiliano Cortés, Prof. Dr. Min Liu, Yicui Kang

Zusammenfassung

Die rasante Industrialisierung und technologischen Fortschritte haben das moderne Leben erheblich verändert, aber sie haben auch zu schwerwiegenden Umweltproblemen geführt, darunter übermäßige CO_2-Emissionen, die Abhängigkeit von nicht erneuerbaren fossilen Brennstoffen und die zunehmende Verschmutzung durch Plastikabfälle. Die Bewältigung dieser dringenden Herausforderungen erfordert die Entwicklung nachhaltiger Technologien zur Energieumwandlung. Ein vielversprechender Ansatz besteht darin, Sonnenlicht – eine reichlich vorhandene und erneuerbare Energiequelle – zu nutzen, um katalytische Prozesse anzutreiben, die Schadstoffe in wertvolle Brennstoffe und Chemikalien umwandeln.

Die künstliche Photosynthese, inspiriert von natürlichen Prozessen, bietet einen vielversprechenden Ansatz zur Umwandlung von CO_2 und Wasser in wertvolle Brennstoffe und Chemikalien unter Nutzung erneuerbarer Energie. Dieser Prozess umfasst zentrale Reaktionen wie die Wasserstoffentwicklung (HER) und die CO_2-Reduktion (CO_2RR). Darüber hinaus hat sich Wasserstoffperoxid (H_2O_2) als alternativer Energieträger mit einer Leistungsdichte vergleichbar zu komprimiertem Wasserstoff herausgestellt und bietet eine sicherere und praktikablere Option für Speicherung und Transport. Die photokatalytische Kunststoffreformierung stellt eine weitere innovative Strategie dar, bei der erneuerbare Energie genutzt wird, um gleichzeitig Kunststoffabfälle abzubauen und Wasserstoff zu erzeugen, was eine doppelte Lösung zur Reduzierung der Umweltverschmutzung und zur nachhaltigen Energiegewinnung bietet. Trotz ihres Potenzials stehen diese Methoden jedoch vor erheblichen Herausforderungen, darunter langsame Reaktionskinetik, geringe Umwandlungseffizienz und unzureichende Selektivität, die ihre industrielle Anwendbarkeit einschränken.

Unter den verschiedenen vorgeschlagenen Ansätzen zur Bewältigung dieser Herausforderungen hat die katalytische Nutzung der lokalisierten Oberflächenplasmonenresonanz (LSPR) erhebliches Interesse geweckt. Plasmonische Nanopartikel weisen bemerkenswerte Lichtabsorptionsfähigkeiten über ein breites Wellenlängenspektrum auf und können Sonnenlicht auf der Nanoskala effizient erfassen und umwandeln. Bei Bestrahlung mit resonantem Licht zeigen sie einzigartige Eigenschaften wie verstärkte elektrische Felder, die Erzeugung heißer Ladungsträger und lokalisierte Erwärmungseffekte, die die katalytische Aktivität und Selektivität in verschiedenen Energieumwandlungsprozessen erheblich verbessern können. Darüber hinaus ermöglicht die gezielte Modifikation der Form und Zusammensetzung plasmonischer Nanopartikel eine präzise Steuerung ihrer optischen und katalytischen Eigenschaften. Diese einzigartigen Eigenschaften machen die plasmonische Katalyse zu

einem leistungsstarken Werkzeug, um die Nutzung von Solarenergie über Photovoltaik hinaus zu erweitern und die Herstellung von Solar-Brennstoffen sowie die photokatalytische Reformierung zu ermöglichen. Trotz bedeutender Fortschritte bleibt die katalytische Leistung jedoch suboptimal, und die zugrundeliegenden Mechanismen, die die plasmonunterstützte Katalyse bestimmen, sind noch nicht vollständig verstanden, was weitere Untersuchungen erforderlich macht.

Diese Dissertation untersucht systematisch die Rolle plasmonischer Nanokatalysatoren in der Energieumwandlung unter Berücksichtigung der Materialherstellung, Charakterisierung und katalytischen Leistung. Zunächst werden die theoretischen Grundlagen plasmonischer Phänomene und deren Bedeutung für die Katalyse vorgestellt, gefolgt von einer eingehenden Diskussion über die Synthese und Charakterisierung plasmonischer Nanopartikel. Anschließend werden facettenabhängige Effekte in der plasmonunterstützten Elektrokatalyse für CO_2RR und HER untersucht, um zu zeigen, wie LSPR die Verteilung aktiver Zentren beeinflusst und die Reaktionskinetik verbessert. Danach wird die Rolle von Au@TiO_2-Kern-Schale-Nanostrukturen analysiert, insbesondere hinsichtlich der Verbesserung der Ladungstransfereffizienz und der Steigerung der photokatalytischen H_2O_2-Produktionsrate durch LSPR. Schließlich wird ein neuartiges hybrides Au-FeSA-MCN System für die Kunststoff-Photoreformierung vorgestellt, das plasmonische Nanopartikel mit Einzelatomkatalysatoren kombiniert, um die simultane Kunststoffzerlegung und Wasserstofferzeugung zu ermöglichen.

Insgesamt bietet diese Dissertation eine umfassende Untersuchung plasmonischer Nano-katalysatoren für Energie- und Umweltanwendungen und verbindet grundlegende wissenschaftliche Erkenntnisse mit praktischen Innovationen. Die Ergebnisse unterstreichen das transformative Potenzial der LSPR-unterstützten Katalyse zur Optimierung der Solarenergie-Nutzung für eine nachhaltige Energieumwandlung und bilden die Grundlage für zukünftige Fortschritte in skalierbaren und effizienten photokatalytischen Technologien.

Abstract

Rapid industrialization and technological advancements have dramatically transformed modern life, but they have also led to severe environmental challenges, including excessive CO_2 emissions, dependence on nonrenewable fossil fuels, and escalating plastic waste pollution. Addressing these urgent issues requires the development of sustainable energy conversion technologies. A promising approach is to harness sunlight, an abundant and renewable energy source, to drive catalytic processes that transform pollutants into valuable fuels and chemicals.

Artificial photosynthesis, inspired by natural processes, offers a promising approach by converting CO_2 and water into valuable fuels and chemicals using renewable energy. This process involves key reactions such as hydrogen evolution (HER) and CO_2 reduction (CO_2RR). Additionally, hydrogen peroxide (H_2O_2) has emerged as an alternative energy carrier with a power density comparable to pressurized hydrogen, offering a safer and more practical storage and transportation option. Plastic photoreforming presents another innovative strategy by utilizing renewable energy to simultaneously degrade plastic waste and generate hydrogen, providing a dual-benefit approach to pollution mitigation and clean energy production. However, despite their potential, these methods face significant challenges, including slow reaction kinetics, low conversion efficiency, and poor selectivity, limiting their industrial applicability.

Among the different approaches proposed to address these challenges, localized surface plasmon resonance (LSPR)-assisted catalysis has garnered significant interest. Plasmonic nanoparticles exhibit remarkable light absorption properties across a broad range of wavelengths, efficiently capturing and converting sunlight with a nanoscale. When exposed to resonant light, they exhibit unique properties such as enhanced electric fields, hot carrier generation, and localized heating effects, which can significantly improve catalytic activity and selectivity across various energy conversion processes. Furthermore, the tunability of plasmonic nanoparticles through modifications in shape and composition enables precise control over their optical and catalytic properties. These unique properties position plasmonic catalysis as a powerful tool for extending solar energy utilization beyond photovoltaics, enabling solar fuel production and photocatalytic reforming. However, despite notable progress, catalytic performance remains suboptimal, and the underlying mechanisms governing plasmonic-enhanced catalysis are not yet fully understood, necessitating further investigation.

This thesis systematically explores the role of plasmonic nanocatalysts in energy conversion by addressing material preparation, characterization, and catalytic performance. First, it introduces the theoretical foundations of plasmonic phenomena and their implications in catalysis, followed by an in-depth discussion of the synthesis and characterization of plasmonic nanoparticles. Next, it investigates facet-dependent effects in plasmon-assisted electrocatalysis for CO_2RR and HER, demonstrating how LSPR influences active site distribution and enhances reaction kinetics. The study then explores Au@TiO_2 core-shell nanostructures, elucidating the role of LSPR in improving charge transfer efficiency and boosting photocatalytic H_2O_2 production rates. Finally, the thesis presents a novel hybrid Au-FeSA-MCN system for plastic photoreforming, integrating plasmonic nanoparticles with single-atom catalysts to enable simultaneous plastic degradation and hydrogen generation.

Overall, this thesis provides a comprehensive study on plasmonic nanocatalysts for energy and environmental applications, bridging fundamental insights with practical innovations. The findings highlight the transformative potential of LSPR-assisted catalysis in optimizing solar energy utilization for sustainable energy conversion, laying the foundation for future advancements in scalable and efficient photocatalytic technologies.

1

Introduction

Over the past few decades, our society has experienced remarkable advancements that have greatly enhanced living standards and convenience for people worldwide. However, this rapid progress has come at a steep cost to the environment. Critical challenges such as global warming and climate change, driven by excessive CO_2 emissions, an escalating energy crisis stemming from reliance on nonrenewable fossil fuels, and severe ocean and soil pollution caused by excessive plastic usage, have emerged. These pressing environmental issues demand an urgent transition toward sustainable and renewable development strategies.

In recent years, the concept of carbon neutrality has gained considerable attention. An promising approach to achieve this goal is artificial photosynthesis, which mimics the natural photosynthetic process, converting CO_2 and water into valuable chemicals and fuels using renewable energy under ambient conditions. The process encompasses reactions such as hydrogen evolution reactions (HER), oxygen evolution reactions (OER), and CO_2 reduction reactions (CO_2RR), producing useful products like hydrogen, carbon monoxide (an important feedstock in the chemical industry), methane, ethanol, etc. By transforming CO_2 into usable fuels, this method not only addresses the problem of excessive atmospheric CO_2, but also tackles fossil fuel depletion, creating a dual solution to these interconnected challenges. To be mentioned, hydrogen, as a clean and efficient energy carrier, has garnered significant attention in the field of sustainable energy. However, due to the explosive nature of pure hydrogen, its storage and transportation pose substantial challenges. In this context, hydrogen peroxide (H_2O_2) has emerged as a compelling alternative energy carrier. With a power density comparable to that of pressurized hydrogen, H_2O_2 offers a safer and more practical option, driving increased research interest in its efficient production. Another intriguing solution referred to as "carbon internal cycling," is plastic photoreforming, which couples the degradation of plastic waste with hydrogen generation. By leveraging sunlight or electricity as an energy source, photogenerated holes facilitate the breakdown of plastic waste, while the corresponding electrons participate in hydrogen generation. This innovative approach not only addresses the growing issue of plastic waste but also contributes to advancements in energy conversion technologies. Above mentioned strategies to tackle these environmental challenges involve utilizing sunlight, an abundant and renewable energy source, to drive catalytic reactions that convert pollutants into valuable fuels and chemicals, thus have attracted more and more attention. However, despite the promising potential of these methods, their practical applications face significant challenges, including slow reaction kinetics, low conversion efficiencies, and poor selectivity. These

intertwined limitations have driven substantial research efforts aimed at overcoming these barriers and developing approaches that are industrially feasible.

Among the various strategies to address these challenges, localized surface plasmon resonance (LSPR)-assisted catalysis has attracted considerable attention. Due to their nanoscale dimensions, plasmonic nanoparticles exhibit strong light-matter interactions, allowing them to efficiently capture and convert sunlight across a wide spectral range, including visible light. When plasmonic nanoparticles are exposed to light of a resonant wavelength, their electrons undergo collective oscillations, known as LSPR. In addition to their exceptional optical properties, LSPR-active nanoparticles exhibit enhanced electric fields, hot carrier generation, and localized thermal effects. These attributes have proven advantageous for a range of catalytic processes, including those described earlier, as will be discussed in detail in subsequent chapters. Furthermore, the plasmonic properties of these nanoparticles can be finely tuned by adjusting their size, shape, and composition. This tunability enhances their ability to absorb and concentrate light more properly and effectively, making them highly versatile materials for catalytic applications in energy conversion. More importantly, plasmonic catalysis aims to maximize solar energy utilization beyond traditional photovoltaic applications, extending its impact to solar fuel production and photocatalytic reforming. Despite significant progress in the field of LSPR-enabled catalysis, the mechanisms underlying the improved catalytic performance of plasmonic nanostructures remain insufficiently understood. Bridging this knowledge gap is crucial for the rational design and optimization of plasmonic catalysts. To achieve both high catalytic activity and selectivity, detailed investigations into the interplay of physical and chemical phenomena under LSPR excitation are essential. This thesis investigates the unique capabilities of plasmonic nanocatalysts in energy conversion applications, systematically addressing their synthesis, characterization, and catalytic performance, paving the way for the development of more efficient and robust systems for sustainable energy conversion.

Chapter 2 introduces the theoretical framework, offering an in-depth overview of plasmonic phenomena and their catalytic implications. Given the importance of precise synthesis and thorough characterization, Chapter 3 details methodologies for fabricating plasmonic nanoparticles and advanced techniques used to analyze their optical, chemical, and catalytic properties.

Subsequent chapters delve into specific applications and innovations. Chapter 4 examines facet-dependent catalytic effects in plasmon-assisted electrocatalytic CO_2RR and HER using gold nanoparticles of varying morphologies. This study demonstrates how LSPR transforms active sites from facet-specific regions in pure electrocatalysis to low-coordination sites, significantly enhancing reaction kinetics and selectivity. This finding underscores the fundamental role of LSPR in reshaping catalytic processes.

To address the stability limitations of gold nanoparticles and optimize the utilization of hot charge carriers, Chapter 5 introduces Au@TiO_2 core-shell nanostructures. By coating plasmonic Au nanoparticles with a porous anatase TiO_2 shell, this study explores plasmonic photocatalytic H_2O_2 production in metal-semiconductor hybrid systems. The results highlight the critical role of LSPR in

facilitating directional charge transfer across the metal-semiconductor interface, resulting in higher efficiency in utilizing photo-generated charge carriers and significantly improving H_2O_2 production rates.

Finally, Chapter 6 presents a novel plastic photoreforming process utilizing hybrid plasmonic catalysts, which integrate Au nanoparticles with single-atom catalysts. This innovative approach utilizes photogenerated holes to degrade plastic waste while concurrently employing electrons to produce hydrogen. By coupling these two processes, this strategy offers a dual-function solution to environmental and energy challenges, exemplifying sustainable progress.

In conclusion, this thesis provides a comprehensive exploration of plasmonic nanocatalysts in energy conversion, spanning theoretical insights, material development, and practical applications. The findings emphasize the transformative potential of plasmonic nanostructures in addressing critical challenges in sustainable energy and environmental remediation, while offering guidance for the design of future catalytic systems. These contributions lay a foundation for advancing the field and moving closer to achieving scalable and sustainable energy solutions.

2

Fundamentals of plasmonic nanocatalysts for energy conversion

The content of this chapter is partially based on our review paper published in the scientific journal ACS Energy Letters (Ezendam, S., Herran, M., Nan, L., Gruber, C., Kang, Y., Gröbmeyer, F., Lin, R., Gargiulo, J., Sousa-Castillo, A., Cortés, E. Hybrid Plasmonic Nanomaterials for Hydrogen Generation and Carbon Dioxide Reduction. ACS Energy Letters, 2022, 7(2), 778-815.)[1]. The peer-reviewed manuscript is used, and text elements are drawn from the publication with rephrase in accordance with the ACS Publications that allows the reprinting of own contributions and in accordance with the terms of the Creative Commons CC BY public use license http://creativecommons.org/licenses/by/4.0/. Large language models are used to refine the grammars.

The following chapter establishes the theoretical framework underpinning plasmonic nanocatalysts, providing a solid foundation for understanding their unique properties and catalytic potential. The discussion begins with the fundamental concepts of surface plasmons and localized surface plasmons, which are essential for grasping the mechanisms driving plasmonic catalysis. With the foundational principles introduced, we then illuminate how plasmonic nanostructures interact with light and how to produce remarkable optical and catalytic phenomena.

2.1 Fundamentals of surface plasmon

To begin with, the fundamental principles of surface plasmons and localized surface plasmons, which serve as the cornerstone of this thesis, are introduced. While detailed theoretical discussions can be found in standard textbooks[2], this section aims to present the essential conceptual framework, providing a concise and logical foundation for the subsequent content.

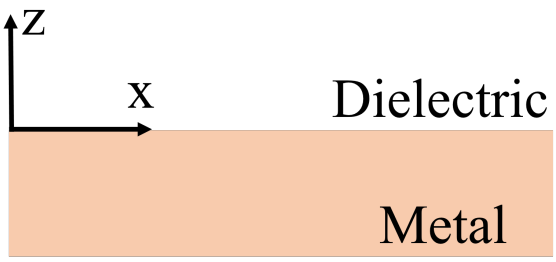

Figure 2.1: Geometry for surface plasmon polaritons propagation at a single interface between a metal and a dielectric. Adapted with permission from Ref [2].

2.1.1 Surface plasmon resonance

The following derivation is based on the clear and comprehensive book from Maier[2], to which the reader is referred for more details.

The foundation of our investigation into the electromagnetic properties of a system begins with Maxwell's equations, which are indispensable for describing electromagnetic phenomena:

$$\begin{aligned} \nabla \cdot \mathbf{D} &= \rho_{\text{ext}}, \\ \nabla \cdot \mathbf{B} &= 0, \\ \nabla \times \mathbf{E} &= -\frac{\partial \mathbf{B}}{\partial t}, \\ \nabla \times \mathbf{H} &= \mathbf{J}_{\text{ext}} + \frac{\partial \mathbf{D}}{\partial t}. \end{aligned} \tag{2.1}$$

Here, $\mathbf{D}$ represents the electric displacement field, $\mathbf{E}$ the electric field, $\mathbf{H}$ the magnetic field, and $\mathbf{B}$ the magnetic flux density. The quantities ρ_{ext} and $\mathbf{J}_{\text{ext}}$ are the external charge and current densities, respectively.

To examine the physical properties of surface plasmon polaritons, we apply Maxwell's equations to the flat interface between a conductor and a dielectric. This analysis is facilitated by reformulating Maxwell's equations into the wave equation, which is broadly applicable to electromagnetic wave propagation. In the absence of external charges and currents, Maxwell's equations reduce to

$$\nabla \left(-\frac{1}{\varepsilon} \mathbf{E} \cdot \nabla \varepsilon \right) - \nabla^2 \mathbf{E} = -\mu_0 \varepsilon_0 \varepsilon \frac{\partial^2 \mathbf{E}}{\partial t^2}. \tag{2.2}$$

For negligible spatial variation of the dielectric profile, $\varepsilon = \varepsilon(\mathbf{r})$, over distances comparable to the optical wavelength, this simplifies to

$$\nabla^2 \mathbf{E} - \frac{\varepsilon}{c^2} \frac{\partial^2 \mathbf{E}}{\partial t^2} = 0. \tag{2.3}$$

To describe confined propagating waves, we assume a harmonic time dependence of the electric field, $\mathbf{E}(\mathbf{r},t) = \mathbf{E}(\mathbf{r})e^{-i\omega t}$, where $k_0 = \omega/c$ is the vacuum wave vector. Substituting this into the wave equation yields the Helmholtz equation:

$$\nabla^2\mathbf{E} + k_0^2\varepsilon\mathbf{E} = 0. \tag{2.4}$$

Assuming a one-dimensional problem where $\varepsilon = \varepsilon(z)$, and setting the x-axis as the propagation direction ($\partial/\partial x = i\beta$ and $\partial/\partial y = 0$), the electric field can be expressed as $\mathbf{E}(x,y,z) = \mathbf{E}(z)e^{i\beta x}$. Substituting into the Helmholtz equation gives

$$\frac{\partial^2\mathbf{E}(z)}{\partial z^2} + \left(k_0^2\varepsilon - \beta^2\right)\mathbf{E}(z) = 0. \tag{2.5}$$

For transverse magnetic (TM) modes, where only E_x, E_z, and H_y are nonzero, the solutions for a single flat interface between a dielectric ($z > 0$) and a conductor ($z < 0$) are:

For $z > 0$:

$$\begin{aligned} H_y(z) &= A_2 e^{i\beta x}e^{-k_2 z}, \\ E_x(z) &= iA_2\frac{k_2}{\omega\varepsilon_0\varepsilon_2}e^{i\beta x}e^{-k_2 z}, \\ E_z(z) &= -A_2\frac{\beta}{\omega\varepsilon_0\varepsilon_2}e^{i\beta x}e^{-k_2 z}. \end{aligned} \tag{2.6}$$

For $z < 0$:

$$\begin{aligned} H_y(z) &= A_1 e^{i\beta x}e^{k_1 z}, \\ E_x(z) &= -iA_1\frac{k_1}{\omega\varepsilon_0\varepsilon_1}e^{i\beta x}e^{k_1 z}, \\ E_z(z) &= -A_1\frac{\beta}{\omega\varepsilon_0\varepsilon_1}e^{i\beta x}e^{k_1 z}. \end{aligned} \tag{2.7}$$

The continuity conditions for H_y and $\varepsilon_i E_z$ at the interface imply $A_1 = A_2$ and $k_2/k_1 = -\varepsilon_2/\varepsilon_1$. Confinement of the wave to the interface requires $\mathrm{Re}[\varepsilon_1] < 0$ when $\varepsilon_2 > 0$, indicating that surface waves exist only at interfaces where the real parts of the dielectric permittivities have opposite signs.

The wave equation further yields the relations:

$$k_1^2 = \beta^2 - k_0^2\varepsilon_1, \quad k_2^2 = \beta^2 - k_0^2\varepsilon_2. \tag{2.8}$$

The dispersion relation for SPPs at the interface is thus:

$$\beta = k_0\sqrt{\frac{\varepsilon_1\varepsilon_2}{\varepsilon_1 + \varepsilon_2}}. \tag{2.9}$$

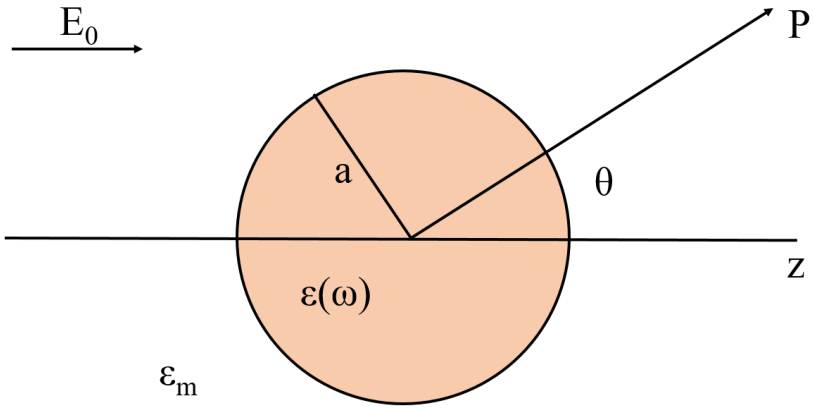

Figure 2.2: Sketch of a homogeneous sphere placed into an electrostatic field. Adapted with permission from Ref [2].

For materials with negligible damping, the SPP frequency approaches the characteristic surface plasmon frequency, $\omega_{sp} = \omega_p/\sqrt{1+\varepsilon_2}$, where $\omega_p^2 = ne^2/(\varepsilon_0 m)$ is the plasma frequency of the free electron gas. In the limit of $\mathrm{Im}[\varepsilon_1(\omega)] \to 0$, the wave vector β diverges as $\omega \to \omega_{sp}$, and the group velocity $v_g \to 0$, resulting in a mode with electrostatic character, termed the surface plasmon.

2.1.2 Localized surface plasmon

When the particle size d is significantly smaller than the wavelength of light in the surrounding medium ($d \ll \lambda$), the electromagnetic field's phase remains nearly uniform across the particle's volume. This allows the spatial distribution of the field to be approximated by solving the electrostatic problem, governed by the Laplace equation for the potential:

$$\nabla^2 \Phi = 0. \tag{2.10}$$

Consider a homogeneous, isotropic sphere of radius a positioned at the origin and placed in a uniform static electric field $\mathbf{E} = E_0 \hat{z}$. The surrounding medium is also isotropic, with a dielectric constant ε_m. Solving the Laplace equation under these conditions yields the potential outside the sphere as

$$\Phi_{out} = -E_0 r \cos\theta + \frac{\mathbf{p}\cdot\mathbf{r}}{4\pi\varepsilon_0\varepsilon_m r^3}, \tag{2.11}$$

where the induced dipole moment $\mathbf{p}$ is given by

$$\mathbf{p} = \varepsilon_0\varepsilon_m \alpha \mathbf{E}_0, \tag{2.12}$$

and the polarizability α of the sphere is

$$\alpha = 4\pi a^3 \frac{\varepsilon - \varepsilon_m}{\varepsilon + 2\varepsilon_m}. \tag{2.13}$$

This solution demonstrates that the external field induces a dipole moment within the sphere proportional to the magnitude of the applied field, $|\mathbf{E}_0|$. The polarizability, α, undergoes resonant enhancement when the condition $\mathrm{Re}[\varepsilon(\omega)] = -2\varepsilon_m$ and $\mathrm{Im}[\varepsilon(\omega)] = 0$ is satisfied. At resonance, the internal and dipolar fields are significantly amplified, leading to a concurrent increase in the efficiency of light scattering ($\propto a^6$) and absorption ($\propto a^3$) by the particle.

The curved surface of the sphere exerts an effective restoring force on the oscillating conduction electrons, enabling a resonance that amplifies the field both inside the particle and in the near-field region. This phenomenon is known as the localized surface plasmon resonance (LSPR). Unlike propagating surface plasmon polaritons, LSPRs can be excited directly by incident light without requiring phase-matching techniques, due to the curvature of the particle's surface.

Additionally, the resonance wavelength of the LSPR red-shifts with increasing ε_m, the dielectric constant of the surrounding medium. This dependency makes metal nanoparticles particularly suited for optical sensing applications, where they can detect changes in the refractive index of their environment.

The calculations outlined above provide a reasonably accurate approximation for spherical particles with dimensions smaller than 100 nm when exposed to visible or near-infrared light. However, for larger particles, the quasi-static approximation becomes insufficient due to significant phase variations of the incident field across the particle's volume.

In a landmark study published in 1908, Gustav Mie developed analytical solutions to describe the interaction of spherical particles with light, particularly when the particle dimensions are comparable to the wavelength of the incident radiation[3]. This work explained phenomena such as the red coloration of colloidal gold and established a framework for understanding light scattering and absorption. Mie's approach involves expanding the scattered and internal electric and magnetic fields into a series of normal modes using vector harmonics. These harmonics characterize the particle's electromagnetic response and provide a comprehensive description of light-matter interactions across different regimes, from Rayleigh scattering in the case of very small particles to geometrical optics for much larger particles.

Particle size in Mie theory is defined relative to the wavelength of the incident light or, for metallic particles, the mean free path of conduction electrons. For particles much smaller than the wavelength, the quasi-static approximation can be recovered by performing a power series expansion of the scattering and absorption coefficients and retaining only the leading term. Using Mie's formalism, the scattering and extinction cross-section can be determined as follows:

$$\begin{aligned}\sigma_{sca} &= \frac{2\pi}{k^2}\sum_{n=1}^{\infty}(2n+1)\left(|a_n|^2+|b_n|^2\right),\\ \sigma_{ext} &= \frac{2\pi}{k^2}\sum_{n=1}^{\infty}(2n+1)\,\mathrm{Re}[a_n+b_n].\end{aligned} \tag{2.14}$$

where n is a positive integer value and $k^2 = \omega^2\varepsilon\mu$.

The coefficients a_n and b_n are read as:

$$\begin{aligned}a_n &= \frac{\tilde{m}\psi_n(\tilde{m}x)\psi_n'(x)-\psi_n(x)\psi_n'(\tilde{m}x)}{\tilde{m}\psi_n(\tilde{m}x)\xi_n'(x)-\xi_n(x)\psi_n'(\tilde{m}x)}\\ b_n &= \frac{\psi_n(\tilde{m}x)\psi_n'(x)-\tilde{m}\psi_n(x)\psi_n'(\tilde{m}x)}{\psi_n(\tilde{m}x)\xi_n'(x)-\tilde{m}\xi_n(x)\psi_n'(\tilde{m}x)}\end{aligned} \tag{2.15}$$

where $\tilde{m} = \frac{m_1}{m_2}$ is the ratio of the refractive indices of the sphere n_1 and the medium n_2, and $x = kR$ is the size parameter. $\xi_n(k\pi) = k\pi \cdot h_n^{(1)}(k\pi)$ and $\psi_n(k\pi) = k\pi \cdot j_n^{(1)}(k\pi)$ are the Riccati-Bessel functions, where $j_n^{(1)}$ and $h_n^{(1)}$ are the spherical Bessel functions and the spherical Hankel functions. For a more detailed discussion of the calculations, readers are encouraged to consult the comprehensive text by Bohren and Huffman[4].

2.2 Plasmonic catalysis

As mentioned in the above chapters, when LSPR is excited by light with certain wavelength, the plasmonic metal nanostructures with large scattering cross-section will confine photons to regions much smaller than their diffraction limit. This interaction induces a collective oscillation of surface free electrons at frequencies that match the incoming photons, which is a pronounced optical extinction. Interestingly, the extinction peaks are influenced by the nanostructures' composition, shape, and surrounding dielectric medium[5]. Due to these characteristics, LSPR has garnered significant attention in diverse applications, including plasmon-based sensors and spectroscopy[6], light source technologies[7], medical innovations[8], and energy storage systems[9–11]. Besides, LSPR excitation has been increasingly employed to accelerate chemical reaction rates and control chemical processes, leading to the development of the field of plasmonic catalysis[5,12–14].

2.2.1 Fundamentals and advances in plasmonic catalysis

Plasmonic catalysis utilizes visible or near-infrared light as a sustainable energy source for driving molecular transformations, combining both optical and catalytic functionalities of plasmonic nanostructures. When a LSPR is excited, it dramatically amplifies the electromagnetic field near the surfaces of plasmonic nanostructures. Through nonradiative Landau damping, energetic charge carriers form

within hundreds of femtoseconds. These carriers rapidly (100 fs to 1 ps) redistribute energy through electron-electron scattering, creating 'hot' electrons and holes - 'hot' refers to charge carriers with energies larger than those of thermal excitations at ambient temperatures. Subsequent relaxation transfers energy to phonons, generating localized heat[15,16]. This process is illustrated in the schematic diagram of figure 2.3, providing readers with a clearer and more visualized understanding of the mechanism. In general, there are three key effects of LSPR excitation that underpin plasmonic catalysis: near-field enhancement, energetic hot carriers, and localized heating. In the following paragraphs, we will discuss in greater detail how these unique phenomena influence catalytic processes.

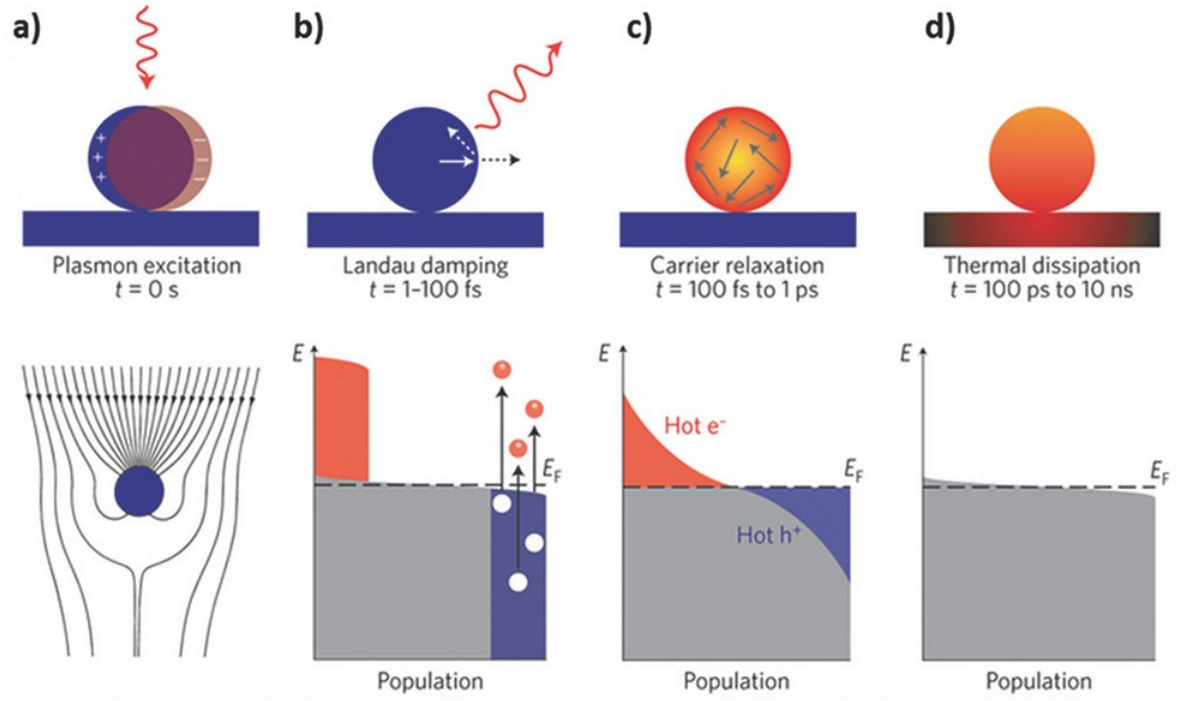

Figure 2.3: Photoexcitation and subsequent relaxation processes when a metal nanoparticle is illuminated. (a) The excitation of a localized surface plasmon resonance (LSPR) redirects the flow of light (Poynting vector) toward and into the nanoparticle. (b–d) Schematic representations of electronic state populations (grey) following plasmon excitation: hot electrons (red regions above the Fermi energy, E_F) and hot holes (blue regions below E_F) emerge. **(b)** Through Landau damping, the athermal electron–hole distribution relaxes via photon re-emission or carrier multiplication due to electron–electron interactions (1–100 fs). **(c)** Hot carriers then redistribute energy through electron–electron scattering processes (100 fs–1 ps). **(d)** Finally, energy is transferred to the surroundings of the metallic structure via thermal conduction (100 ps–10 ns). Reprint from Ref [15].

Hot Carriers.

The hot charge carriers generated by dephasing of plasmons can be transferred to surrounding environments, including molecular adsorbates. This transfer can ionize the molecules, thereby facilitating redox reactions. Notably, unlike conventional catalytic methods, plasmon-induced hot carrier transfer provides access to novel reaction pathways and enhances product selectivity[15,16].

The charge transfer processes can occur via two mechanisms: indirect or direct transfer, a schematic illustration of these two mechanisms in metal/adsorbate and metal/semiconductor systems is demonstrated in Figure 2.4.

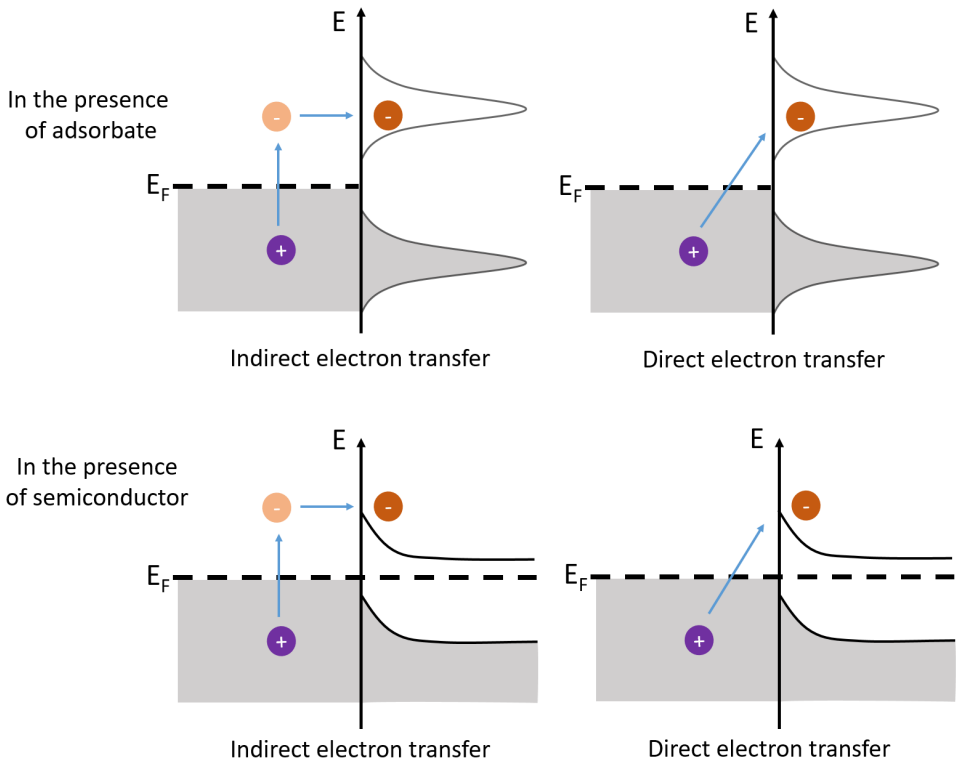

Figure 2.4: Plasmon-induced hot carrier generation and transfer processes in metal/adsorbate interfaces, and metal/semiconductor systems. For each scenario, the left component (relative to the energy y-axis) represents the Fermi level (E_F) of the plasmonic metal, while the right component illustrates the highest occupied molecular orbitals (HOMOs) and lowest unoccupied molecular orbitals (LUMOs) for adsorbates or the conduction band (CB) and valence band (VB) positions for semiconductors. The gray regions indicate the electronic state populations in each system. Adapted with permission from Ref [17].

In the indirect mechanism, electronic excitation occurs within the plasmonic metal, followed by a secondary injection step[18]. In this charge transfer mechanism, the energy of the excited carriers is critical, as they must overcome potential barriers. For instance, on the metal-semiconductor interfaces, the plasmonic hot electrons must overcome the Schottky barrier to escape from the metal nanoparticle. This interfacial energy barrier forms when the metal and semiconductor materials are brought into contact, leading to a flow of electrons, until the equalization of the Fermi levels of the two materials is achieved. As a result, the conduction and valence bands of the semiconductor bend upward for an n-type semiconductor and downward for a p-type semiconductor[18]. The Schottky barrier on one hand prevents low-energy carriers from leaving the metal, on the other hand also limits the

charge back-transfer, which makes the hybrid structures of plasmonic metal-semiconductor effective in prolonging the lifetime of plasmon generated hot carriers[19,20]. Similarly, for molecules adsorbed on plasmonic materials, the alignment between the electronic states of the metal and the hybridized states of the adsorbate is crucial for efficient charge injection. Specifically, when the lowest unoccupied molecular orbital (LUMO) of the molecule is at a higher energy than the metal's Fermi level, additional energy is required to facilitate carrier injection, therefore the gap between (E_F) of the metal and LUMO of adsorbate largely affects the efficiency of charge transfer[21]. Other factors such as the molecular affinity[22] could further influence the efficiency of this process.

The case of direct plasmon-induced charge transfer involves the decay of a surface plasmon through the direct excitation of an electron in the semiconductor or adsorbed molecule and a corresponding hole in the metal, or vice versa[18]. As the name suggests, the direct charge transfer mechanism occurs in a single step, bypassing the intermediate phase of charge retention within the particle. Since carriers are not retained within the metal, the rapid scattering processes that typically dissipate energy are avoided. Consequently, this mechanism achieves near-perfect injection efficiency by eliminating the most detrimental energy dissipation step[23]. To be noted, a recently published study reported an overall electron transfer efficiency of $44 \pm 3\%$ from gold nanorods to titanium oxide shells when excited on resonance[24]. It was demonstrated that approximately half of this efficiency arises from direct interfacial charge transfer mediated specifically by plasmon excitation. These findings underscore the promise of the direct plasmon-induced charge transfer pathway in improving hot carrier extraction efficiency. By circumventing the intrinsic decay mechanisms of metals, which predominantly result in nonspecific heating, this approach holds significant potential for advancing photocatalytic applications.

Electric Field Enhancement

Another key outcome of plasmon excitation is the localization of electromagnetic energy near the nanoparticle surface, leading to significantly enhanced electric fields. Notably, this strong electric field decays rapidly with distance and is therefore referred to as near-field enhancement[25]. In isolated nanoparticles, the field intensity can exceed the incident field by a factor of 10^2, and in regions with sharp structural features, even higher enhancements can be achieved[26]. For instance, metallic nanostars are particularly effective for photocatalytic applications due to their remarkably enhanced electric field, which is also called plasmonic "hotspots". These strong hotspots significantly increase the internal generation rates of hot carriers and lead to impressive photocatalytic performances[27]. Notably, the plasmon-induced localized electric field enhancement leads to the development of a steady-state charge and an associated electrostatic potential in noble metal nanoparticles[28]. This photopotential (or photovoltage) modulates both the energetics and kinetics of surface chemical reactions, particularly those involving charge transfer, which is critical for photocatalysis[29].

Another extensively studied application of plasmon-enhanced fields is surface-enhanced Raman spectroscopy (SERS), where the amplified field significantly intensifies Raman scattering signals from molecular adsorbates on metallic surfaces[30]. In such systems, the electromagnetic enhancement factor for SERS, depending on the structure of the plasmonic material, is theoretically estimated to reach

magnitudes of 10^{10} to 10^{11}[31,32]. Similarly, plasmonic near-fields can enhance fluorescence signals from fluorophores[33] and intensify molecular chiral signals[34]. Overall, near-field enhancement is a key characteristic of LSPR excitation, and further research and broader applications could unlock additional potential of plasmonic phenomena.

Thermal Effects

Upon light irradiation, plasmonic metals undergo non-radiative decay of excited electrons, generating hot carriers that can selectively interact with adsorbed molecules to activate specific chemical bonds or dissipate energy as localized heating. Studies have demonstrated that rationally designed plasmonic photothermal catalysts can harness both hot carriers and photothermal effects to enhance catalytic activity and modulate reaction selectivity[35]. For instance, SiO_2/Ag@TiO_2 core–shell nanocomposites have been employed as solar thermal collectors for hydrogen production from glycerol solutions. Under full-spectrum illumination, these catalysts achieved a reaction rate of 1536 μmol g^{-1} h^{-1}, significantly higher than the 786 μmol g^{-1} h^{-1} rate observed under UV illumination alone. This enhancement was attributed to the photothermal effect, which increased catalyst temperature and improved hole scavenging by glycerol[36]. These findings highlight the potential of full-spectrum solar energy utilization in photocatalytic processes. To get a comprehensive understanding of plasmon involved catalytic processes, a deeper study of the interplay between thermal and non-thermal effects in plasmon-assisted catalysis is essential, necessitating precise temperature measurements under operando conditions. Emerging techniques such as anti-Stokes (AS) thermometry provide promising approaches for directly measuring the temperature of plasmonic nanoparticles. For example, Cortés et al. validated AS thermometry for monitoring light-induced heating in plasmonic ensembles and confirmed its accuracy using wavefront microscopy[37,38]. These advancements underscore the importance of temperature control in optimizing plasmonic catalytic systems. All investigations on plasmonic thermal effects highlight their great potential in enhancing catalytic activity and selectivity, with a deeper understanding of the underlying mechanisms enabled by novel characterization techniques.

These above effects, acting individually or synergistically, channel low-intensity photon energy into surface adsorbates, accelerating and modulating chemical reactions. The distinctive LSPR effect allows for substantial enhancement of catalytic reaction rates under relatively mild light conditions, thus the field of plasmonic catalysis has attracting more and more attentions. Notably, by fine-tuning structural features, plasmonic metal nanostructures can effectively interact with photons across nearly the entire solar spectrum, especially in the visible region, which accounts for approximately 50% of solar energy, making them an optimal platform for light absorption[14].

Except for impressive ability of plasmonic catalytic materials in harvesting solar spectrum, their potential in improving the reaction selectivity and activity has also been proved many studies[12,39]. Catalytic processes typically involve several steps, including the adsorption and activation of reactants, the transformation of intermediates, and the desorption of final products. To realize high selectivity and

activity, these steps should be carefully controlled, which has always been challenges in conventional catalytic processes. For example, in traditional thermally driven catalysis, which adjusts the energy barriers and adsorption energies of all steps simultaneously. However, plasmonic catalysis offers a more energy-efficient alternative with precise control over individual steps[14]. By manipulating factors such as the intensity and wavelength of incident light, the enhancement of local electric fields, the distribution of hot carriers, and localized heating effects can be adjusted by the chemical reaction landscape[40]. This level of control supports the selective adsorption, activation, or desorption of molecules, facilitating the selective and efficient conversion and storage of solar energy in chemical bonds.

More interestingly, many materials with plasmonic properties themselves are perfect catalysts for lots of chemical reactions, such as Au[41], Ag[42], Pt[43,44], Al[45,46], etc. Additionally, combining plasmonic metals with other materials like transition metals or semiconductors to form hybrid plasmonic nanomaterials, further expands the scope of plasmonic catalytic reactions. The hybrid materials on one hand enhance the light harvesting efficiency and prolong the lifetime of photo-generated energetic charge carriers, on the other hand prompt the interaction with target molecules and enhance the stability of the material, here Figure 2.5 highlights several advantages of hybrid plasmonic catalytic systems which are desirable for catalytic processes[1].

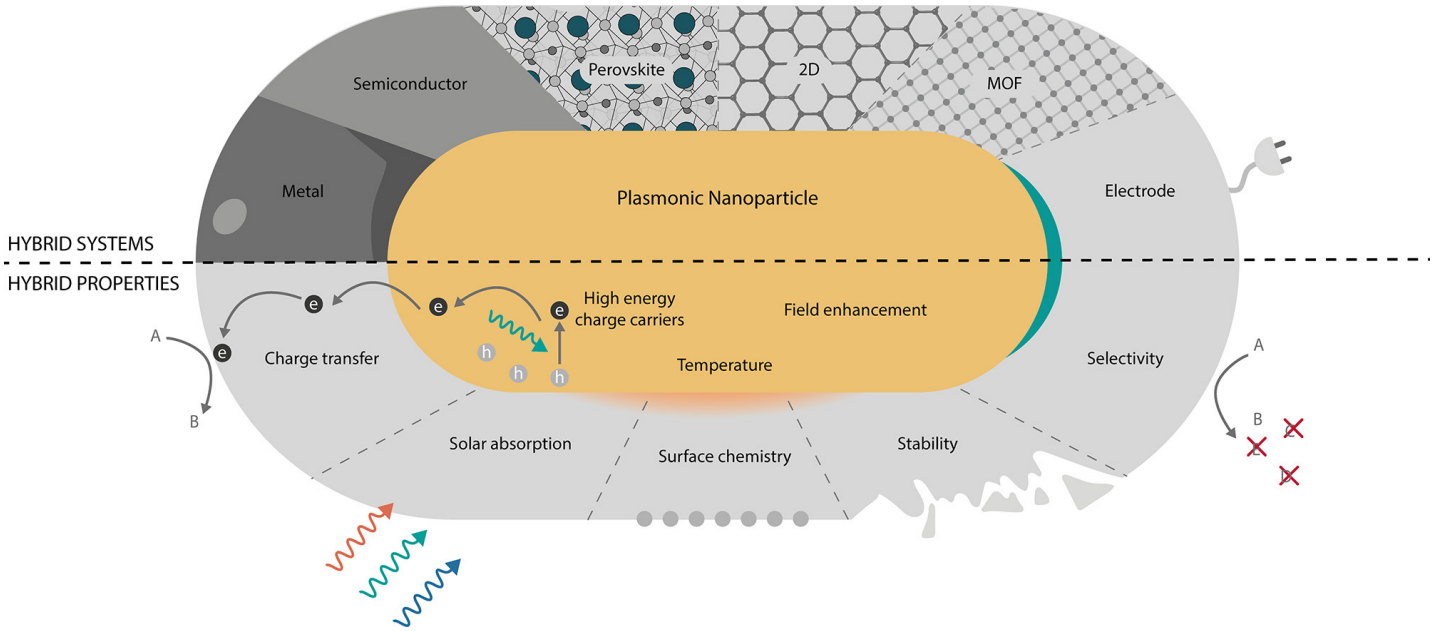

Figure 2.5: Overview of hybrid plasmonic systems that are widely studied, along with the desirable properties of an ideal photocatalyst. In these systems, the plasmonic component is responsible for harvesting light and transferring energy through mechanisms such as charge carriers, localized heating, and enhanced electromagnetic fields. Non-plasmonic materials, on the other hand, contribute by adding or improving catalytic properties. Through synergistic interactions, hybrid systems can achieve enhanced stability, selectivity, and catalytic activity. These improvements are facilitated by mechanisms such as efficient charge transfer, modified surface chemistry, and increased light absorption. Reprint with permission from Ref [1].

Despite these advantages, numerous challenges remain in the field of plasmonic catalysis. One major issue is the limited availability of high-value products with sufficient selectivity and activity for industrial applications. To develop efficient plasmonic catalysts, both material design and mechanistic understanding are crucial. For example, investigating activation pathways is needed for distinguishing between nonthermal and thermal mechanisms, which can provide valuable theoretical guidance for designing more effective catalysts. Additionally, robust nanofabrication techniques must be developed to enable large-scale nanophotonics-based plasmonic chemical processes. Highly stable nanomaterials are essential to compete with existing thermal catalysts while addressing key issues such as sintering and poisoning effects in plasmonic catalysts. Moreover, integrating plasmonic catalysts into large-scale industrial reactors with high device efficiency is also critical for their practical application. Another pressing challenge is the sustainability of plasmonic catalysis. Most current plasmonic catalysts rely on noble metals, which are rare, expensive, and impractical for widespread industrial use. Research is needed to explore earth-abundant plasmonic materials for sustainable chemical processes[13]. Addressing these challenges requires continued efforts and further studies to advance the field of plasmonic catalysis toward real-world applications.

2.2.2 Shape-controlled synthesis of plasmonic nanoparticles

The preceding chapters highlighted the significant potential of plasmonic materials for tuning activity and selectivity in chemical reactions. Achieving this goal requires the preparation of nanoparticles with well-defined morphology and size, as the plasmonic response is highly dependent on these characteristics of plasmonic nanostructures. In this thesis, plasmonic gold nanoparticles with various morphologies were synthesized using bottom-up approaches based on wet chemical methods. A brief overview of this fabrication process is provided to offer readers a clearer understanding of how precise control over nanoparticle morphology and size is realized.

The synthesis of metallic nanocrystals often relies on relatively simple redox reactions; however, the mechanisms governing crystal nucleation and growth are inherently complex[47–50]. A widely adopted strategy for producing nanoparticles with well-defined shapes involves using seeds with controlled internal structures in conjunction with appropriate capping agents[51,52]. This approach ensures that crystals follow specific kinetic pathways, enabling the formation of nanoparticles with desired morphologies. Seed-mediated synthesis can be divided into three main stages: nucleation, seed formation, and nanocrystal growth[53].

The nucleation phase begins with an increase in metal atom concentration by reducing metal salt solutions. When the concentration exceeds the supersaturation threshold, metal atoms aggregate into small clusters, forming crystal nuclei that serve as precursors to seeds.

In the seed formation stage, the concentration of metal atoms drops below the critical supersaturation point. Since metal atoms are supplied through precursor decomposition, they tend to attach to the nuclei and lead to its growth. At the critical size, structural fluctuations stabilize, and seeds

with well-defined structures are formed. The structure of these seeds is determined by a balance of thermodynamic and kinetic factors, which can be controlled through reaction parameters[50,52]. For instance, slow reduction or decomposition reactions promote the random hexagonal close packing of atoms into stable seeds[50].

The final stage, nanocrystal growth, involves the deposition of additional metal atoms onto the seed surface. This growth is driven by a balance between the crystal volume energy, favoring growth, and surface energy. The equilibrium between these forces dictates the final morphology of the nanocrystals. To be mentioned, the capping agents play a critical role by selectively binding to specific crystal facets, modifying their relative free energies, and guiding anisotropic growth[54]. Besides, external factors such as pH[55], temperature[56], ionic strength[57,58], and magnetic fields[59] can further influence the aggregation of atoms and the formation of nanoparticles. Importantly, for many noble metals, a clear correlation has been established between the structure of the initial seeds and the final nanocrystal morphology[60,61].

The ability to precisely synthesize nanoparticles with controlled shapes is of great interest, as the morphology and size of nanostructures play a critical role in determining their optical and catalytic properties. These advancements hold significant value for applications in plasmonic catalysis and related fields.

2.3 Chemical reactions involved in the thesis

CO_2 reduction reaction

Carbon dioxide (CO_2), due to its ability to absorb infrared radiation through excited vibrational modes, plays a significant role in trapping heat within Earth's atmosphere[62], making it a potent greenhouse gas. Although it constitutes only about 0.04% of the atmosphere by volume (421 ppm as of December 2023)[63], CO_2 has substantially contributed to global warming and climate change. Alarmingly, its concentration has risen dramatically from pre-industrial (1960s) levels of approximately 280 ppm to over 400 ppm in recent years[63]. This concerning upward trend is illustrated in Figure 2.6. In addition to its atmospheric effects, CO_2 dissolves in water to form carbonate and bicarbonate ions, causing ocean acidification as atmospheric levels continue to increase[64]. Among the various sources of CO_2 emissions, the primary driver of this increase is the combustion of fossil fuels. Global CO_2 emissions from fossil fuel consumption have skyrocketed from 9.36 billion tons in 1960 to 37.79 billion tons in 2023 — an increase of more than fourfold[65]. However, modern society remains heavily reliant on nonrenewable energy sources such as fossil fuels. In 2023, energy generated from gas, oil, and coal surpassed 14,000 TWh, accounting for over 85% of the total global energy consumption. In contrast, energy derived from solar power was only 1,600 TWh. The dual challenges of excessive CO_2 emissions and an outdated, environmentally unsustainable energy structure urgently demand effective solutions to achieve sustainable development.

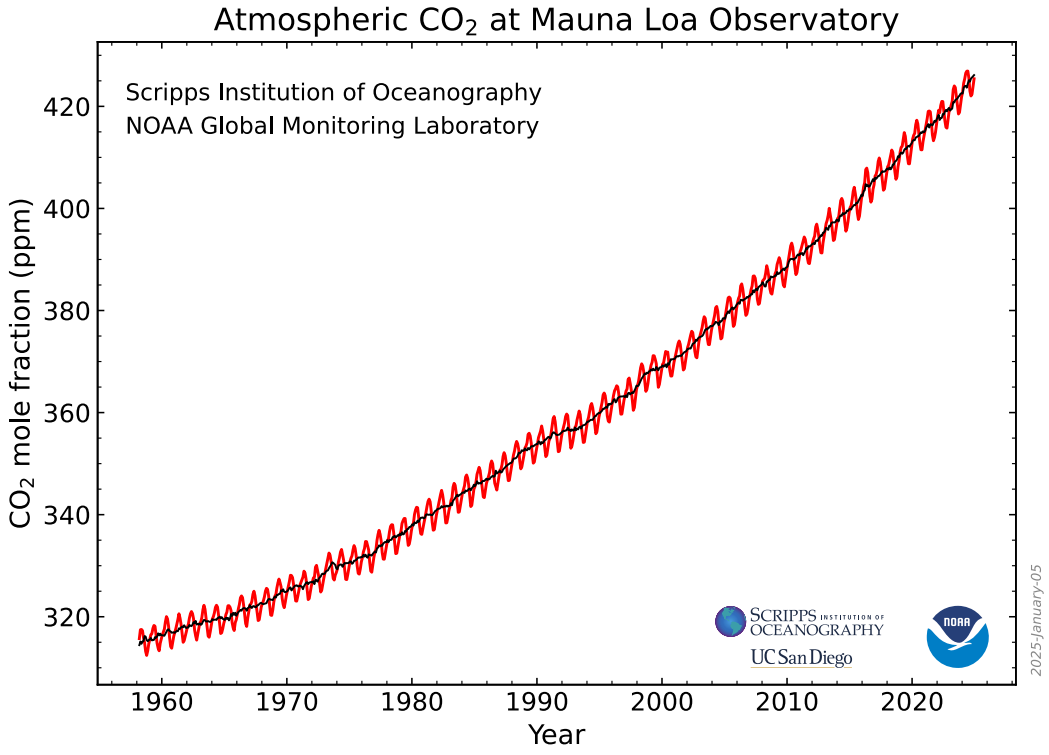

Figure 2.6: Trends in atmospheric carbon dioxide. Reprint from Ref [63].

A promising solution to address these issues simultaneously is the conversion of CO_2 into valuable fuels, chemicals, or other carbon-based products. This approach not only reduces atmospheric CO_2 levels but also transforms waste into valuable resources, potentially mitigating the problem of overdependence on unsustainable fossil fuels.

However, CO_2 reduction presents significant challenges due to the molecule's chemical stability and inertness[66,67]. The linear and centrosymmetric structure of CO_2, characterized by double bonds between the carbon and oxygen atoms, results in a high thermodynamic barrier for reduction reactions[68,69].

Moreover, these reduction reactions involve complex pathways and multiple steps, often producing a variety of products such as carbon monoxide (CO), formic acid (HCOOH), methane (CH_4), methanol (CH_3OH), ethanol (CH_3CH_2OH), and others. In many cases, water plays a crucial role in CO_2 reduction, either as a proton source or as a medium for dissolved gaseous CO_2. However, this introduces an unavoidable competing reaction: hydrogen evolution reaction (HER). Table 2.1 lists common possible reactions in electrocatalytic CO_2 reduction systems along with their corresponding equilibrium potentials of reactions[66,70–72]. These complex reaction pathways and the resulting mixture of products

highlight the critical need for a highly efficient and selective catalyst system. Achieving high selectivity for specific products is especially important for large-scale applications.

Reaction Formulation	E^0 (V vs RHE)	Product
$2H_2O \rightarrow O_2 + 4H^+ + 4e^-$	1.23	Oxygen
$2H^+ + 2e^- \rightarrow H_2$	0.00	Hydrogen
$CO_2 + 2e^- + 2H^+ \rightarrow HCOOH(aq)$	-0.12	Formic acid
$CO_2 + 2e^- + 2H^+ \rightarrow H_2O + CO(g)$	-0.10	Carbon monoxide
$CO_2 + 6e^- + 6H^+ \rightarrow H_2O + CH_3OH(g)$	0.03	Methanol
$CO_2 + 8e^- + 8H^+ \rightarrow 2H_2O + CH_4(g)$	0.17	Methane
$2CO_2 + 2e^- + 2H^+ \rightarrow (COOH)(s)$	-0.47	Oxalic acid
$2CO_2 + 8e^- + 8H^+ \rightarrow 2H_2O + CH_3COOH(aq)$	0.11	Acetic acid
$2CO_2 + 10e^- + 10H^+ \rightarrow 3H_2O + CH_3CHO(aq)$	0.06	Acetaldehyde
$2CO_2 + 12e^- + 12H^+ \rightarrow 3H_2O + C_2H_5OH(aq)$	0.09	Ethanol
$2CO_2 + 12e^- + 12H^+ \rightarrow 4H_2O + C_2H_4(g)$	0.08	Ethylene
$2CO_2 + 14e^- + 14H^+ \rightarrow 4H_2O + C_2H_6(g)$	0.14	Ethane
$3CO_2 + 16e^- + 16H^+ \rightarrow 5H_2O + C_2H_5CHO(aq)$	0.09	Propionaldehyde
$3CO_2 + 18e^- + 18H^+ \rightarrow 5H_2O + C_3H_7OH(aq)$	0.10	Propanol
$CO + 6e^- + 6H^+ \rightarrow H_2O + CH_4(g)$	0.26	Methane
$2CO + 8e^- + 8H^+ \rightarrow H_2O + C_2H_5OH(aq)$	0.19	Ethanol
$2CO + 8e^- + 8H^+ \rightarrow 2H_2O + C_2H_4(g)$	0.17	Ethylene

Table 2.1: Reactions involved in CO_2 reduction electrolysis and their corresponding equilibrium potentials (E^0)

Various methods for CO_2 conversion have been extensively explored[71]. Traditional thermal catalysis, while effective in achieving high conversion rates, requires extreme reaction conditions and substantial energy input[73]. A more economical alternative is electrochemical CO_2 reduction[74], which utilizes solar-driven power to convert electrical energy into chemical energy. However, this method faces significant challenges, including low reaction rates, high overpotentials, and poor selectivity, particularly for multicarbon products. These limitations arise from the strong adsorption energies of reaction intermediates and competition with the hydrogen evolution reaction, which occurs at similar potentials but exhibits faster kinetics[75].

Photocatalysis represents another promising approach, as CO_2 reduction can occur on the surface of irradiated photocatalysts[67]. While thermodynamically more favorable than electrochemical methods, the reaction is hindered by the high energy gap of CO_2 as 13.7 eV between the LUMO and HOMO orbitals and its highly negative redox potential of -1.9 V at pH 7[74]. The adsorption of CO_2 onto photocatalyst surfaces, such as TiO_2, has been shown to lower the LUMO level, facilitating electron transfer[76]. However, the efficiency of solar-to-fuel conversion remains low, limiting the feasibility of large-scale applications.

Although numerous solar-active catalysts have been reported for CO_2 photoreduction, most suffer from low energy conversion efficiency, uncontrollable product selectivity, instability, and an inability to completely suppress the competing HER in the presence of water[70]. Consequently, the design and development of highly active photocatalytic systems with improved conversion efficiency and selectivity for CO_2 reduction remain critical challenges[67].

Interestingly, combining different approaches, such as coupling photocatalysis with electrochemical methods, has shown synergistic effects, enhancing both performance and selectivity. For example, applying an external potential to a photocatalytic system improves charge separation and conversion efficiency, while introducing photons into electrochemical processes can alter reaction pathways[77]. Notably, integrating plasmonics into electrocatalysis has demonstrated higher efficiencies and selectivities in the challenging CO_2 reduction reactions[78]. As shown in Figure 2.7 (b-d), the introduction of plasmonic effects enables the production of novel products, such as CH_3OH and HCOOH, which are rarely achievable with non-plasmonic catalysts. Additionally, plasmonic catalysts demonstrate superior performance in terms of both formation rate and selectivity.

In a typical photoelectrocatalytic CO_2 reduction system, catalyst performance is evaluated using metrics such as activity, measured by partial current density, and selectivity, assessed through Faradaic efficiency, which quantifies the proportion of electrons contributing to a specific product.

Recent research highlights the potential of plasmon-assisted electrochemical CO_2 reduction. For instance, Kim et al. demonstrated that plasmonic excitation increases the reaction rate and current density during CO_2 reduction on Ag nanopyramid electrodes[79]. Similarly, Creel et al. reported significant improvements in Faradaic efficiency for CO production on illuminated Ag thin-film electrodes, along with suppressed hydrogen evolution and the emergence of methanol as a product[80]. Plasmonic hybrid systems, such as Ag combined with Cu_2O/CuO plasmonic metal-semiconductor system, has also shown enhanced CO_2 reduction performance under illumination[81]. These systems benefit from reduced charge recombination, lower overpotentials, and improved stability of semiconductor materials. Additionally, plasmonically active bimetallic systems demonstrate substantial enhancements under plasmon excitation. For example, Cu-based catalysts coated with silver have exhibited selective enhancement of specific CO_2 reduction products, such as ethylene, methane, and formate, while suppressing undesirable side reactions like hydrogen evolution[82]. As shown in Figure 2.7 (b-d), the introduction of plasmonic effects enables the production of novel products that are rarely achievable with non-plasmonic catalysts, such as CH_3OH and HCOOH. Additionally, plasmonic catalysts exhibit excellent performance in terms of both formation rate and selectivity. These findings underscore the potential of incorporating plasmonics into electrocatalytic systems as a promising strategy to enhance CO_2 reduction activity and selectivity while leveraging light to reduce energy consumption.

Despite these advancements, several challenges remain. The reliance on expensive noble metals for plasmonic systems limits industrial scalability, and the Faradaic efficiencies for hydrocarbons and multicarbon products remain relatively low. Moreover, the mechanisms underlying the plasmonic effects in CO_2 reduction systems are not yet fully understood[1,13]. Future research should focus on

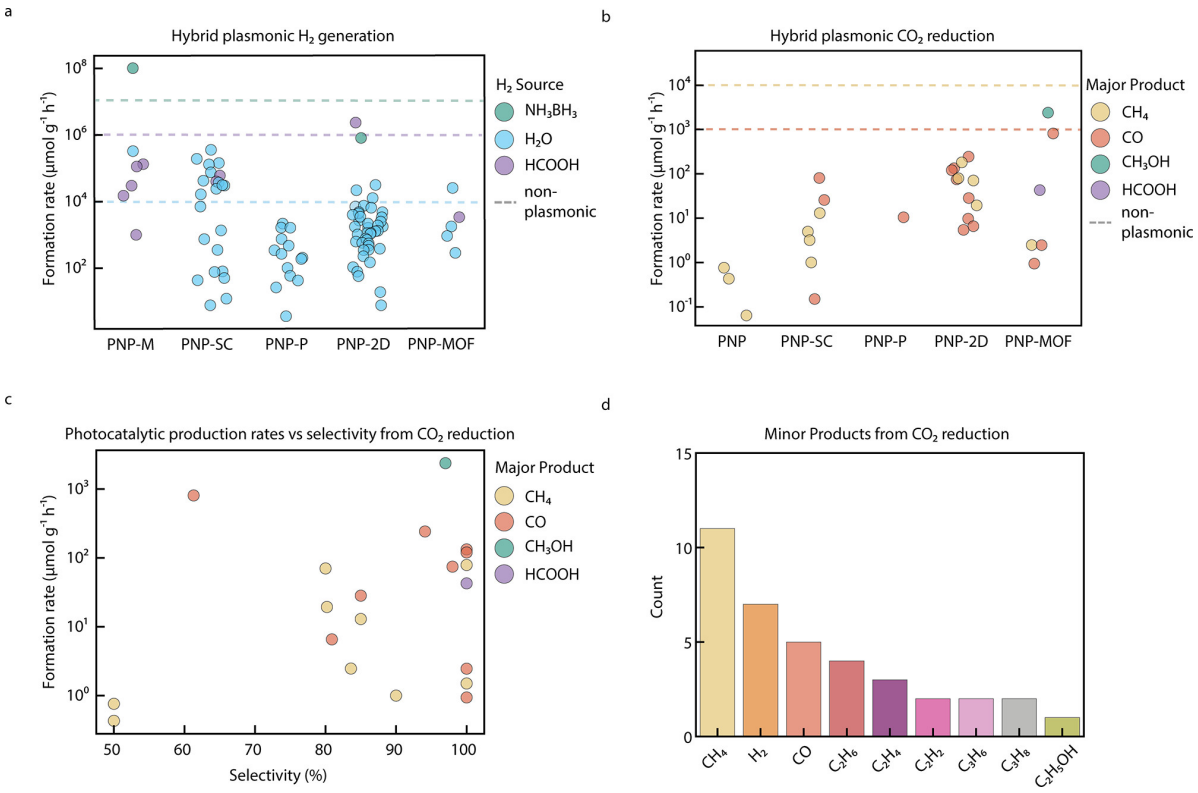

Figure 2.7: Hybrid plasmonic nanomaterials for H_2 generatio and CO_2 reduction. **(a)** H_2 generation and **(b)** CO_2 reduction for the different hybrid photocatalysts reviewed in our paper [1]. The dashed line illustrates the order of magnitude achieved with prominent examples of non-plasmonic catalysts. **(c)** Formation rate vs selectivity and **(d)** histogram of the number of publications vs the minor products reported. Reprint from Ref [1].

improving efficiencies, advancing mechanistic understanding, and exploring cost-effective alternatives to noble metals to facilitate the widespread adoption of plasmon-assisted CO_2 reduction technologies.

H_2 evolution reaction

With the increasing challenges of energy crises and environmental pollution, molecular hydrogen has garnered significant attention as a promising candidate for future energy systems. Its high specific energy, versatile applications, and environmentally friendly combustion byproduct make it an attractive alternative to traditional fossil fuels[83]. Currently, large-scale hydrogen production predominantly relies on the steam reforming of methane, a process that requires high temperatures and generates substantial carbon dioxide emissions. To position hydrogen as a viable replacement for fossil fuels, the development of alternative, sustainable production technologies is essential.

Electrochemically driven hydrogen evolution reaction (HER) systems represent a key strategy for sustainable hydrogen production. These systems enable hydrogen generation from water using sunlight or electricity as the primary energy inputs, bridging fundamental electrochemistry with practical applications[84]. The hydrogen evolution reaction (HER) can occur in strongly acidic or

alkaline solutions, although intermediate pH and buffered solutions are also sometimes employed for experimental studies[85,86].

In acidic solutions, the overall HER process is described by Eq. (1), while the equilibrium potential (E_{eq}) is given by Eq. (2):

$$H^+ + e^- = \frac{1}{2}H_2 \tag{1}$$

$$E_{eq} = E^0 + \frac{1}{2f} \ln \frac{(a^*_{H^+})^2}{a^*_{H_2}} \tag{2}$$

Here, E^0 denotes the standard hydrogen electrode potential, which is conventionally set to zero. The term a_{H^+} represents the proton activity in the bulk solution, and f_{H_2} corresponds to the hydrogen fugacity above the solution. The factor f = F/RT incorporates the relationship between the Faraday constant (F), the gas constant (R), and the temperature (T). The equilibrium potential, also referred to as the open-circuit potential, is typically measured using a Pt-black electrode. For further details, readers may consult references[86,87].

While the above equations describe the overall reaction, the hydrogen evolution reaction mechanism consists of multiple steps. The first step is the electrochemical adsorption of hydrogen onto the electrode surface (Volmer reaction), followed by either electrochemical desorption (Heyrovsky reaction) or chemical desorption (Tafel reaction). These steps are expressed as follows. To be mentioned, the rate constants associated with these reactions are potential-dependent and significantly influence the overall reaction kinetics.

$$H^+ + M + e^- \underset{k_{-1}}{\overset{k_1}{\rightleftharpoons}} MH_{ads} \quad \text{Volmer} \tag{3}$$

$$H^+ + MH + e^- \underset{k_{-2}}{\overset{k_2}{\rightleftharpoons}} H_2 + M \quad \text{Heyrovsky} \tag{4}$$

$$2MH \underset{k_{-3}}{\overset{k_3}{\rightleftharpoons}} H_2 + 2M \quad \text{Tafel} \tag{5}$$

However, despite its promise, conventional electrocatalytic HER systems still face challenges, such as low efficiency and high energy demands, necessitating continued research to enhance catalytic performance. To address these issues, plasmonic electrocatalysis has emerged as a novel approach for improving catalytic efficiency through the integration of renewable solar energy . By utilizing light absorbed by electrocatalysts or associated materials, plasmonic effects can modulate electronic structures and influence local environments, thereby accelerating surface reactions[88]. As shown

in Figure 2.7 (a), many plasmonic hybrid photocatalysts (dots) demonstrate superior H_2 generation performance compared to prominent non-plasmonic catalysts (dashed line).

In plasmonic electrocatalytic HER systems, key metrics for evaluating catalysts include the current density at various overpotentials and the onset potential, which indicate activity, as well as the Tafel slope, which provides insights into reaction kinetics and efficiency.

Significant progress has been made in this field. For example, a study by Wei et al. investigated the effect of different configurations of metal-metal hybrid nanostructures on plasmon-enhanced HER performance[89]. Gold nanostars modified with AgPt alloys in various arrangements - covered, tipped, and edged—exhibited notable differences in activity. Among these, the AgPt-tipped Au nanostars demonstrated superior performance, achieving a lower overpotential (58 mV vs. RHE) and a reduced Tafel slope (35 mV/dec), indicating enhanced charge transfer and improved reaction kinetics. This configuration optimized the synergy between Au nanostars, which acted as light absorbers generating heat and excited electrons, and AgPt alloys, which served as electron acceptors and reactive sites.

Another study by Du et al. highlighted the synergistic effects between plasmonic nanoparticles and conventional semiconductor electrocatalysts in solar-enhanced water splitting[90]. A composite of gold nanoparticles and NiCo layered double hydroxides (LDH) demonstrated significantly reduced overpotentials for both HER and the oxygen evolution reaction (OER) under illumination compared to dark conditions. This improvement was attributed to plasmonic excitation, which enhanced charge transport efficiency. These findings underscore the potential of integrating plasmonic materials into pure electrocatalytic HER systems to reduce energy consumption and improve catalytic performance.

Involving plasmon offers a promising pathway for advancing pure electrocatalytic HER, particularly in overcoming challenges that conventional methods have struggled to address. However, this field is still in its early stages and requires further research to optimize catalytic performance and gain a deeper understanding of the underlying mechanisms. Such efforts are crucial for the development of efficient and sustainable hydrogen energy production and storage technologies.

H_2O_2 production

Hydrogen peroxide (H_2O_2) is an environmentally friendly oxidant, producing only water and molecular oxygen as byproducts, and offering high atom efficiency[91]. With its high active oxygen content by weight, H_2O_2 serves as a source of hydroxyl radicals (·OH) and is widely applied in organic synthesis, pulp bleaching, wastewater treatment, and disinfection[92]. Increasingly, H_2O_2 is thus being recognized as a potential solution to environmental pollution and energy shortages. Moreover, its in situ production has been proposed as a portable energy carrier in fuel cells, offering a power density comparable to pressurized hydrogen while providing the advantages of easier storage and transportation[93].

The current industrial production of H_2O_2 relies primarily on the anthraquinone process. Although the overall reaction ($H_2 + O_2 \rightarrow H_2O_2$) appears simple, the process involves multiple hydrogenation and oxidation steps, consuming large amounts of energy and organic solvents. Furthermore, the handling

of H_2-O_2 mixtures and concentrated H_2O_2 poses significant explosion risks[92]. These drawbacks highlight the urgent need for safer, more efficient, and environmentally sustainable alternatives.

Photocatalytic production of H_2O_2 from water and oxygen has emerged as a promising alternative, eliminating the need for H_2 as a reactant and thereby reducing explosion hazards. This approach relies on the two-electron reduction of O_2 or the oxidation of water to form H_2O_2[94,95]. The reactions involved in H_2O_2 production are summarized in Table 2.2.

Potential (V vs NHE)	Reaction
−0.33	$O_2 + e^- \rightarrow O_2^{\cdot -}$
−0.13	$O_2 + H^+ + e^- \rightarrow \cdot OH$
0.68	$O_2 + 2H^+ + 2e^- \rightarrow H_2O_2$
0.87	$H_2O_2 + e^- \rightarrow \cdot OH + OH^-$
1.00	$H_2O_2 + h^+ \rightarrow O_2^{\cdot -} + 2H^+$
1.23	$2H_2O + 4h^+ \rightarrow O_2 + 4H^+$
1.76	$2H_2O + 2h^+ \rightarrow H_2O_2 + 2H^+$

Table 2.2: Redox reactions involved in H_2O_2 production and their corresponding equilibrium potentials

The first mechanism, the direct two-electron oxygen reduction reaction (ORR) pathway, was initially demonstrated using g-C_3N_4. In this process, photoexcited electrons reduce O_2 to H_2O_2, while photoinduced holes oxidize alcohols to aldehydes and protons[96]. For efficient operation, the photocatalyst's conduction band potential must be at least +0.68 V vs. NHE, the equilibrium potential for this reaction, as shown in Table 2.2. However, when the conduction band potential is more negative than -0.33 V vs. NHE, a competing two-step single-electron reduction pathway can occur, leading to undesired side reactions and reduced selectivity.

Water oxidation (WOR) represents another pathway for H_2O_2 production, utilizing water as both the electron donor and H_2O_2 source. However, its slow kinetics pose significant challenges[95]. To mitigate this issue, alcohols or other sacrificial agents are often introduced to quench photogenerated holes and prevent electron-hole recombination.

Beyond direct ORR or WOR, an alternative "two-channel" approach in heterostructure photocatalysts combines both pathways to enhance H_2O_2 production. In this system, photoelectrons reduce O_2 on one component while holes on another component oxidize water, creating a synergistic effect that boosts H_2O_2 yields. For instance, ZIF-8/C_3N_4 heterostructures have demonstrated significantly increased H_2O_2 production rates via this mechanism[97].

Despite its potential, several challenges remain in photocatalytic H_2O_2 production. For example, the slow kinetics of water oxidation and the rapid recombination of photogenerated charge carriers significantly limit overall efficiency[94]. Furthermore, H_2O_2 decomposition is exacerbated by UV irradiation, reactions with radicals, and interactions with photogenerated electrons or holes[98]. Besides, the decomposition rate of H_2O_2 is influenced by various factors, including its concentration, temperature, pH, and the presence of stabilizers or impurities. Therefore, achieving high H_2O_2 yields requires

optimizing reaction conditions to favor H_2O_2 formation over decomposition[99,100]. Additionally, the use of scavengers such as ethanol or isopropanol in many photocatalytic systems raises concerns regarding the generation of toxic byproducts and increased costs[94].

While two-phase systems have been proposed to enhance H_2O_2 production efficiency, these approaches remain in their early stages. Future research should focus on designing advanced photocatalytic systems to improve efficiency, scalability, and sustainability. The development of photocatalysts with high activity and stability, particularly those based on earth-abundant materials, is urgently needed to address these challenges and realize the full potential of photocatalytic H_2O_2 production.

Plastic Photoreforming

Plastics are among the most versatile, durable, lightweight, and cost-effective materials, making them indispensable across a wide range of applications. They serve as essential components in adhesives, paints, and polymer composites and are extensively utilized in packaging and construction due to their ease of processing into diverse products. Over the past two decades, global plastic production has more than doubled, reaching 460 million tons in 2019[101], as illustrated in Figure 2.8. However, the widespread use of plastics has also resulted in significant environmental challenges. Plastics are the most widely discarded materials, with more than 80% being improperly disposed of, leading to pollution of terrestrial, aquatic, and atmospheric ecosystems[101], as shown in Figure 2.9. The COVID-19 pandemic further exacerbated this issue, contributing an estimated 8 million additional tons of plastic waste[102]. This pervasive plastic pollution not only threatens ecosystems and human health but also represents a considerable loss of valuable chemical resources.

Common plastics include polyethylene (PE), polyethylene terephthalate (PET), polyester (PES), polypropylene (PP), polystyrene (PS), polyurethane (PUR), and polyvinyl chloride (PVC). Despite their widespread use, most plastics present significant challenges for economical recycling. Mechanical recycling processes often degrade material quality, limiting the reuse of plastics and leading to downcycling into lower-quality products[103]. For example, PET, which is widely used in packaging and textiles, experiences a decline in material properties during mechanical recycling, restricting its reuse to only a few cycles. Consequently, only 7% of recycled PET bottles can be reprocessed into new bottles[104,105]. Chemical recycling methods, including hydrolysis, methanolysis, glycolysis, and aminolysis, offer alternative approaches but require high temperatures and may cause environmental harm[106]. Non-recycled PET is typically disposed of via landfilling or incineration, further exacerbating ecological issues. Plastic waste in the environment undergoes disintegration and degradation through physical, chemical, and biological processes, such as hydrolysis, photodegradation, biodegradation, and mechanical abrasion. These processes fragment macroscopic plastics into particles smaller than 5 mm, commonly known as microplastics[103]. Due to their persistence, rapid dispersal, and ease of ingestion by organisms, plastic pollution poses increasing environmental threats with significant ecological consequences. Addressing this growing problem requires urgent advancements in waste management strategies, recycling technologies, and sustainable alternatives to conventional plastics.

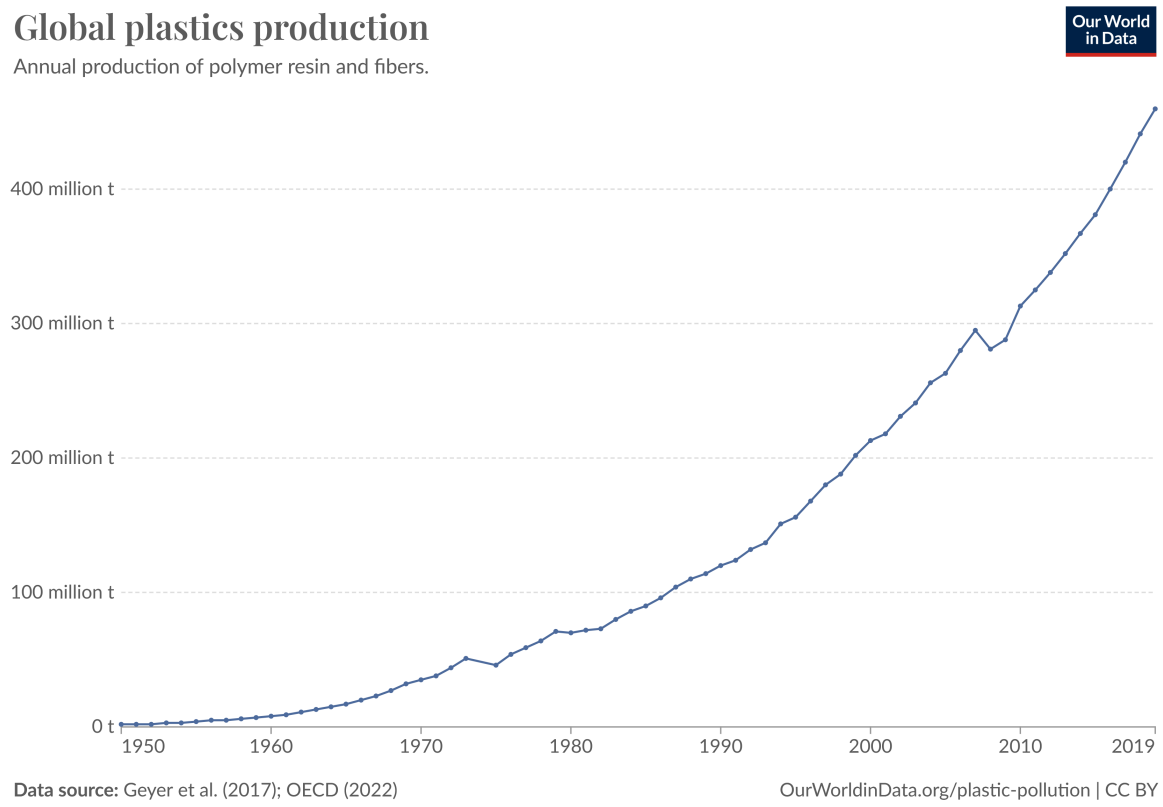

Figure 2.8: Global plastic production. Reprint from [101].

Advances in photocatalysis offer sustainable methods for addressing plastic waste under mild conditions using light energy. In 1981, Kawai and Sakata demonstrated the photoconversion of polyethylene (PE), polyvinyl chloride (PVC), and polyvinyl alcohol into CO_2 and H_2 using a Pt-TiO_2 catalyst under ultraviolet light[107]. More recently, photocatalytic systems such as Nb_2CO_5 have been shown to degrade PE, polypropylene (PP), and PVC into CO_2, which can subsequently be converted into acetic acid[108]. These systems effectively deconstruct addition polymers under mild conditions. However, a major limitation of these processes is that the primary carbon product, CO_2, is a greenhouse gas with limited economic value, reducing their overall practicality. To overcome this limitation, "photoreforming" has emerged as an innovative approach that simultaneously mitigates plastic waste and generates valuable chemical products[104,109,110]. This process utilizes sunlight and a photocatalyst to generate H_2 from an organic substrate and water. Upon light excitation, the photocatalyst generates electrons that reduce water to H_2, while photogenerated holes oxidize the plastic substrate into smaller organic molecules. Unlike conventional methods such as steam reforming of fossil fuels or thermal conversion of plastics into oil, photoreforming operates under ambient conditions, relies solely on solar energy, and produces high-purity H_2 suitable for fuel cells. Additionally, the process is thermodynamically favorable; for example, photoreforming ethylene glycol from plastic waste at room temperature requires minimal energy input[104].

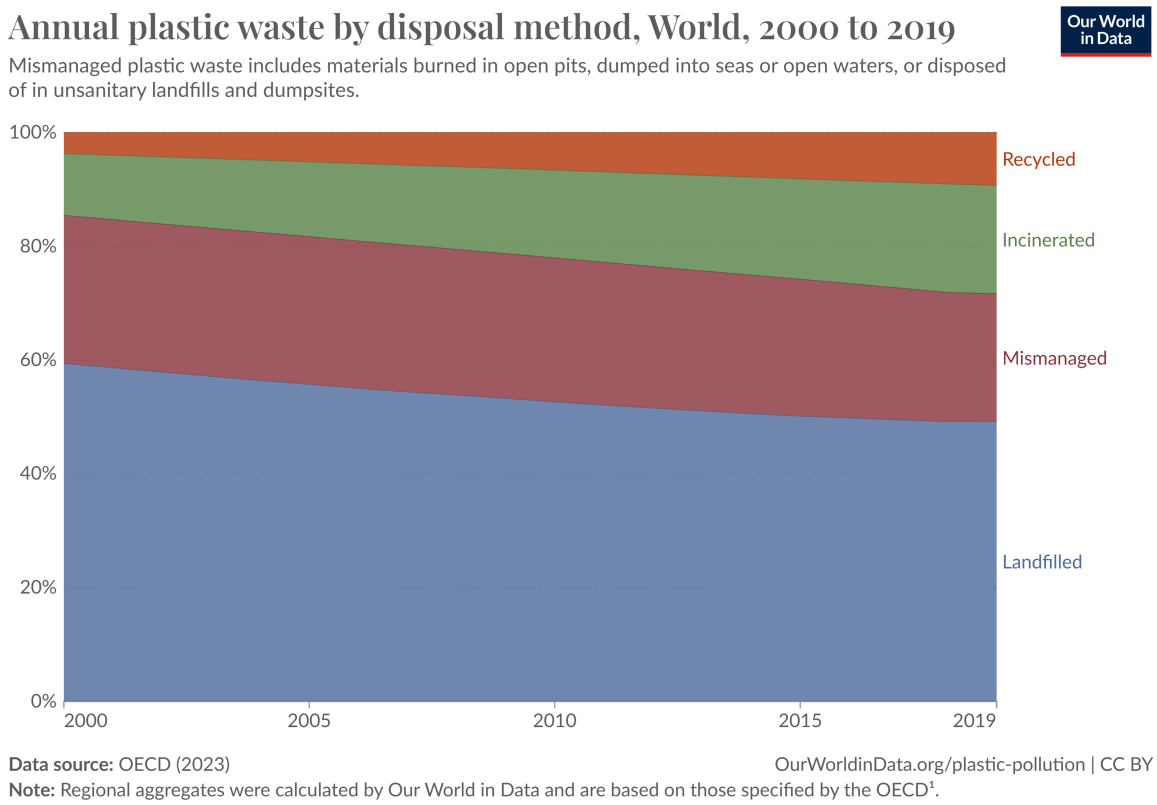

Figure 2.9: Global plastic waste disposal method. Reprint from [101].

Recent advancements have further expanded the scope of photoreforming. For instance, Reisner and colleagues developed a photocatalytic system that enables selective C–H oxidation of tertiary carbons in polystyrene (PS), yielding benzoic acid with approximately 40% efficiency and other aromatic monomers at around 20%[109]. This system operates under mild conditions using blue LED light and has been successfully applied to the gram-scale deconstruction of real-world PS foam. Such innovations demonstrate the potential of photoreforming to not only address plastic waste but also recover valuable chemical products, paving the way for more sustainable plastic management strategies. Interestingly, recent studies suggest that incorporating biological materials into these processes can further enhance plastic degradation efficiency. For example, a variant of leaf-compost cutinase (LCC) has been shown to effectively depolymerize post-consumer PET waste with minimal energy requirements, highlighting its practical applicability in plastic recycling[111].

However, challenges remain in improving both the selectivity and activity of these systems for large-scale applications. In this context, plasmonic catalysis presents an exciting opportunity to enhance catalytic performance in plastic photoreformation. The significant field enhancement, localized heating effects, and the generation of energetic electron-hole carriers introduced by LSPR excitation - all can facilitate chemical transformations. Additionally, plasmonic catalysts possess the unique ability to selectively activate chemical bonds in adsorbed molecules, directing reactions along specific pathways. This selectivity, combined with their ability to harvest visible light efficiently, makes

plasmonic catalysts a promising tool for improving the catalytic performance of plastic photoreforming systems[112]. However, both a desirable catalytic performance and a comprehensive understanding of the underlying mechanisms of plasmon-involved plastic photoreforming are still lacking, requiring further investigation.

3

Methodology

3.1 Synthesis

In this section, the synthesis processes of nanoparticles are described, the spectroscopy images of the prepared nanostructures are presented in Figure 3.1 and also later chapters where they were used in specific studies.

3.1.1 Synthesis of Au NPs.

The synthesis of Au nanocubes (NCs), rhombic dodecahedrons (RDs), and octahedra (OCs) was conducted through a series of well-established procedures based on seed-mediated growth methods[113,114].

Materials. Chemicals used were Ascorbic acid (> 99.0%), Hexadecyltrime thylammonium (CTAB, > 96.0%), Hexadecyltrime thylammonium (CTAB, > 99.0%), Gold (III) Chloride trihydrate (HAuCl4·H_2O, > 99.9%), Sodium borohydride (> 98.0%), Sodium hydroxide (>97%), Sodium carbonate (99.999%), Perchloric acid (70%). All chemicals were used after purchase without any further purification. Milli-Q water at 25 °C was used in all experiments. All glassware was washed with aqua regia, Milli-Q water, and dried before use. Carbon (mesoporous, nano powder graphitized 99.95%, trace metals basis), Nafion (perfluorinated resin solution, 5wt% in lower pliphatic alcohols and water, contains 15-20% water), 2-Propanol (puriss.p.a., ACS reagent. reag. ISO, reag. Ph. Eur., > 99.8% (GC)), Deuterium oxide (deuteration degree min. 99.9% for NMR spectroscopy) and Dimethyl sulfoxide (ACS reagent >/=99.9%) were also purchased from Sigma-Aldrich. Carbon paper (sigracet 39BB and sigracet 39CC) were purchased from Fuel cells Etc.

Au nanocubes. To prepare Au NCs, an aqueous solution of 0.25 mM $HAuCl_4$ and 75 mM CTAB was prepared, followed by the rapid injection of 0.6 mL of 10 mM ice-cold $NaBH_4$ under stirring conditions at 30°C. The resulting brown solution was allowed to stir slowly for 2 hours. Afterward, it was diluted 100-fold with deionized water to create a seed hydrosol. Subsequently, 0.3 mL of the seed solution was added to 25 mL of a growth solution composed of 0.04 mM $HAuCl_4$, 16 mM CTAB, and 6 mM ascorbic acid. The solution was mixed using a vortex mixer for 10 seconds and then left undisturbed at 25°C overnight to promote the formation of Au NC seeds. For the growth of Au NCs,

0.150 mL of 25 mM $HAuCl_4$ was quickly introduced into 8 mL of the seed solution, followed by vortex mixing for 10 seconds. The reaction mixture was then left undisturbed at 30°C for 2 hours, resulting in a red-purple solution, indicating the successful formation of Au NCs.

Au rhombic dodecahedrons. To synthesize Au RDs, a sequential addition of 0.5 mL of 0.1 M ascorbic acid, 0.55 mL of 0.2 mM NaOH, and 0.2 mL of 25 mM $HAuCl_4$ was performed in the previously synthesized Au NC solution. The mixture was then allowed to stand at 30°C for 2 hours until a red-brown colloidal solution was obtained, signifying the formation of Au RDs.

Au octahedra. The synthesis of Au OCs followed a similar seed-mediated approach. The octahedral seed hydrosol was prepared by injecting 0.6 mL of 10 mM ice-cold $NaBH_4$ into a solution containing 87.5 µL of 20 mM $HAuCl_4$ and 7 mL of 75 mM CTAB. After gentle stirring for 3 hours, the seed solution was diluted 100-fold with deionized water. For the first growth stage, 0.15 mL of the octahedral seed hydrosol was added to a growth solution containing 25 µL of 20 mM $HAuCl_4$, 0.387 mL of 38.8 mM ascorbic acid, and 12.1 mL of 16 mM CTAB, vortex-mixed for thorough mixing, and left undisturbed at 25°C overnight. In the second growth stage, 5 mL of the previously obtained solution was added to 12.5 mL of a growth solution containing 16 mM CTAB, 0.04 mM $HAuCl_4$, and 1.2 mM ascorbic acid, and the mixture was left undisturbed overnight. The appearance of a purple color in the solution indicated the successful formation of Au OCs.

3.1.2 Synthesis of Au@TiO_2 core-shell nanostructures.

Materials. The following chemicals were used in the experiments without further purification: Gold (III) chloride trihydrate ($HAuCl_4 \cdot H_2O$, > 99.9%), hexadecyltrimethylammonium bromide (CTAB, > 96.0%), ascorbic acid (> 99.0%), sodium borohydride (> 98.0%), sodium hydroxide (> 97%), sodium bicarbonate (99.7%), titanium(III) chloride solution (10%–15%), and sodium dodecyl sulfate (SDS, > 99.0%). Methanol (> 99.8%, GC), potassium hydrogen phthalate (> 99.95%), potassium iodide (> 99%), ethanol (> 99.8%, GC), and Nafion solution (5 wt% in lower aliphatic alcohols and water, containing 15–20% water) were purchased from Sigma-Aldrich. Milli-Q water was used throughout all experiments, and all glassware was cleaned using aqua regia, rinsed with Milli-Q water, and dried prior to use.

Au cores. Gold rhombic dodecahedrons (Au RDs) and gold nanocubes (Au NCs) were prepared based on a previously reported method[113,115], with an additional step to ensure consistent gold content across samples. Specifically, after completing the initial synthesis, 0.5 mL of 0.1 M ascorbic acid was added to the reaction mixture, followed by 0.2 mL of 25 mM $HAuCl_4$. This adjustment facilitated uniform growth of the subsequent TiO_2 shell on the surfaces of both Au NCs and RDs, enabling precise control over shell thickness.

Au@TiO_2 Core-Shell Nanostructures. The Au@TiO_2 core-shell structures were synthesized with modifications to a previously reported method[116]. First, ligand exchange was performed to replace CTAB on the Au nanostructures with SDS. For this, 4 mL of as-prepared Au NPs stabilized by CTAB were centrifuged to remove excess surfactant and redispersed in 10 mL of Milli-Q water.

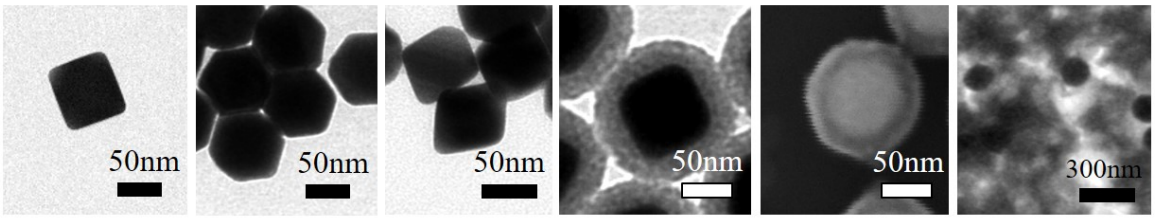

Figure 3.1: Nanostructures mentioned in the chapter of Methods. From left to right: Au cubes, Au rhombic dodecahedron, Au octahedra, Au NC@TiO_2, Au RD@TiO_2 core-shell Nanostructures, and Au-FeSA-MCN composites.

The suspension was added gradually to 10 mL of 0.1 M SDS solution under vigorous stirring and allowed to interact for 30 minutes. After removing excess SDS via centrifugation, the SDS-capped Au nanocrystals were redispersed in 50 µL of Milli-Q water.

For the core-shell synthesis, 20 µL of $TiCl_3$ solution was rapidly added to 6 mL of Milli-Q water under vigorous stirring, followed by 20 µL of 0.1 M $NaHCO_3$ solution. The concentrated SDS-capped Au nanoparticle solution was then introduced into the mixture, which was stirred for 10 minutes to form the Au@TiO_2 structures. The resulting core-shell nanostructures were washed twice with ethanol and subsequently annealed at 400°C for 2 hours in a muffle furnace. This annealing step ensured the formation of anatase TiO_2 and the complete removal of surfactants.

3.1.3 Composite of macroporous CN supported Fe single-atom (MCN-FeSA) and Au nanoparticles.

Au NCs prepared above was used again for the preparation of the composites. Macroporous CN-supported Fe single-atom catalysts (FeSA-MCN) was prepared using an advanced one-pot SiO_2-templated pyrolysis strategy, based on the method described in a previous publication[117]. For a typical preparation process, 20 mg prepared FeSA-MCN was mixed with 2 mg Au nanoparticles (so 10 wt% of Au in the mixture). The mixture was then dispersed in the mixture of 10 mL Isopropanol and 10 mL DI water. suspension was sonicated for 5 min and stirred with 400 rpm overnight. Next day, stop stirring and the pink-white suspension will naturally settle. Romove the supernatant, centrifuge and wash the sediment twice, we got the clean Au-FeSA-MCN composites. Dry them for later annealing. The composites were annealed in N_2 atmosphere at 300°C for 2 hours to improve the interfacial connection between Au nanoparticles and FeSA-MCN.

3.2 Characterization

3.2.1 Microscopies.

Scanning Electron Microscopy (SEM) and Transmission Electron Microscopy (TEM) are the most commonly used microscopic techniques for characterizing nanomaterials. These microscopy techniques, when combined, offer comprehensive insights into the structural, morphological, and compositional properties of nanomaterials, facilitating the understanding and optimization of their functionality

Scanning Electron Microscopy (SEM). SEM provides high-resolution surface imaging by scanning a focused electron beam across a sample and detecting the emitted secondary or backscattered electrons. Therefore it can provide the information about the surface topography of the sample, thus it is particularly useful for studying the morphology and size distribution of nanostructures.

Transmission Electron Microscopy (TEM). TEM operates by transmitting an electron beam through a thin sample and form an image, so the internal structure of the sample can be revealed. High-Resolution TEM (HRTEM) could produce images with atomic-scale resolution, thus allows for the visualization of lattice fringes, enabling the determination of crystal structures and defects at the atomic level. Additionally, Energy-Dispersive X-ray Spectroscopy (EDS) mapping, often integrated with TEM, provides spatially resolved elemental analysis. This capability is crucial for studying the composition and elemental distribution in complex nanostructures, such as core-shell systems

3.2.2 Spectroscopies.

Spectroscopic techniques are essential for understanding the structural, optical, and electronic properties of nanomaterials. Combining with microscopic techniques, they could offer a comprehensive understanding of the material's properties, thus are essential for correlating the characteristics of nanomaterials with their catalytic and functional performance.

Ultraviolet-Visible Spectroscopy (UV-Vis). UV-Vis is a powerful tool for studying the optical properties of nanostructures, providing insights into localized surface plasmon resonance (LSPR) and other light-matter interactions. Besides, the absorption spectra obtained help in understanding the optical response and bandgap characteristics.

X-ray Diffraction (XRD). XRD is a fundamental technique for determining the crystallographic structure and phase purity of materials. When a monochromatic X-ray beam interacts with a crystal, the oscillating electric field of the X-rays induces periodic vibrations in the electrons surrounding the atoms. These vibrating electrons act as secondary sources, emitting spherical electromagnetic waves. The scattered waves generated by the electrons can interfere with each other, leading to the phenomenon of diffraction. The spatial distribution of the diffraction pattern is determined by the size, shape, and orientation of the crystal lattice, while the intensity of the diffraction depends on the

type and arrangement of atoms within the unit cell. Consequently, each crystal produces a unique diffraction pattern that reflects its structural characteristics.

The diffraction of X-rays by a crystal obeys Bragg's law:

$$2d \sin\theta = n\lambda$$

where n is the diffraction order, θ is the angle between the incident X-ray beam and the crystal plane, d represents the interplanar spacing, and λ is the wavelength of the X-rays.

By analyzing the diffraction angles (θ) and the associated intensities obtained from X-ray diffraction (XRD) spectra, the interplanar spacing (d) can be calculated using Bragg's law. This information allows the determination lattice parameters, crystallite size, and any structural changes introduced during synthesis or treatment.

X-ray Photoelectron Spectroscopy (XPS). XPS is employed to analyze the surface chemical composition and oxidation states of elements within a material. The method involves irradiating a sample with X-rays, which excites core electrons from atoms in the material. If the energy of the incident photon exceeds the binding energy of the electron, the electron is ejected as a photoelectron. The kinetic energy of the photoelectron (E_k) is measured, and its binding energy (E_b) is calculated using the relation:

$$E_k = h\nu - E_b - \phi$$

where $h\nu$ is the photon energy and ϕ is the work function of the spectrometer. The binding energy is characteristic of the atom and its chemical environment, therefore, XPS is particularly valuable for investigating chemical bonding, elemental distribution, and surface modifications in complex nanostructures.

Photoluminescence (PL) and Time-Resolved Photoluminescence (TRPL). PL and TRPL are optical techniques used to study the electronic and optical properties of materials. PL involves the excitation of electrons from the valence band or defect states to higher energy levels by a light source, followed by their radiative recombination, emitting photons. The intensity and wavelength of the emitted light are influenced by the material's structure, composition, and defects, making PL a valuable tool for investigating the bandgap, defect states, and electronic transitions within the material. TRPL extends this analysis by measuring the decay dynamics of the photoluminescence over time. This allows for the determination of carrier lifetimes, providing insights into charge carrier recombination mechanisms and the efficiency of charge separation. By analyzing lifetimes associated with radiative and non-radiative processes, TRPL enables a deeper understanding of material performance in applications such as photovoltaics, photocatalysis, and optoelectronics. Both PL and TRPL are critical for assessing the optical and electronic characteristics of materials, particularly in the context of energy conversion and semiconductor research.

4

Crystal Facet Effect in Plasmonic Catalysis

The content of this chapter is published in the scientific journal Nature Communications (Kang, Y., João, S.M., Lin, R., Liu, K., Zhu, L., Fu, J., Cheong, W.C., Lee, S., Frank, K., Nickel, B., Liu, M., Lischner, J. and Cortés, E. Effect of crystal facets in plasmonic catalysis. Nature Communications, 2024, 15(1), 3923.).[115] *As the foundation of the chapter, the peer-reviewed manuscript is used, and text elements are drawn from the publication with rephrase in accordance with the Springer Nature that allows the reprinting of own contributions and in accordance with the terms of the CC-BY Creative Commons Attribution 4.0 International license http://creativecommons.org/licenses/by/4.0/. Large language models are used to refine the grammars.*

4.1 Research background

For several decades, fossil fuels have served as the predominant source of affordable energy; however, their extensive use has led to the emission of significant quantities of CO_2 into the atmosphere, with detrimental implications for both climate change and the global energy landscape. While addressing this issue will necessitate substantial investments in more sustainable energy production methods, a key aspect of this transition is decarbonization. One promising avenue for achieving this goal is artificial photosynthesis, which emulates the natural process of converting CO_2 into chemical fuels utilizing sunlight[118]. Despite its potential, the CO_2 reduction reaction (CO_2RR) remains a complex multi-electron, multi-proton process with numerous reaction pathways, making it difficult to attain high selectivity[119–121]. This challenge has motivated extensive research efforts aimed at enhancing catalytic performance, with various strategies explored, such as altering the composition[121–126], adjusting particle size[122,127], and optimizing geometric configurations[120,128–130], in addition to modifying the exposed crystal facets[131–133] of the catalytic materials. Among these approaches, the influence of crystal facets is particularly significant, as they can play a decisive role in determining both the activity and selectivity of catalysts. This is achieved through the modulation of factors like atomic arrangement[134]

and the adsorption energies of reaction intermediates[135,136]. Furthermore, distinct facets can exhibit varied physical properties, including variations in work function[137], electronic states[138], and electron mean free path[139]. In recent years, growing attention has been devoted to investigating the facet effect on heterogeneous catalysts, across a range of catalytic processes, including thermocatalysis[140–142], electrocatalysis[134,135,143–153], photocatalysis[154,155] and photo-electrocatalysis[156,157]. A seminal study by Hori et al., conducted in 1995, examined the facet effect of single-crystal platinum (Pt) in electrocatalytic CO_2RR systems. Their findings revealed that the CO production rate on Pt (110) was more than ten times higher than that on Pt (111), underscoring the potential of facet engineering in optimizing both the selectivity and activity of catalysts for CO_2RR[144].

Simultaneously, the rise of plasmonic catalysis as a novel and rapidly expanding sub-discipline within heterogeneous catalysis has attracted considerable attention due to its unique properties and potential to improve both activity and selectivity across a variety of catalytic reactions. Plasmonic catalysis operates through the excitation of localized surface plasmons (LSPs), which occur as conduction electrons within nanoparticles oscillate resonantly in response to incident light. At the resonance frequency, known as localized surface plasmon resonance (LSPR), nanoparticles concentrate electromagnetic fields at their surfaces, resulting in substantial field intensification. This enhanced electromagnetic field subsequently leads to the decay of surface plasmons into energetic electron-hole pairs via Landau damping. These high-energy charge carriers can then be transferred to unoccupied orbitals of adsorbed molecules on the catalyst surface, facilitating chemical transformations or selective desorption, among others[158,159]. In addition to these electronic effects, plasmonic catalysts may enable the selective activation of specific chemical bonds in adsorbed molecules, thus allowing the exploration of targeted reaction pathways[159–161]. Furthermore, the temperature increase associated with plasmon decay can contribute further to driving the catalytic reaction[162,163]. A wide array of reactions has been investigated within this framework, including H_2 dissociation[164,165], O_2 activation[166], N_2 dissociation[167], H_2 evolution[168], as well as CO_2RR[169]. These studies have consistently demonstrated the capacity of plasmonic catalysis to enhance reaction efficiency or even alter the reaction pathways[124,170,171]. Beyond its influence on chemical reactivity, the LSPR effect offers a high degree of tunability, enabling the manipulation of light absorption at nanometer and femtosecond scales[172]. These characteristics position plasmonic catalysis as a promising approach for improving the efficiency and selectivity of solar energy-driven chemical processes[173]. However, despite its potential, the strategic design of plasmonic catalysts remains in its early stages, necessitating further research to optimize their performance.

Given this context, the primary objective of our study is to investigate the influence of crystal facets on plasmonic CO_2RR, building upon the established importance of facet effects in thermal catalysis, electrocatalysis, and photocatalysis. To this end, we synthesized three distinct morphologies of gold nanoparticles (Au NPs)—nanocubes (NCs), rhombic dodecahedrons (RDs), and octahedra (OCs)—all of which were prepared with identical phase, size, and LSPR position, but with different exposed crystal facets. The electrocatalytic CO_2RR behavior of these three Au NP morphologies varied considerably, a result attributed to differences in CO_2 activation energies on each of the exposed crystal facets, as

corroborated by density functional theory (DFT) calculations. However, when introducing plasmon excitation into the system, a notable enhancement in CO selectivity was observed for both Au OCs and NCs, whereas the RDs exhibited no significant improvement. To elucidate the underlying mechanisms behind this disparity, we conducted large-scale atomistic simulations and electric field modeling. Our findings suggest that the catalytic response to plasmonic excitation is primarily governed by the quantity and spatial distribution of hot carriers and electric field enhancements generated by plasmons. In particular, edges and corners play a crucial role, while the contribution of exposed facets appears to be minimal. These insights may provide a pathway for advancing the design of plasmonic catalysts, potentially enabling the direct utilization of sunlight for decarbonization processes.

4.2 Results and discussion

Synthesis and characterization of Au NPs.

Gold nanocrystals with three different exposed facets - {100}, {110} and {111} - were synthesized using seed-mediated growth methods in the presence of cetyltrimethylammonium bromide (CTAB) as a surfactant[113,114]. These different exposed facets correspond to distinct nanocrystal morphologies: nanocubes (NCs) for the {100} facet, rhombic dodecahedra (RDs) for the {110} facet, and octahedra (OCs) for the {111} facet. The detailed protocols for synthesizing each of these morphologies are outlined in the Methods section. Figures 4.1(a-c) and Figure 4.2 present scanning electron microscopy (SEM) and transmission electron microscopy (TEM) images, demonstrating the monodispersed shapes and sizes of the single-crystalline gold nanocrystals. All three nanocrystal morphologies—NCs, RDs, and OCs—were found to have an average size of approximately 60 nm (as further shown in Figure 4.3). The face-centered cubic (FCC) phase common to all three Au nanoparticle morphologies was confirmed via X-ray diffraction (XRD) analysis, with corresponding data shown in Figure 4.1(g). To gain a deeper understanding of the surface structures, high-resolution transmission electron microscopy (HRTEM) and selected area electron diffraction (SAED) were utilized, as depicted in Figures 4.1(d-f). The measured d-spacing values in the HRTEM images—0.209 nm for Au NCs, 0.141 nm for RDs, and 0.242 nm for OCs—are consistent with the surface termination of the {100}, {110}, and {111} facets in the FCC phase, as summarized in Appendix. The SAED patterns displayed sharp, well-defined diffraction spots, further confirming the single-crystalline nature of the synthesized Au nanoparticles. These structural characterizations align with previous literature on Au nanocrystals and their facet-specific properties[113]. In addition to the structural analysis, UV–vis–NIR absorption spectroscopy was employed to study the optical properties of the Au nanocrystals. As shown in Figure 4.1(h), all three samples exhibited extinction spectra with a distinct peak around 540 nm, indicating the presence of a single localized surface plasmon resonance (LSPR) mode at a similar excitation wavelength for each morphology. The sharpness of these peaks corroborates the uniformity in particle size, as evidenced by the SEM and HRTEM analyses. These results collectively confirm the successful synthesis of monodisperse, single-crystalline gold nanocrystals with well-defined facets and optical properties.

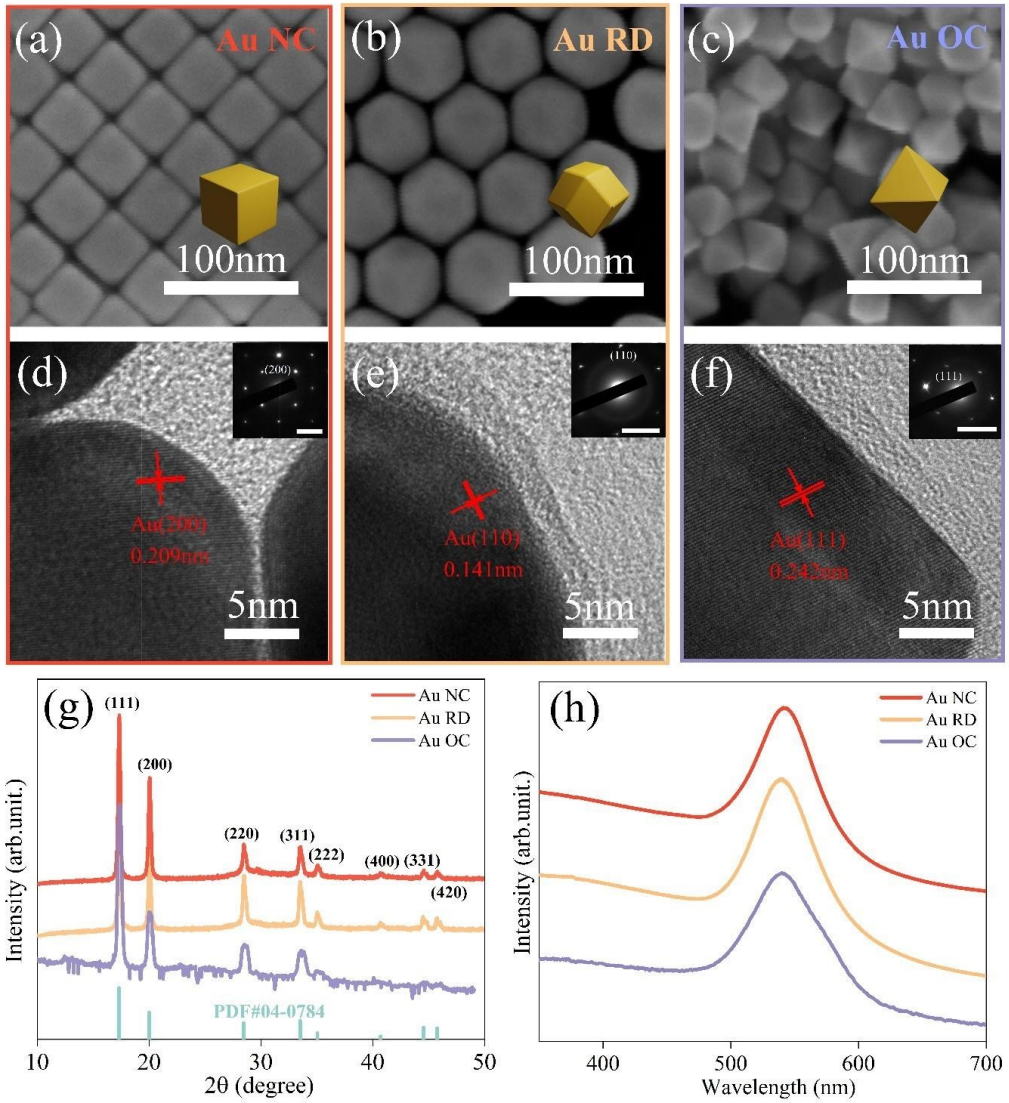

Figure 4.1: Characterization of Au Nanoparticles. a-c. Scanning electron microscopy (SEM) images of Au nanocubes (NCs) (a), rhombic dodecahedra (RDs) (b), and octahedra (OCs) (c). **d-f** High-resolution transmission electron microscopy (HRTEM) images and selected area electron diffraction (SAED) patterns (insets) for Au NCs (d), RDs (e), and OCs (f). The scale bars in the insets represent 5 1/nm. The average distances between the fringes in the HRTEM images and the corresponding Au facets are marked in red. **g.** X-ray diffraction (XRD) patterns of Au NCs (red), RDs (yellow), and OCs (purple), along with the expected XRD pattern for Au in the face-centered cubic (FCC) phase using Mo Kα radiation. **h.** Extinction spectra for Au NCs, RDs, and OCs, each exhibiting localized surface plasmon resonance peaks at 543 nm, 539 nm, and 542 nm, respectively.

Electrocatalytic performance of Au NPs.

The CO_2 reduction reaction (CO_2RR) holds great promise as a potential solution to mitigating the excessive carbon dioxide levels in the atmosphere. However, significant challenges remain, particularly

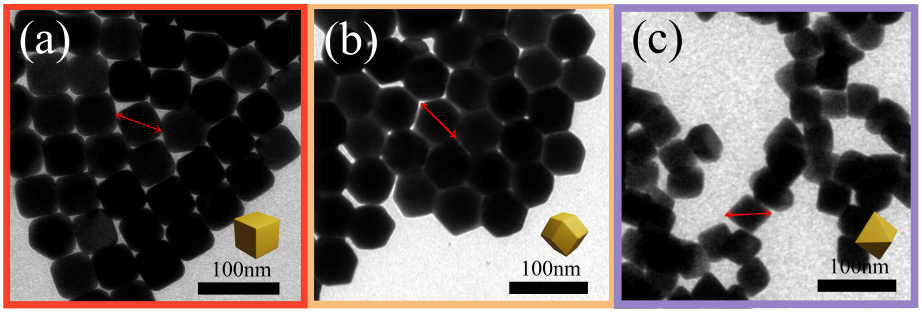

Figure 4.2: TEM images of (a) Au NCs (b) Au RDs and (c) Au OCs. The red arrow indicators within the figure delineate the dimensions that were measured for size distribution shown in Figure 4.3.

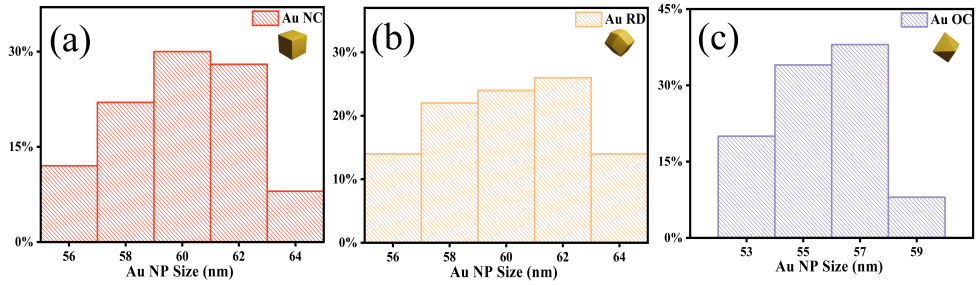

Figure 4.3: Size distribution of (a) Au NCs (b) Au RDs and (c) Au OCs. The dimensions that were measured were delineated by the red arrow indicators in Figure 4.2. By conducting 100 measurements on Au NPs from distinct synthesizing batches, average sizes of NC 60nm, RD 60nm and OC 56nm were ascertained.

related to the high activation energy required and the limited selectivity of the process. Gold has emerged as a highly favorable catalyst for CO_2RR due to its relatively low activation energy and excellent selectivity for CO production. In light of this, we conducted a series of experiments to evaluate the electrocatalytic performance of Au nanoparticles with three distinct exposed crystal facets: {100} in nanocubes (NCs), {110} in rhombic dodecahedra (RDs), and {111} in octahedra (OCs). As previously discussed, we synthesized Au nanostructures with identical face-centered cubic (FCC) phases, similar particle sizes, and nearly identical LSPR wavelengths. To assess their electrocatalytic performance in CO_2RR, we examined current-time (i-t) curves, linear sweep voltammetry (LSV) measurements, and corresponding Tafel plots, which are provided in Figures 4.9 and 4.10. Across the range of applied potentials (from -0.53 V_{RHE} to -0.88 V_{RHE} with the step of -0.07 V_{RHE}), the primary gas products detected were carbon monoxide (CO) and hydrogen (H_2). No liquid products were observed, as confirmed by proton nuclear magnetic resonance (^{1}H NMR) and no products were detected (see Figure 4.4).

Control experiments using carbon powder on carbon paper verified that the catalytic activity originated from the Au NPs rather than the carbon substrate (Figure 4.5). Further validation using

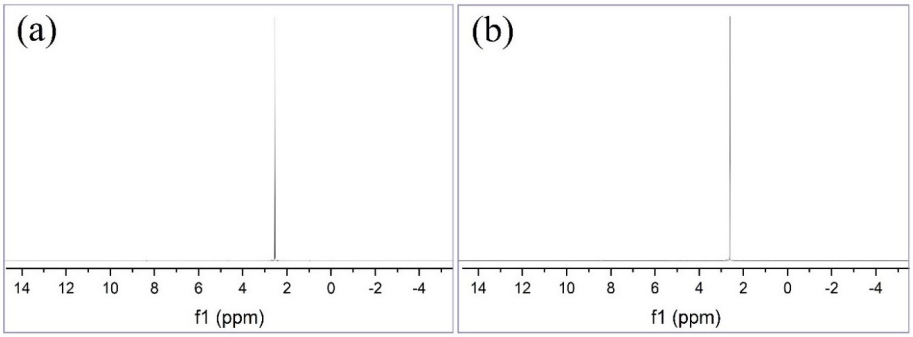

Figure 4.4: ^{1}H NMR spectrum of electrolyte after CO_2RR measurement on Au OCs (a) in dark conditions, (b) with constant 525 nm LED illumination. In our system, the internal standard DMSO showed its chemical shift at 2.6 ppm in the spectrum. For other Au NPs, the spectrum are similar to OCs. No obvious peak corresponding to liquid products is observed on all three Au NPs in both situations.

argon (Ar) bubbling confirmed that the detected CO was exclusively the result of CO_2 reduction, ruling out any contribution from ligand decomposition (see Figure 4.6).

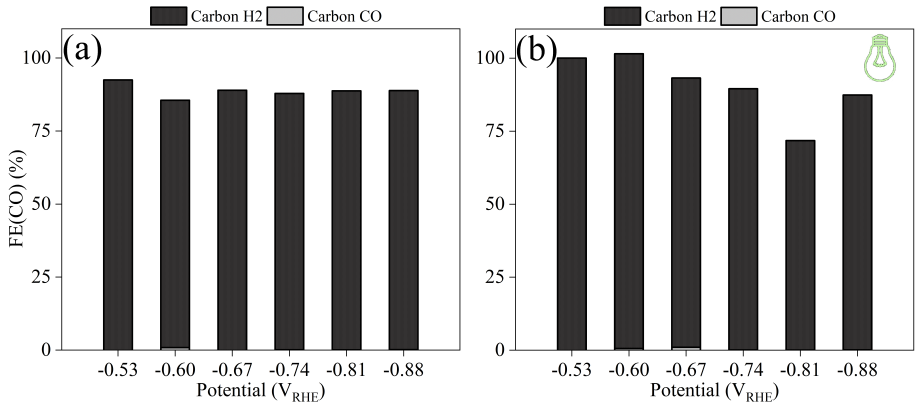

Figure 4.5: Control experiment of CO_2RR system based on carbon. FE(CO) and FE(H_2) (a) in dark condition, (b) with 525 nm illumination.

The faradaic efficiency of CO (FE(CO)) and H_2 (FE(H_2)) along with the corresponding partial current densities for the three Au nanoparticle types (NCs, RDs, and OCs) are presented in Figures 4.7a and 4.8. Our results reveal significant differences in the CO_2RR selectivity among the three types of Au NPs. Au RDs with the {110} facet exhibited the highest CO selectivity, with FE(CO) reaching approximately 94% at an applied potential of -0.67 V_{RHE} across the entire potential range studied. In comparison, Au NCs with the {100} facet displayed a lower CO selectivity at the same potential (FE(CO) as 69%), while Au OCs with the {111} facet demonstrated the lowest selectivity among the three, with FE(CO) around 51% at -0.67 V_{RHE}. The long-term performance over a 5-hour period, as depicted in the i-t curves in Figure 4.11, shows that the order of FE(CO) selectivity remained consistent, with Au

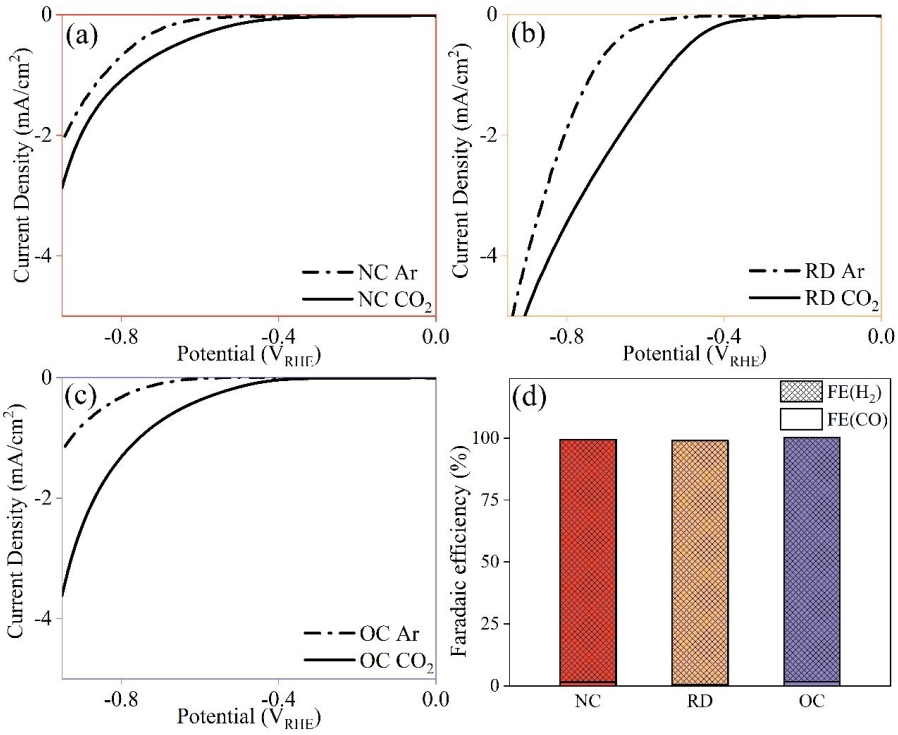

Figure 4.6: Control experiment under Ar bubbling. (a-c) Current density under CO_2 and Ar on (a) NCs, (b) RDs and (c) OCs. (d) Corresponding FE of gaseous products.

RDs exhibiting the highest performance, followed by NCs and OCs, confirming the high stability of the system.

Density functional theory (DFT) calculations were conducted to gain deeper insight into the factors driving the varying electrocatalytic CO_2 reduction performance across the three types of Au nanoparticles. Full details of the computational approach are provided in the Methods section. The calculations confirmed that the activation of CO_2, specifically the formation of the COOH* intermediate, is the rate-determining step in the reaction mechanism, as illustrated in Figure 4.14. The computed formation energies of COOH* on the different Au facets revealed significant differences: on Au{110} (RDs), the formation energy was found to be 1.1 eV, compared to 1.2 eV on Au{100} (NCs) and 1.4 eV on Au{111} (OCs). The lower COOH* formation energy on Au{110} suggests a more favorable CO_2 activation process, facilitating enhanced CO production. This trend aligns well with the experimental findings, where Au RDs with the {110} facet exhibited the highest FE(CO). In contrast, Au NCs with {100} and Au OCs with {111} facets demonstrated progressively higher energy barriers for COOH* formation, which corresponded to lower CO selectivity in the electrocatalytic CO_2 reduction reaction[134].

Plasmon-assisted electrocatalytic performance of Au NPs with different exposed crystal facets.

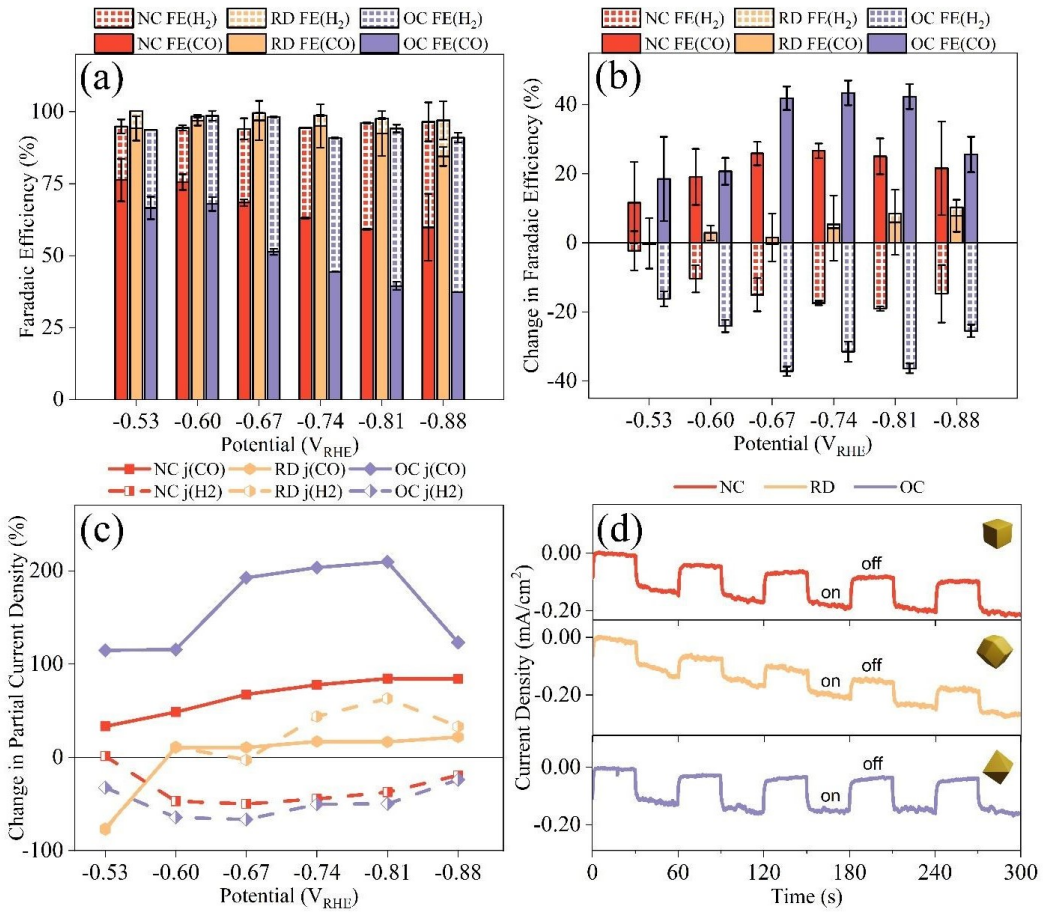

Figure 4.7: (Plasmon-assisted) Electrocatalytic CO_2RR Performance of Au NPs. a. Faradaic efficiency (FE) for CO (solid) and H_2 (square grid) production on Au NCs (red), RDs (yellow), and OCs (purple) in CO_2 reduction experiments. Error bars represent the standard deviation from three independent measurements. **b.** Change in the absolute value of FE for CO and H_2 [$FE_{light} - FE_{dark}$] on Au NPs under illumination by a 525 nm LED. **c.** Percentage change in the partial current density for CO (solid line) and H_2 (dotted line) [$(j_{light} - j_{dark})/j_{dark} 100\%$] on Au NPs under illumination. **d.** Chopped-light chronoamperometry with a 525 nm LED at -0.81 V_{RHE} on Au NPs.

Recent advances in plasmon excitation have introduced new avenues for enhancing the electrocatalytic activity and selectivity of photoactive materials across a range of reactions. To explore the effects of plasmonic enhancement in our system, we studied the plasmon-assisted electrocatalytic CO_2RR on Au NPs was subsequently studied. For this, a light-emitting diode (LED) emitting at a wavelength of 525 nm—corresponding closely to the localized surface plasmon resonance peaks of the Au NPs—was employed as the illumination source. The cathode was illuminated with a continuous light intensity of 610 mW/cm². The corresponding current-time (i-t) and linear sweep voltammetry (LSV) curves under illumination are displayed in Figures 4.9 and 4.10. As observed in the dark electrocatalytic CO_2RR, the main gaseous products during plasmon-assisted catalysis were CO and H_2, with no liquid products detected via proton nuclear magnetic resonance, as shown in Figure 4.4. Control experiments using

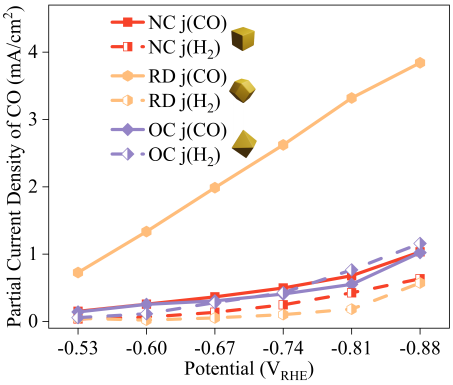

Figure 4.8: Partial current density of CO and H_2 on Au NCs, RDs and OCs in electrocatalytic CO_2RR system.

carbon powder, outlined in Figure 4.5, ensured that the catalytic activity was not influenced by the carbon support material.

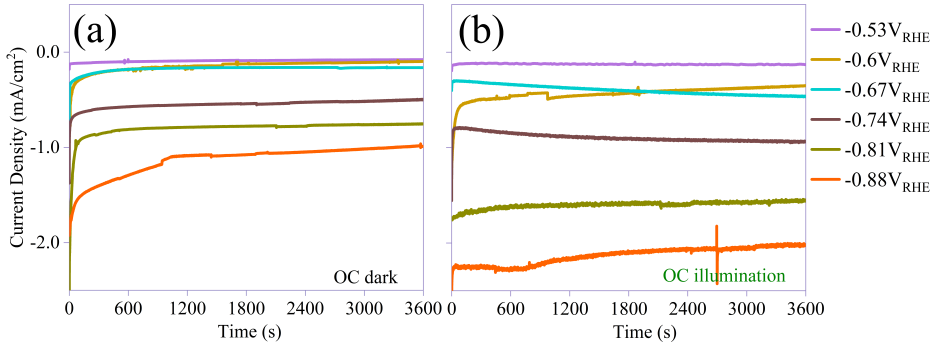

Figure 4.9: Current density on Au NCs in 3600 seconds time in CO_2RR system under potentials from -0.53V_{RHE} to -0.88V_{RHE} with a step of 0.07V_{RHE} (a) in dark and (b) with illumination.

The impact of plasmon excitation on the catalytic selectivity and activity of the Au NPs is illustrated in Figures 4.7(b-c). Although Au OCs initially exhibited the lowest FE(CO) during dark electrocatalytic CO_2RR, the excitation of plasmons significantly improved their selectivity. Upon illumination, the FE(CO) on Au OCs increased by at least 19% at all tested potentials compared to dark conditions. Most notably, the FE(CO) nearly doubled at -0.81 V_{RHE}, rising from 44% in the dark to 87% under illumination. Au NCs also displayed an enhancement in FE(CO) upon illumination, with improvements ranging from 12% to 27% across all applied potentials. In contrast, Au RDs, which exhibited the highest FE(CO) in dark electrocatalysis, showed only minimal improvement upon plasmon excitation. In most cases, the increase in FE(CO) for Au RDs was below 5%. Parallel to these changes, the FE(H_2) decreased notably for both Au OCs and NCs under illumination, as shown in Figure 4.7(b), indicating the suppression of the competitive hydrogen evolution reaction (HER). Conversely, Au RDs showed a slight increase in

FE(H_2) at higher potentials, but this enhancement was much less significant compared to the increase in FE(CO) observed for the other nanoparticle morphologies.

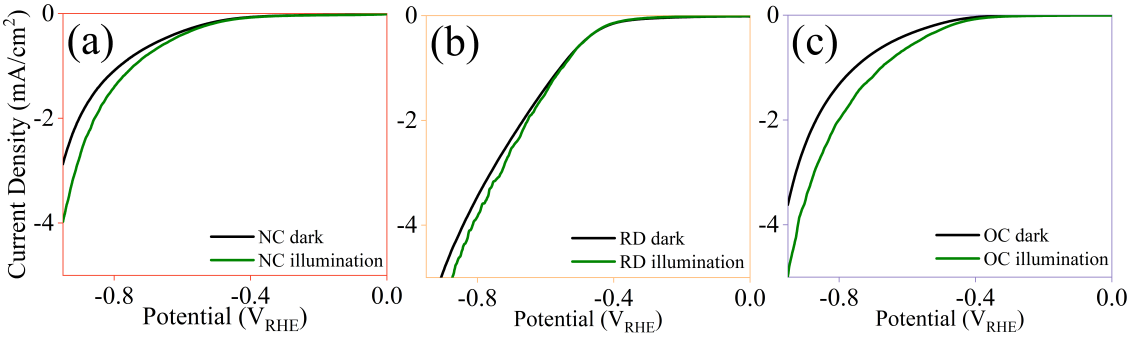

Figure 4.10: LSV curves and Tafel plots of (a, d) Au NCs, (b, e) Au RDs and (c, f) Au OCs in CO_2RR system in dark conditions (black) and with 525 nm LED lightening (green).

The partial current density of CO (j(CO)) on Au OCs and NCs exhibited a significant increase under illumination, as illustrated in Figure 4.7c. At an applied potential of -0.81 V_{RHE}, Au OCs experienced a striking 210% enhancement in j(CO) upon plasmon excitation compared to their performance under pure electrocatalytic conditions. Similarly, Au NCs showed an 84% improvement at the same potential when plasmons were introduced. In contrast, Au RDs displayed only a modest 16% increase in j(CO) in response to light.

The chopped current-time (i-t) curves for the three Au NPs, shown in Figure 4.7d, further confirm the substantial increase in current induced by light. Both Au OCs and NCs demonstrated prominent plasmon-induced photocurrents of 0.12 mA/cm^2 and 0.11 mA/cm^2, respectively, indicating a robust photoresponse. Conversely, Au RDs exhibited a lower photocurrent response of 0.08 mA/cm^2, reflecting their relatively poor interaction with light. In summary, plasmon excitation during electrocatalytic CO_2RR led to considerable improvements in activity and selectivity towards CO on Au OCs and NCs. However, despite Au RDs having the highest intrinsic electrocatalytic performance in dark conditions, they showed minimal enhancement under light exposure, with only slight gains in photocurrent and selectivity. This discrepancy underscores the crucial role of plasmonic effects in boosting the performance of certain nanostructures over others.

Study of the mechanism behind plasmon-enhanced electrocatalytic CO_2RR.

To uncover the mechanism behind the plasmonic enhancement observed in our Au nanoparticle (NP) electrocatalytic systems, we examined the role of hot carriers and heat generation following LSPR excitation. Upon plasmon excitation, non-radiative decay generates energetic “hot” electrons and holes[174–176]which can transfer to adsorbed molecules on the NP surface, facilitating catalytic reactions. In parallel, electron-electron and electron-phonon interactions result in an increase in surface temperature, potentially accelerating reaction rates following the Arrhenius law. To assess whether heat plays a significant role in the enhanced activity and selectivity observed during plasmon-

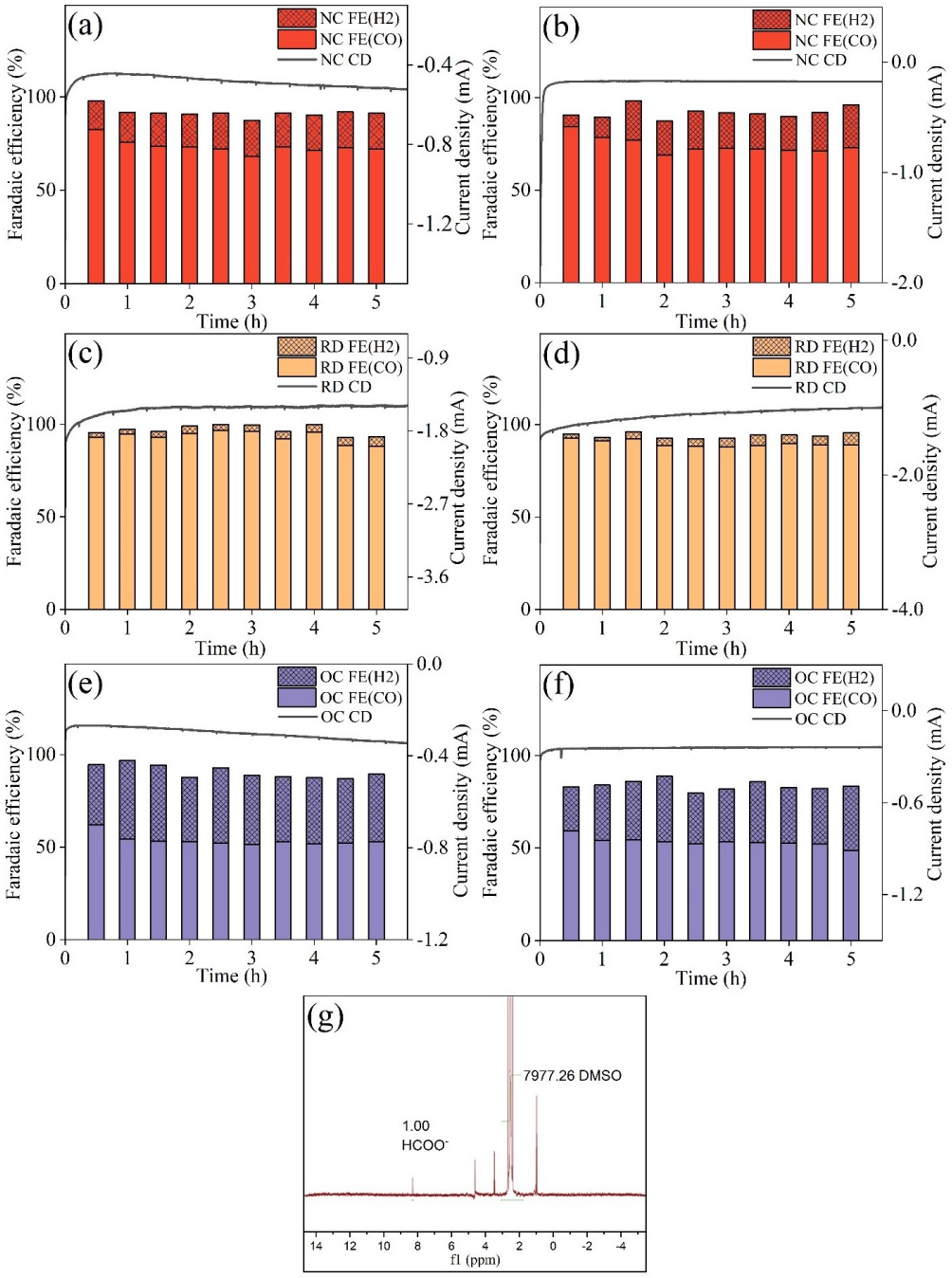

Figure 4.11: Long term electrocatalytic CO_2 reduction. Faradaic efficiencies (FE) of CO and H_2 production as well as the corresponding current density on Au NCs (red), RDs (yellow) and OCs (purple) in long term (5h) electrocatalytic CO_2 reduction system under (a,c,e) -0.67 V_{RHE} and (b,d,f) -0.74V_{RHE}. (g) A typical ^{1}H NMR spectrum of the electrolyte after 5h of experiments. For all rounds, only very limited amount of HCOO- was detected and the corresponding FE were all less than 1%.

assisted CO_2 reduction (CO_2RR), we conducted a series of temperature-dependent electrocatalytic experiments in the dark.

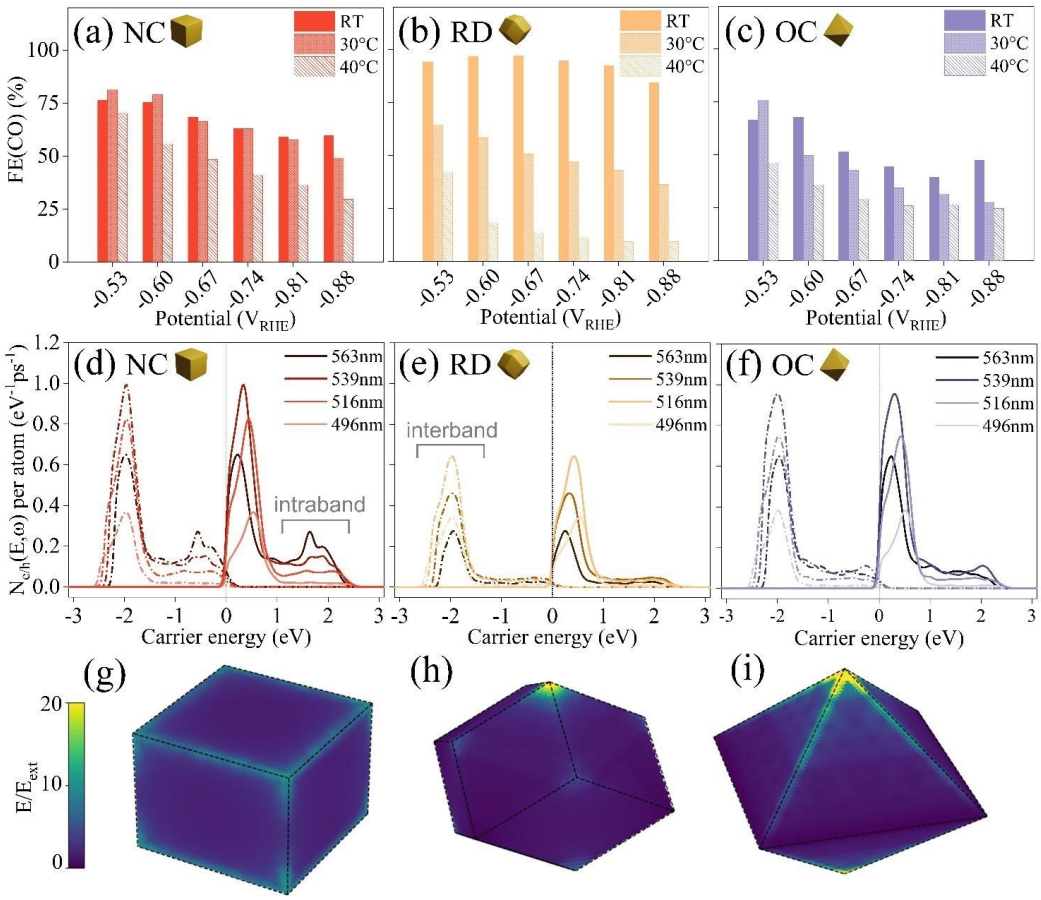

Figure 4.12: Mechanistic investigation of plasmonic electrocatalytic CO_2RR on Au NPs. a-c. Faradaic efficiencies (FE) for CO production at different applied potentials on Au NCs (a), RDs (b), and OCs (c) at room temperature (solid), 30°C (dense slash), and 40°C (sparse slash). **d-f.** Hot electron (solid) and hole (dashed) generation rates for Au NCs (d), RDs (e), and OCs (f) at different electric field wavelengths. Ne/h(E, ω) denotes the number of hot carriers generated with energy E upon excitation with light of frequency ω. The Fermi energy is set to zero. **g-i.** Absolute electric field profile for Au NCs (g), RDs (h), and OCs (i) at their corresponding LSPR frequencies, relative to the externally applied electric field. All simulated NPs consist of approximately 200,000 atoms.

These were performed at room temperature (23°C), 30°C, and 40°C using external heating. The results, depicted in Figure 4.12(a-c), reveal an inverse relationship between temperature and faradaic efficiency for CO production. As temperature increased, selectivity towards CO decreased significantly, with hydrogen evolution reaction (HER) becoming more dominant. For example, at -0.67 V_{RHE}, the FE(CO) for Au RDs dropped from 94% at room temperature to 51% at 30°C and further to just 13% at 40°C. This trend was observed consistently across all three Au NPs, suggesting that elevated temperatures generally reduce CO selectivity in favor of HER. We then estimated the surface temperature during plasmon excitation to be approximately 70°C[177]. However, at this elevated temperature, the CO_2RR

performance under dark conditions was significantly worse, as depicted in Figure 4.13. The FE(CO) was notably lower at high temperatures, attributed in part to the reduced solubility of CO_2, which drops nearly fourfold when the temperature rises from 20°C to 70°C. As an illustrative comparison, at -0.81 V_{RHE}, the FE(CO) for Au OCs under plasmon excitation reached 87%, whereas under dark conditions at a similar surface temperature (70°C), the FE(CO) dropped to only 5%. This contrast highlights the large impact of plasmonic excitation, which counteracts the detrimental effects of reduced CO_2 solubility and reduced CO selectivity typically seen with thermal increases.

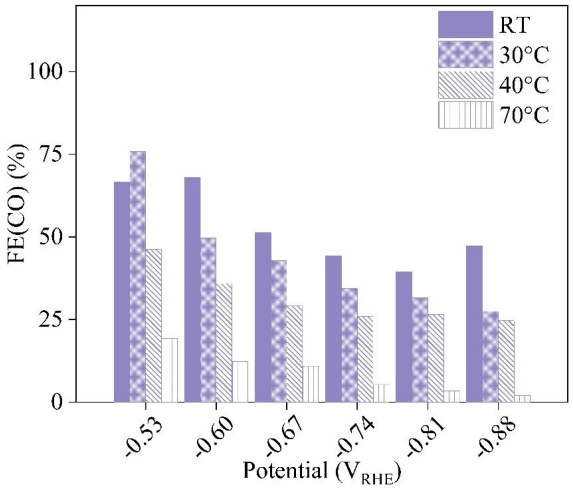

Figure 4.13: Measurement under various temperature. FE(CO) on Au OCs under room temperature, 30°C, 40°C and 70°C.

Thus, while localized heating is a common feature in LSPR-involved systems, it had an opposite effect in our study, where increased temperature decreased CO_2 reduction selectivity. This observation reinforces the conclusion that the plasmonic effects observed here are largely non-thermal, and they offer unique advantages over traditional thermal catalysis. The enhancement in CO selectivity under plasmon excitation cannot be achieved through thermal means alone, underscoring the distinct potential of plasmonic catalysis in driving efficient and selective CO_2RR[178,179].

Given that heat is not the primary cause of the enhanced catalytic effects under illumination, we shifted our focus to the role of "hot carriers" generated after plasmon dephasing. With the help from our collaborator Simão M João and Johannes Lischner, we did the Large-scale Atomistic Simulation. Hot carriers—electrons and holes with high energy—can transfer to adsorbed molecules, playing a crucial role in plasmonic catalytic processes. Relevant for our study is the well-known sensibility of hot carriers on the geometry of the plasmonic catalyst[180]. In the context of CO_2 reduction, these hot carriers may promote the desorption of CO from the catalyst surface, freeing up CO-active sites and increasing the current density as well as the FE(CO). Additionally, they could assist in the activation of adsorbed CO_2 molecules, further driving the reaction. To investigate the role of hot carriers in our system, we calculated the rate of hot carrier generation for Au NCs, OCs, and RDs. The method used was based on the recent approach developed by Jin and coworkers[181]. In this approach, the electric

potential induced by light is first computed using a quasistatic approximation, which is then used to evaluate Fermi's golden rule (FGR). This rule, governing transitions between quantum states, was calculated using large-scale atomistic tight-binding simulations, with each nanoparticle containing approximately 200,000 Au atoms (see Methods section for more details). Figure 4.12(d-f) illustrates the distribution of hot electrons and hot holes generated within the three different Au nanoparticle geometries. The plots reveal strong peaks linked to interband transitions from states with d-band character to sp-band states. Additionally, smaller peaks, particularly noticeable for Au NCs, are attributed to intraband transitions between initial and final states both within the sp band. These smaller peaks are surface-enabled transitions that are amplified by the electric field enhancement at the nanoparticle surface, which is particularly strong in plasmonic systems.

Our findings indicate that Au RDs generate fewer hot carriers compared to Au NCs and OCs, which display similar levels of hot carrier generation. This disparity in hot carrier production can be attributed to the significant influence of electric field enhancement on the surfaces of plasmonic nanomaterials. Given the direct relationship between hot electron transfer and local electric field conditions, we analyzed the electric field distribution near the surfaces of the different Au nanoparticle shapes, as illustrated in Figure 4.12(g-i). In our observations, both Au OCs and NCs exhibit more substantial electric field enhancements at their edges and corners compared to Au RDs. This difference explains why Au NCs generate a larger portion of intraband transitions, increasing from 10% of total transitions at 496 nm to 32% at 563 nm. In contrast, the Au RDs demonstrate a smaller increase, from 6% to 15%, and Au OCs show a range from 7% to 17%. For the purposes of our analysis, electrons were classified as resulting from intraband transitions if their energies exceeded 1.2 eV, with specific population values provided in Table 4.1. Large-scale atomistic simulations and electromagnetic modeling, supported by experimental data showing weaker light responses in RDs compared to NCs and OCs, underscore the importance of hot carriers and electric field enhancement in plasmonic catalytic processes. Interestingly, while facets mainly determine the dark electrocatalytic performance of Au OCs, NCs, and RDs during CO_2RR, uncoordinated sites—such as edges—are the primary contributors to plasmon-assisted CO_2RR. This finding highlights a significant aspect of plasmonic catalysis, revealing that the sites responsible for catalytic activity under plasmonic excitation differ from those contributing to activity in dark conditions[162,182].

Table 4.1: Population of hot carriers of intra- and interband transitions.

Au NP sample	563 nm		539 nm		516 nm		496 nm	
	Inter	**Intra**	**Inter**	**Intra**	**Inter**	**Intra**	**Inter**	**Intra**
Au NCs	68%	32%	80%	20%	85%	15%	90%	10%
Au RDs	85%	15%	85%	15%	91%	9%	94%	6%
Au OCs	83%	17%	85%	15%	89%	11%	93%	7%

The plasmon-induced electric field enhancement is notably influenced by the precise geometry of the nanostructures[158]. In our study, pronounced enhancements were observed at low-coordination

sites, particularly corners and edges, rather than on the facets themselves. This observation aligns with previous studies demonstrating that hot electrons tend to concentrate at lower-coordinated sites, such as edges, rather than at higher-coordinated facets[183]. Recent investigations employing single-particle electron energy loss spectroscopy have confirmed the spatially inhomogeneous efficiency of carrier extraction in plasmonic nanostructures[184].

Moreover, the role of low-coordinated sites has been well-documented, showcasing their superiority over facets in catalytic processes, including CO_2RR systems[184,185]. However, as demonstrated in Figure 4.7, facets primarily dictate the dark response of our system, while the activation under light shifts the energetic landscape of the reaction towards edges and corners.

Notably, investigations into the impact of low-coordinated sites have established their superiority over facets in catalytic processes[186], including CO_2RR system[184,185]. However, as shown in Figure 4.7, in our system facets dominate the dark response, while under light activation the energetics of the reaction is dominated by edges and corners. To elucidate this change in reactivity, we conducted density functional theory (DFT) simulations examining the CO_2RR activity at edge and tip sites, as shown in Figure 4.14. Remarkably, we found that the activation energy on the edges (0.65 eV) is comparable to that on the Au{110} facet exposed by Au RDs (0.64 eV). This similarity suggests that while plasmon-induced hot electrons generated at the edges have a limited impact on enhancing FE(CO), the activation energies for Au OCs {111} (0.74 eV) and NCs {100} (0.68 eV) are higher than that at the edges (0.65 eV). Consequently, for Au NCs and OCs, edges with low coordination numbers serve as critical sites where highly active CO_2RR sites coincide with elevated electric fields and abundant hot electrons once activated by light.

This plasmon excitation significantly improves the reactivity of these systems, allowing for active sites with lower activation barriers than those observed in dark conditions. The efficient transfer of hot electrons to adsorbed CO_2 molecules facilitates their activation, leading to a marked enhancement in both the activity and selectivity of CO_2RR. Although these edge sites are also present during dark experiments, our findings indicate that they become significantly more active under plasmonic excitation, dominating the overall catalytic response of the system. This mechanism is summarized in Figure 4.15. As a result, Au nanoparticles with a higher edge-to-facet ratio, such as Au OCs (supported by calculations and values in Table 4.2), are anticipated to exhibit the most pronounced plasmonic response in CO_2RR, consistent with our experimental observations.

Table 4.2: Edge/facet ratio of Au NPs.

Au NPs on electrodes	**NC**	**OC**	**RD**
Edge length a **(nm)**	42.4	39.6	40.0
Area of edge	$24 \times a \times r$	$24 \times a \times r$	$74 \times a \times r$
Area of facet	$6 \times a^2$	$2\sqrt{3} \times a^2$	$8\sqrt{2} \times a^2$
Edge/facet ratio	1.36×10^{-2}	2.52×10^{-2}	2.35×10^{-2}

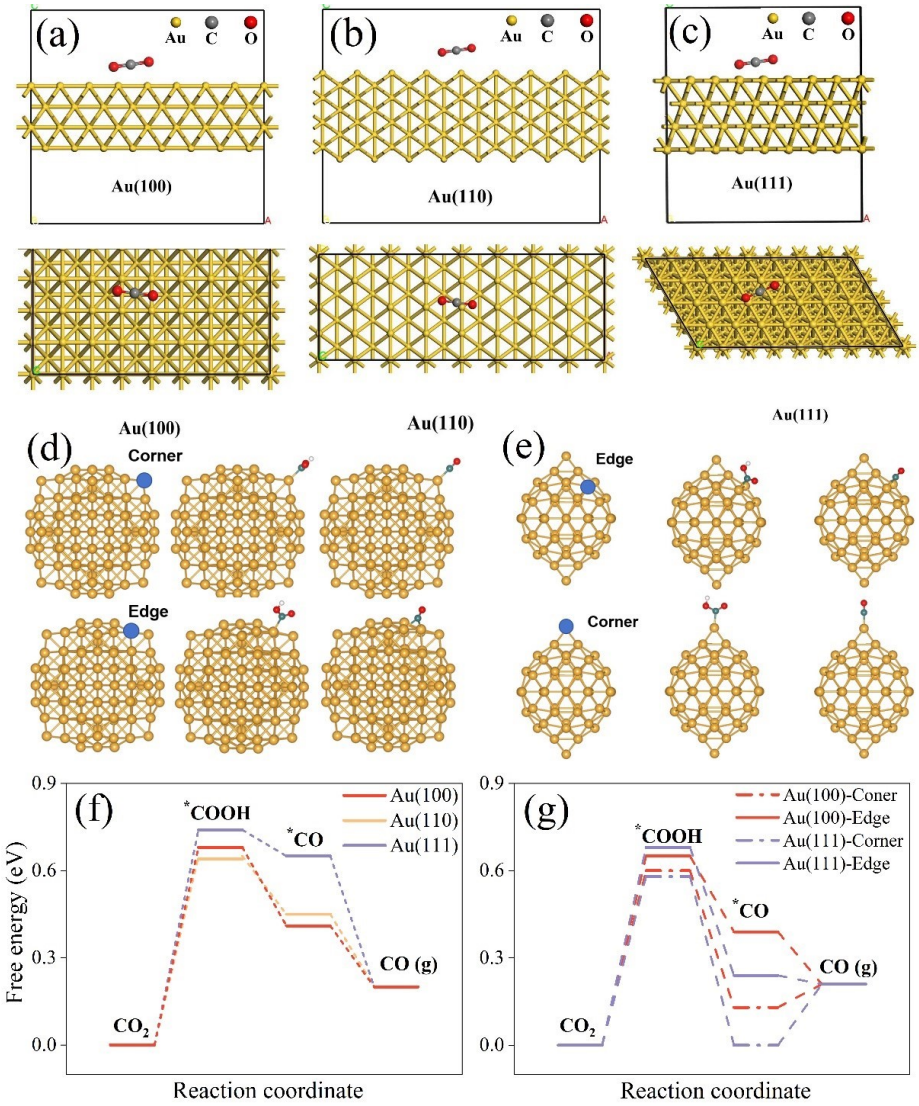

Figure 4.14: Model of DFT calculation. Side views (top half) and top views (bottom half) of 4 × 2 periodic surface slab including four atomic layers of (a) Au(100) (b) Au (110) (c) Au (111). Au cluster model for edge and corner free energy calculation with exposed facets as (d) Au (100), (e) Au (111). (f) Calculated free energy diagrams for the CO_2 reduction process on Au (100), (110) and (111) facets and (g) free energy diagrams for the CO_2 reduction on edges and corners.

To further explore the mechanism of plasmonic catalysis, we examined the influence of light wavelength on catalytic performance. For this purpose, an LED emitting at 405 nm was used, matching the power of the previously tested 525 nm LED (610 mW/cm²). Interestingly, despite the higher energy of 405 nm photons, the improvement in FE(CO) was notably smaller, particularly for Au nanocubes (NCs), as seen in Figure 4.16.

To understand this discrepancy, we calculated energy absorption per atom for each nanoparticle shape as a function of frequency, shown in Figure 4.17. The critical difference emerged at the edges of

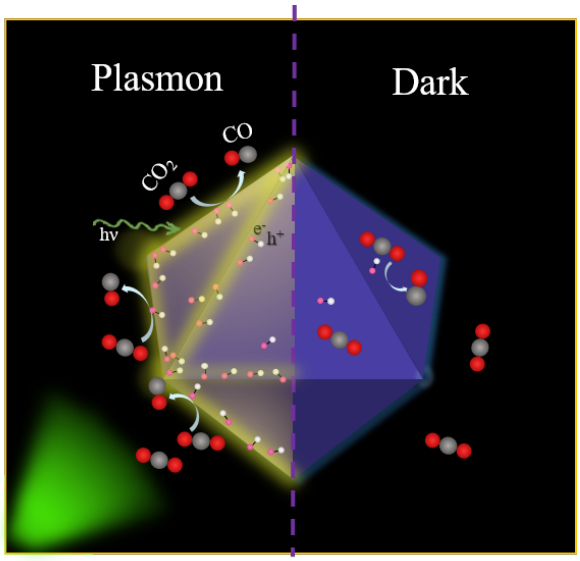

Figure 4.15: Schematic representation of the electrocatalytic CO_2RR response of Au NPs. This diagram illustrates the electrocatalytic CO_2RR response of a Au NP under illumination (plasmon excitation) compared to its activity under dark conditions. While in the dark, the catalytic response is dominated by the exposed crystal facets, upon plasmon excitation the FE(CO) increases substantially, and the role of uncoordinated sites (such as edges and corners) becomes more prominent than the facets.

the nanoparticles, where the absorption changed significantly with varying wavelengths. Notably, for Au NCs, absorption dropped by 70% as the wavelength shifted from 540 nm to 413 nm, resulting in a decrease exceeding 2000 eV/ns. In comparison, Au octahedra (OCs) showed a decrease of 1140 eV/ns, and Au rhombic dodecahedra (RDs) showed only a modest reduction of 180 eV/ns. This significant variation for NCs may be due to the reduced intraband transitions, which decreased from 32% at 563 nm to 10% at 496 nm, as illustrated in Figure 4.12(d-f). Simulations of electric potential enhancement under 405 nm illumination showed that the effect on the facets of NCs was more pronounced. This led to fewer hot electrons being generated and distributed on sites with higher energy barriers, thus activating fewer CO_2 molecules compared to the 525 nm illumination. Consequently, the FE(CO) improvement was significantly smaller under 405 nm light. These findings underscore the importance of hot electron generation and electric field enhancement in our model system.

To further validate our hypothesis regarding the importance of low-coordinated sites (edges) with strong electric field enhancement and hot electron generation, we extended our experiments to the hydrogen evolution reaction (HER). The experimental details are outlined in the Methods section. Under dark conditions, the HER onset potentials for the Au nanoparticles followed the order RD{110} < NC{100} < OC{111}, consistent with the results from DFT simulations (Figure 4.20). Upon illumination, both Au OCs and NCs, which generate large quantities of hot carriers and exhibit significant electric field enhancements, showed substantial reductions in HER onset potential by 0.033 V_{RHE} and 0.021 V_{RHE}, respectively. In contrast, Au RDs exhibited only a slight improvement of 0.007 V_{RHE}, as shown

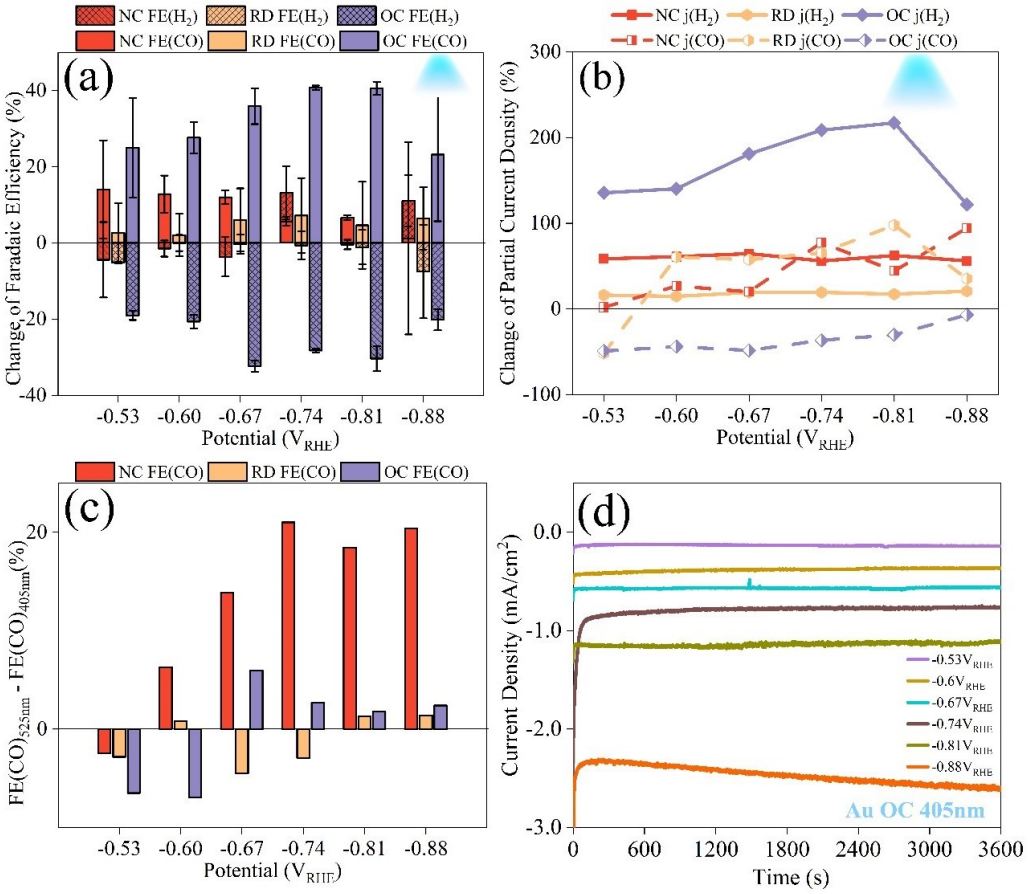

Figure 4.16: CO_2RR performance under 405 nm illumination. (a) Change in the absolute value of FE(CO) and FE(H_2) when illuminated by 405 nm LED compared to dark conditions. The error bars denote the standard deviation obtained from three independent measurements. (b) Percentage change in j(CO) and j(H_2) when illuminated by 405 nm. (c) The difference between FE(CO)525nm and FE(CO)405nm. (d) A typical chronoamperometry measurements under 6 measured potentials used for computing FE and change of current density under 405 nm.

in Figure 4.18(a-c). The corresponding Tafel plots are presented in Figure 4.19, and the consistency of these results was confirmed through three independent rounds of experiments.

The pronounced interaction between plasmonic light and the catalytic activity of Au OCs and NCs, coupled with the minimal response observed in Au RDs during HER, provides further evidence of the importance of abundant hot carriers and electric field enhancement in plasmonic catalysis. The larger reduction in onset potential seen in OCs, which have a higher edge-to-facet ratio, underscores the dominance of low-coordinated sites in plasmonic electrocatalysis.

In summary, in contrast to traditional electrocatalytic systems, facets do not play a prominent role in plasmonic catalysis. Instead, low-coordinated sites like edges, which experience substantial electric field enhancements and high hot electron densities, are more critical. These findings, which diverge from conventional catalytic behavior, illustrate the unique nature of plasmonic catalysis.

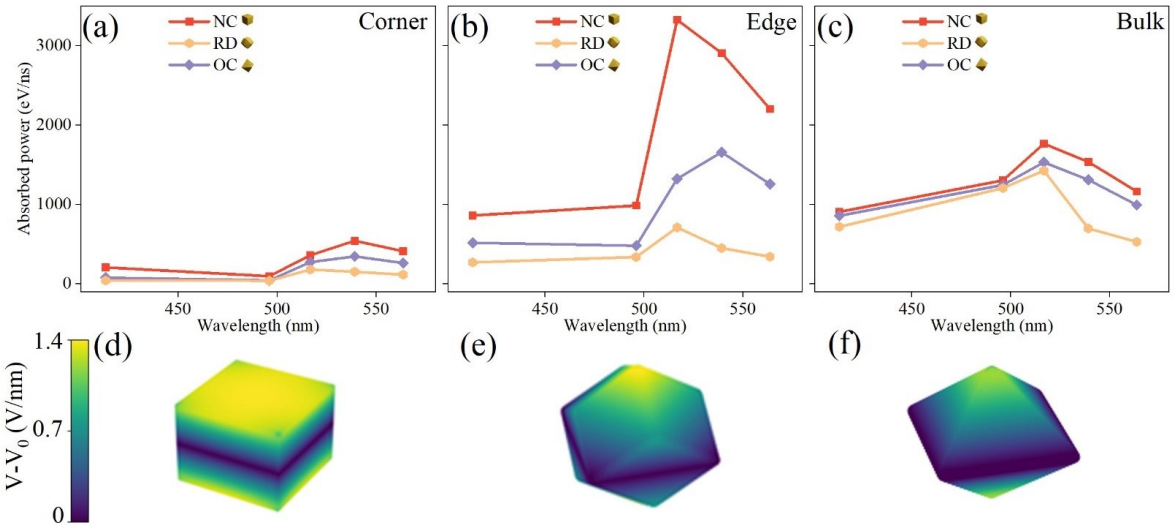

Figure 4.17: Mechanism investigation for the system with 405nm illumination. (a-c) Energy absorption per atom for different region on Au NPs as a function of frequency. (d-f) Electric potential enhancement on Au NPs with 405 nm illumination.

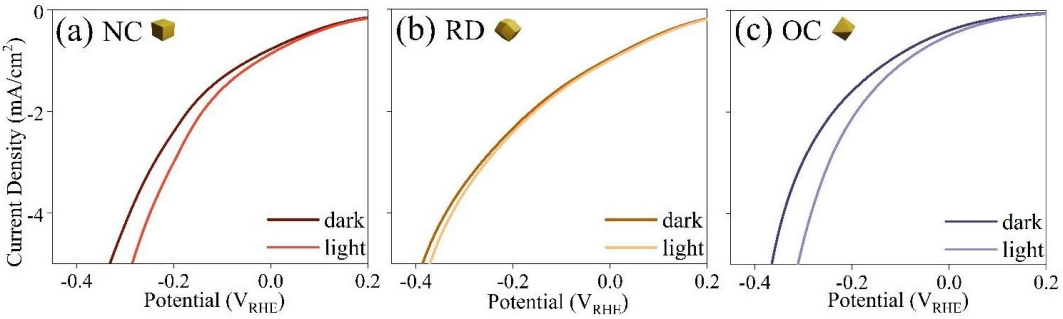

Figure 4.18: HER performance on Au NPs. a-c. Linear sweep voltammetry (LSV) curves of Au NCs (a), RDs (b), and OCs (c) measured in the dark and under 525 nm LED illumination.

4.3 Summary

In our study of plasmon excitation in electrocatalytic CO_2RR and HER systems, we investigated three Au NP morphologies: NCs, RDs and OCs. In the absence of light (pure electrocatalytic CO_2RR), Au RDs displayed the highest selectivity for CO, achieving a FE(CO) of up to 94% at -0.67 V_{RHE}. In contrast, Au NCs and OCs had lower selectivities, with FE(CO) values of 69% and 51%, respectively. These variations were attributed to the distinct formation energies of COOH* intermediates on the specific Au facets exposed by each nanoparticle, underscoring the critical role of facets in conventional (dark) electrocatalysis.

When plasmonic excitation was introduced, however, the trend shifted dramatically. Au OCs, which had the lowest CO selectivity in pure electrocatalytic conditions, exhibited the most significant

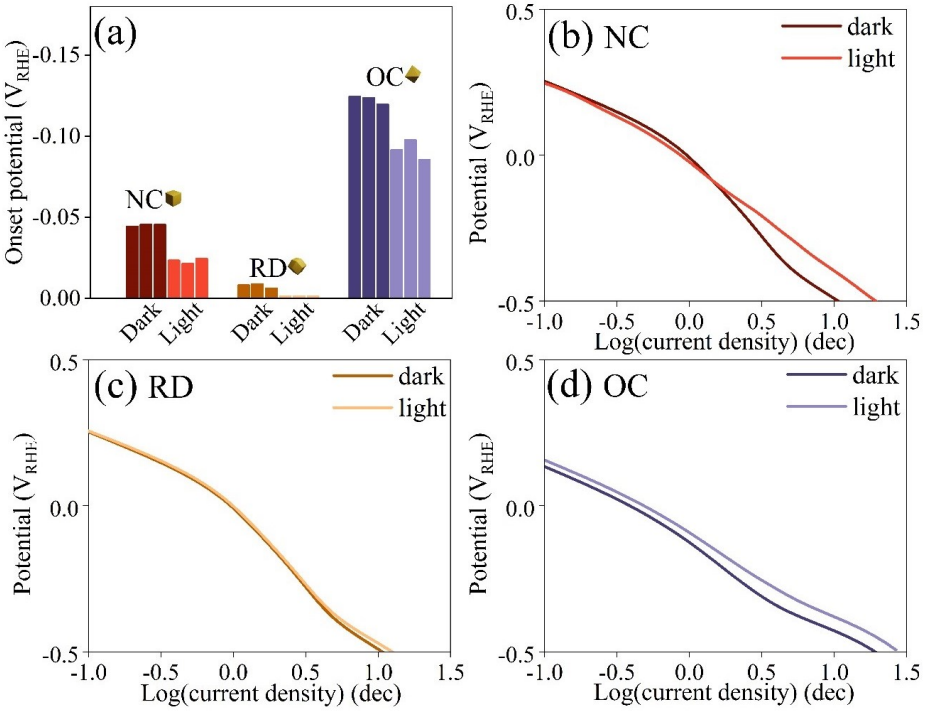

Figure 4.19: HER experiment results. (a) Onset potentials for HER on three Au NPs under dark conditions and 525 nm illumination. (b-d) Tafel plots for (b) Au NCs, (c) RDs and (d) OCs.

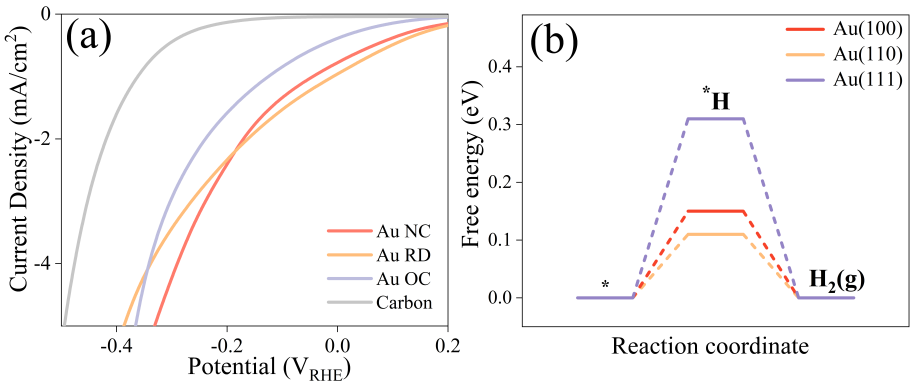

Figure 4.20: HER performance on Au NPs. (a) LSV curves of Au NPs in electrocatalytic system. (b) Calculated free energy diagrams for the HER process on Au {100} {110} and {111} facets.

enhancement under illumination. At -0.81 V_{RHE}, the FE(CO) of Au OCs doubled, rising from 44% to 87%, while Au NCs saw a 26% increase under the same conditions. On the other hand, Au RDs, despite their excellent dark performance, only showed a modest 5% increase in FE(CO) upon illumination. Similar trends were observed in the partial j(CO): Au OCs and NCs experienced remarkable improvements of 210% and 84%, respectively, while Au RDs saw only a slight 16% increase upon plasmon excitation.

These findings highlight the substantial role of plasmon excitation in enhancing catalytic selectivity and activity, with significant differences observed between nanoparticle morphologies.

To further understand these divergent responses, we first examined the influence of temperature on CO_2RR activity. Control experiments demonstrated a decline in FE(CO) as the temperature increased, indicating that the improved performance under plasmon excitation could not be attributed to thermal effects. This points to a distinct plasmonic mechanism, separate from traditional thermal catalysis.

We then shifted our focus to the generation of 'hot carriers' (energetic electrons and holes) as the key drivers behind the enhanced performance under plasmon excitation. Large-scale atomistic simulations and electromagnetic field modeling revealed that Au OCs and NCs generated more hot carriers and exhibited stronger electric field enhancements compared to Au RDs. These results were consistent with the experimental observation of stronger light responses for OCs and NCs, highlighting the critical role of hot carriers and electric field enhancement in plasmonic catalysis. Electromagnetic modeling also showed that low-coordinated sites, such as corners and edges, experienced significantly stronger electric field enhancements, concentrating hot carriers at these sites rather than on facets. This is in agreement with previous studies that demonstrated the catalytic favorability of edges in CO_2RR[184,185].

Based on these findings, we proposed a mechanism for plasmon-enhanced CO_2RR: low-coordinated edge sites concentrate the electric field more intensely, leading to higher hot carrier generation. These hot carriers facilitate the activation of CO_2 molecules at the edges, resulting in enhanced selectivity and activity. In contrast, facets, which dominate dark electrocatalysis, play a less significant role under plasmon excitation. This mechanism is further supported by studies on other plasmonic systems, such as Ag-Cu_2O nanoparticles for pollution degradation, where edge-active sites showed higher catalytic activity than facet-dominated sites[187].

To validate our hypothesis about the greater importance of low-coordinated sites in plasmonic catalysis, we extended our study to the HER. In dark conditions, the HER onset potentials followed the same facet-based trend as CO_2RR, with RDs showing the most favorable onset potential. However, under plasmon excitation, Au OCs and NCs, which generated larger numbers of hot carriers and experienced stronger electric field enhancements at their edges, showed the greatest improvements in HER activity. Au RDs, with fewer hot carriers and weaker plasmonic response, showed only minor improvements. These results further confirmed the significance of hot carrier generation at low-coordinated sites in plasmonic catalysis.

In conclusion, our study demonstrates that the role of facets, which is prominent in dark electrocatalysis, diminishes in plasmonic catalysis. Instead, low-coordinated sites, such as edges, dominate the plasmon-enhanced catalytic processes due to their ability to concentrate electric fields and generate abundant hot carriers. These findings provide valuable insights into the distinct reactivity of plasmonic catalysts and offer a roadmap for designing more efficient light-activated catalysts in the future.

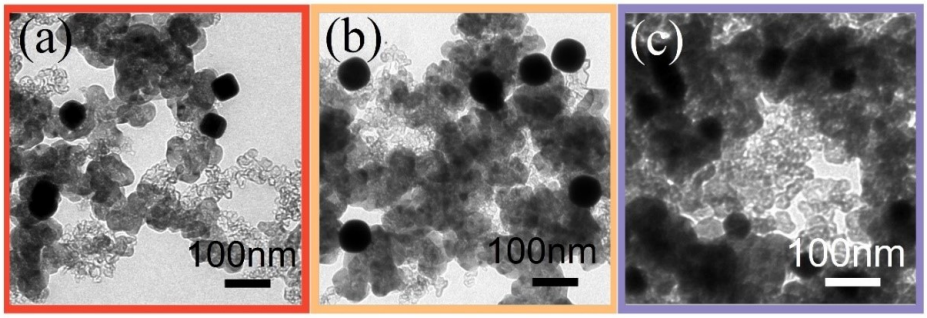

Figure 4.21: Au/C composites. TEM images of Au/C composites of (a) Au NCs, (b) Au RDs and (c) Au OCs.

4.4 Methods

Characterization of Au NPs.
For characterization of the synthesized nanostructures, transmission electron microscopy (TEM) and high-resolution transmission electron microscopy (HRTEM) were performed using a JEM1011 microscope operated at 80 kV and a JEM-2100F microscope operated at 200 kV, respectively. Scanning electron microscopy (SEM) measurements were carried out using a Zeiss Ultra Plus scanning electron microscope with a beam intensity of 10 kV. UV–vis–NIR absorption spectra of the samples were recorded using a Perkin Elmer Lambda 750 UV/VIS/NR spectrometer. X-ray diffraction (XRD) measurements were conducted using a custom-built molybdenum Kα X-ray reflectometer/diffractometer. The measurements were taken at a fixed incidence angle of 10°, with intensities recorded at different scattering angles (2ϑ) ranging from 10° to 60°, using 2500 steps (0.02°/step) with a 10-second acquisition time per step, utilizing a NaI scintillation point detector. Additionally, elemental analysis (EA) for carbon (C), hydrogen (H), and nitrogen (N) content was performed using the Heraeus Elementar Vario EL instrument. This comprehensive characterization provided insights into the morphology, crystallographic structure, and optical properties of the synthesized Au nanostructures.

CO_2RR (Plasmonic) Electrocatalytic Experiments.
1. Preparation of working electrodes.

For electrode preparation, the Au/C composite was firstly prepared. Au nanoparticles (Au NPs) were mixed with carbon powder to achieve an Au mass loading of 20 wt%, which was selected to prevent aggregation of the Au NPs. The mass ratio of Au to carbon was verified through elemental analysis (EA) of carbon (C), hydrogen (H), and nitrogen (N), as shown in Table 4.3. Subsequently, 5 mg of the Au/C composite was dispersed in a solution containing 0.5 mL of 2-propanol, 0.5 mL of water, and 10 µL of Nafion to create a homogeneous ink. Transmission electron microscopy (TEM) was employed to examine the Au/C composites, confirming that the Au NPs were uniformly distributed throughout the porous carbon matrix, as depicted in Figure 4.21.

Table 4.3: Elemental analysis (C, H, N) test result of Au/C composites.

Au NP sample	Initial Weight (mg)	N (%)	C (%)	H (%)	S (%)
Au NCs	2.044	0	81.04	0	0
	2.298	0	81.04	0	0
Au RDs	2.210	0	80.75	0	0
	2.589	0	80.74	0	0
Au OCs	2.078	0	80.67	0	0
	2.587	0	80.64	0	0

For electrode preparation, carbon paper was cut into strips measuring 0.5 cm × 2 cm. A 40 μL aliquot of the ink was then applied to a 0.5 cm × 1 cm area on the carbon paper, forming the working electrode. The final mass loading of the Au/C composite on each electrode was calculated to be 200 μg, with approximately 40 μg of Au NPs. In the control experiments utilizing pure carbon, the mass loading of the carbon powder was maintained at 200 μg per electrode to ensure consistent conditions for comparative analysis.

2. CO_2RR (plasmon-assisted) electrocatalysis measurement.

The CO_2RR measurements were conducted in a custom-designed H-type cell, connected to a potentiostat and an online gas chromatograph (GC) system (Clarus 590 GC, Perkin Elmer) equipped with flame ionization detector (FID) and thermal conductivity detector (TCD), as detailed in Scheme 4.22. The working electrode was prepared by loading carbon paper with the Au/C composite, as previously described. A platinum mesh served as the counter electrode, while an Ag/AgCl electrode was employed as the reference electrode. The electrolyte solution used was 0.1 M NaHCO3, which was continuously purged with CO_2 (99.998% purity, Linde) at a flow rate of 30 standard cubic centimeters per minute (sccm), controlled via a flow meter (PR4000B, MKS). Given that the gas flow rate post-GC was observed to be slightly lower than the inlet flow rate, the Faradaic Efficiency (FE) values reported in this study were normalized by dividing by a correction factor of 0.9 to account for gas losses.

Prior to the experiments, the electrolyte was fully saturated with CO_2 by bubbling the gas for at least 1 hour. During the CO_2RR measurements, gas-phase products were sampled and injected into the GC every 30 minutes, while liquid-phase products were detected using proton nuclear magnetic resonance spectroscopy (^{1}H NMR) after the reaction was completed. Additionally, the electrochemically active surface area (ECSA) of the working electrodes was measured before the CO_2RR experiments. The method used to determine ECSA, as well as the resulting values, are provided in Method Section, Figure 4.23, and Table 4.4. The current densities reported in this study were normalized by dividing the total current by the corresponding ECSA to ensure consistency.

For the photo-electrocatalytic measurements, high-power light-emitting diodes (LEDs) with wavelengths of 525 nm and 405 nm (Mightex Systems) were used as the illumination sources. These LEDs were focused through a lens and positioned approximately 5 cm from the front of the reactor. The power density at the reactor's front surface was measured to be 610 mW/cm² using a power meter.

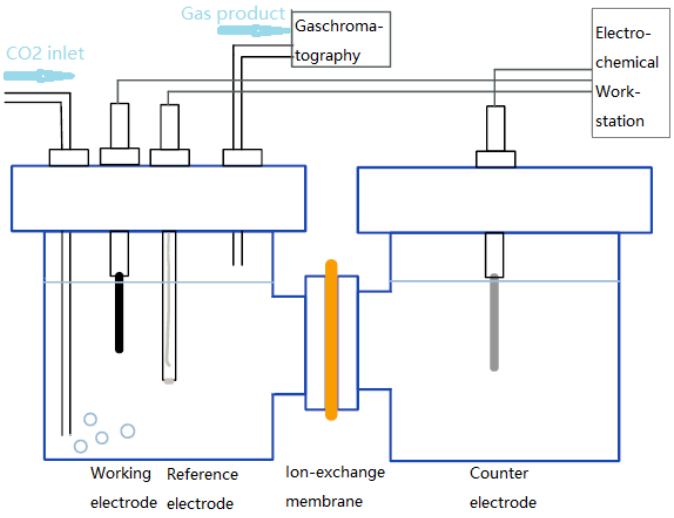

Figure 4.22: Scheme of the setup for CO_2RR measurement.

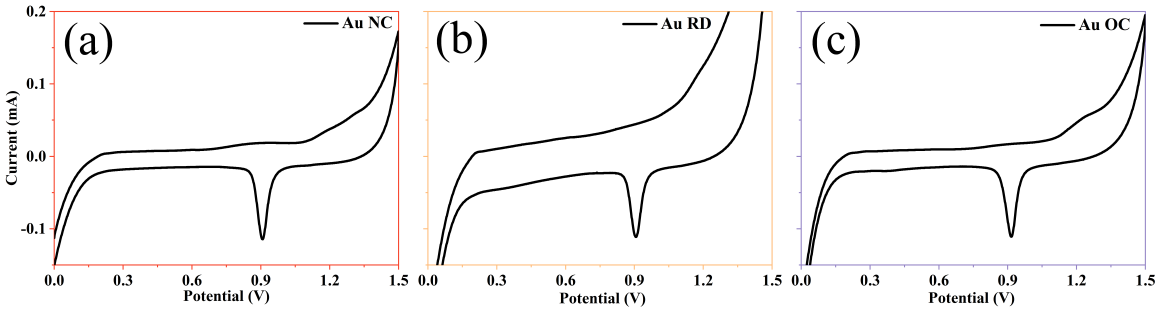

Figure 4.23: CV curves on (a) Au NCs, (b) Au RDs and (c) Au OCs in the non-Faradaic regions of 0 to 1.5V with a scan rate of 10 mV/s in the electrolyte of 0.1 M HClO4 solution. The peak areas of CV curves were integrated and then divided by the scan rate and conversion factor of 450 µC/cm2 to get the ECSA of electrodes. The specific ECSA of electrodes are shown in Table 4.4.

Table 4.4: Electrochemically active surface area (ECSA) of working electrodes.

Au NPs on electrodes	NC	RD	OC
ECSA (cm^2)	1.28	1.11	1.28

All experiments, except for those assessing temperature dependence, were carried out at a controlled room temperature of 23°C.

3. Detailed measurement parameter setting.

3.1 Gas Chromatography.

The gas chromatography (GC) system used in this study was an Arnel Engineered Solutions Clarus 590 GC (Perkin Elmer) connected to a Hydrogen generator (NM Plus, Perkin Elmer) for the online measurement of gaseous products from the reactor cells. Argon (Ar) was employed as the carrier gas at a flow rate of 27.0 mL/min. The injector temperature was maintained at 400°C. The GC was equipped with two detectors: a thermal conductivity detector (TCD) and a flame ionization detector (FID). The operational parameters for the TCD were set with a detector temperature of 200°C. For the FID, hydrogen and air were supplied at flow rates of 45.0 mL/min and 450.0 mL/min, respectively, with a detector temperature of 250°C.

The temperature programming of the GC column began with an initial hold at 70°C for 5 minutes. Following this, the temperature was increased to 150°C at a rate of 20°C per minute and held constant at this temperature for 17 minutes. These settings enabled precise separation and detection of the gas-phase products generated during the catalytic experiments.

3.2 ^{1}H NMR.

To analyze the liquid products from CO_2 reduction reactions (CO_2RR), a mixture of 0.9 mL of post-reaction electrolyte, 0.1 mL of deuterium oxide (D_2O), and 1 µL of dimethyl sulfoxide (DMSO) was prepared. This solution was thoroughly mixed and subsequently injected into an NMR tube for measurement using proton nuclear magnetic resonance spectroscopy (^{1}H NMR). The ^{1}H NMR spectra were recorded on Avance III HD 500 MHz Bruker BioSpin spectrometers to detect the liquid-phase products formed during the reaction.

3.3 Potentiostat.

For electrochemical measurements, a potentiostat was used to perform several key experiments, including cyclic voltammetry (CV), open-circuit potential (OCPT) measurement, electrochemical impedance spectroscopy (EIS), linear sweep voltammetry (LSV), and current-time (i-t) curves. During CV, the potential was swept from -0.6 V to -2.0 V over 20 segments, with a sample interval of 10 mV. The LSV was conducted with the same initial, final, and interval potentials as CV to provide complementary insights into the reaction kinetics. EIS was used to assess the solution resistance for iR drop compensation, with measurements taken at the open-circuit potential (OCP) obtained from OCPT experiments. The frequency in EIS ranged from 10^5 Hz to 1 Hz. Current-time (i-t) measurements were conducted for a duration of 3600 seconds to study the stability and behavior of the system over time. All potentials measured during these experiments were carefully calibrated and converted to values relative to the reversible hydrogen electrode (RHE).

Electrochemically Active Surface Area Measurement.

The electrochemically active surface area (ECSA) of the electrodes was treated as the effective surface area involved in the electrochemical processes, providing a more accurate measure of catalytic activity than the geometric area alone. In this study, ECSA was determined by cyclic voltammetry (CV) in non-Faradaic regions[188], where adsorption and desorption processes occur without charge-transfer reactions, as illustrated in Figure 4.23. The CV measurements were performed by sweeping the potential between 0 and +1.5 V at a scan rate of 10 mV/s in an electrolyte solution of 0.1 M $HClO_4$.

To calculate the ECSA, the peak areas from the CV curves were integrated, and the total charge was normalized by dividing by the scan rate. A conversion factor of 450 $\mu C/cm^2$ was applied to convert the integrated charge to an estimate of the ECSA, based on established methods in the literature[189]. The specific ECSA values for each electrode, representing the surface area per unit of catalyst, are summarized in Table 4.4. This method provides a critical parameter for comparing the catalytic performance of different electrode materials under electrochemical conditions.

DFT Calculation.
To investigate the mechanisms underlying the reduction of CO_2 to CO on different gold (Au) facets, we constructed periodic surface slabs of Au with dimensions of 4 × 2 for the (100), (110), and (111) orientations, each containing four atomic layers, as depicted in Figure 4.14 (a-c). A vacuum slab of 30 Å was incorporated to mitigate any interactions arising from periodic boundary conditions. Each of these models consists of a total of 128 atoms. Additionally, to analyze the reactivity of edge and tip sites in CO_2 reduction reactions (CO_2RR), we developed two models of Au nanoclusters, specifically featuring Au {100} and Au {111} as the primary exposed facets, as illustrated in Figure 4.14 (d-e). These Au nanocluster models comprise 147 and 85 Au atoms, respectively.

The density functional theory (DFT) calculations were conducted using the Vienna Ab initio Simulation Package (VASP), employing the projector augmented wave (PAW) method[190,191]. The exchange and correlation potentials were described using the generalized gradient approximation with the Perdew-Burke-Ernzerhof (GGA-PBE) functional[192,193]. For Brillouin zone integration, a k-point mesh of 1 × 2 × 1 was employed. The cutoff energy was set at 450 eV, with convergence criteria established for energy and force at 1×10^{-5} eV/atom and 0.02 eV/Å, respectively.

The proposed mechanism for the CO_2 reduction to CO is as follows:

$$CO_2 + * + H^+ + e^- \rightarrow *COOH$$
$$*COOH + H^+ + e^- \rightarrow *CO + H_2O$$
$$*CO \rightarrow CO + *$$

The asterisk (*) of above means the substrate. The change of Gibbs free energy (ΔG) for each reaction step is given as follow[194]:

$$\mathbf{\Delta G = \Delta E + \Delta ZPE - T\Delta s} \tag{4.1}$$

where ΔE represents the total energy difference between the product and the reactant. ΔZPE and TΔS are the zero-point energy correction and the entropy change at 298.15 K, respectively.

HER (Plasmonic) Electrocatalytic Experiments.

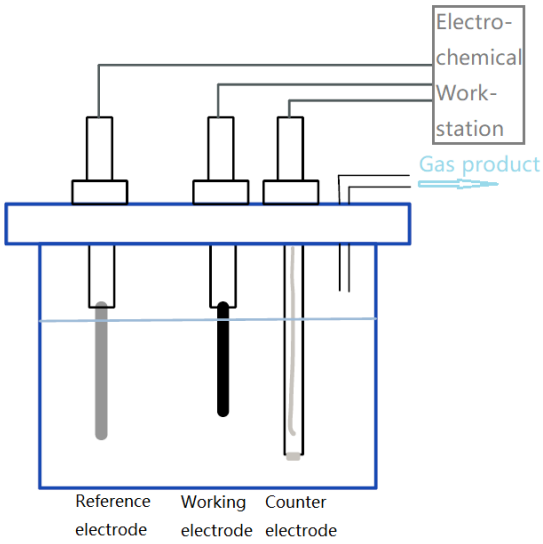

Figure 4.24: Scheme of the setup for HER measurement.

The hydrogen evolution reaction (HER) measurements were performed using a conventional three-electrode cell, as depicted in Scheme 4.24. The working electrodes used were the same as those for the CO_2 reduction reaction (CO_2RR). The electrolyte employed was a 0.1 M $HClO_4$ solution, which was thoroughly purged with nitrogen (N_2) for 30 minutes prior to the experiment to eliminate dissolved oxygen (O_2). The current density was calculated by normalizing the total current to the electrochemically active surface area (ECSA) of the electrodes.

In the HER system, the electrochemical measurements were conducted using an electrochemical workstation with parameters similar to those used in the CO_2RR experiments, but with minor adjustments. Cyclic voltammetry (CV) measurements were performed over 20 segments, sweeping the potential from 0 V to -1.0 V, with a potential interval of 10 mV between steps. Linear sweep voltammetry (LSV) followed the same potential range and intervals as CV. The electrochemical impedance spectroscopy (EIS) settings were identical to those used in the CO_2RR measurements. All measured potentials were calibrated and converted to the reversible hydrogen electrode (RHE) scale for consistency and comparison.

In the photo-electrocatalytic HER system, the illumination source used was the same as that employed in the CO_2RR experiments, consisting of high-power LEDs with specific wavelengths. This setup was utilized to examine the effect of light on HER activity, enabling a direct comparison between the two reactions under similar experimental conditions.

5

Plasmon-boosted Directional Transfer of Photo-generated Electrons

The content of this chapter is based on our manuscript to be submitted (Kang, Y., Tan, Y., Tian, W., Zhang, H., Wang, J., Kammerer, D., Akkerman, Q., Fan, C., Zhu, L., Fu, J., Liu, M., and Cortés, E. Plasmon-boosted Directional Transfer of Photo-generated Electrons for Improved H_2O_2 Production in Au@TiO_2 Hybrid Systems). As the foundation of the chapter, the current version of manuscript is used. Large language models are used to refine the grammars.

5.1 Research background

Hydrogen peroxide (H_2O_2) has become a crucial component in numerous fields, as an environmentally friendly oxidant and a potential sustainable energy carrier. Its applications span chemical manufacturing, environmental remediation, and fuel cell technologies[195–198]. However, traditional production methods of H_2O_2 based on anthraquione or mixtures of H_2 and O_2, which is toxic and dangerous. Recently, photocatalytic synthesis of H_2O_2 has attracted more attention, as it offers a cleaner, safer alternative[199], for which, oxygen reduction (ORR) and water oxidation (WOR) reactions are the two main pathways. Utilizing only water and oxygen, photocatalytic approaches harness solar energy for chemical conversion without generating harmful byproducts, minimizing explosion risks and reducing energy demands[196,199].

Over recent decades, the development of diverse photocatalysts for H_2O_2 production has demonstrated promising results, including carbon nitride[200–203], TiO_2[204–211], metal-organic-compound-based materials[212–214], etc. Among all the materials, TiO_2-based catalysts have demonstrated superior performance. TiO_2 has been always an interesting material for catalysis - its chemical stability, wide availability, and high catalytic efficiency make it to be well-suited for large-scale applications. Despite

these advantages, TiO_2 is primarily responsive to UV light, which constitutes only a small fraction of the solar spectrum. Additionally, challenges such as rapid electron-hole recombination and limited charge transport also hinder its overall light-to-chemical efficiency[215]. To address these limitations, strategies including nanostructure engineering[204], surface modifications[208], and heterostructure designs[211,216] have been explored. Notably, combining TiO_2 with plasmonic nanoparticles to form hybrid nanostructures has emerged as an effective approach. Such hybrids extend light absorption, facilitate charge separation via Schottky barriers and eventually improve catalytic performance. For certain cocatalysts, the interface between TiO_2 also show remarkable catalytic activity, further boosting H_2O_2 production efficiency. Most importantly, the activation of surface plasmons plays a pivotal role in modulating charge carrier transfer, offering significant potential for further enhancements[217].

Surface plasmons describe the collective oscillations of free electrons within a material when exposed to specific wavelengths of light. In nanoparticles smaller than the wavelength of light, these oscillations become confined, resulting in localized surface plasmon resonance (LSPR). LSPR is associated with several key effects, including the enhancement of the electric field near the surface of the particles, the generation of high-energy charge carriers (hot carriers), and localized thermal effects. These unique properties of LSPR have been shown to significantly aid catalytic processes[218,219]. For instance, enhanced electric fields generated by LSPR have been demonstrated to play a critical role in driving various chemical reactions. Examples include the hydrogen evolution reaction (HER)[220], carbon dioxide reduction reaction (CO_2RR)[221–224], nitrogen reduction reaction (NRR)[225] as well as oxygen reduction reaction (ORR)[226,227]. Theoretical studies further highlight the significance of electric fields in activating chemical bonds, such as those in oxygen molecules (O_2)[228–230]. Beyond the role of electric fields, hot carriers generated by plasmon resonance contribute to catalytic enhancement by accelerating reaction kinetics[115,231–233]. Our prior research on plasmonic electrocatalysis demonstrated that hot electrons concentrated at nanoparticle edges greatly improve both the activation and selectivity of CO_2 molecules[115]. In hybrid nanostructures, efficient energy transfer across interfaces has also been recognized as crucial for optimizing quantum efficiency and catalytic performance[217,234,235]. This study seeks to bridge existing gaps by exploring the influence of LSPR on directional electron transfer in hybrid nanostructures and examining the underlying mechanisms that drive catalytic performance enhancements.

Au@TiO_2 core-shell nanostructures provide an excellent platform to investigate these effects. These hybrids combine the strong catalytic performance of TiO_2 for oxygen reduction with the enhanced efficiency imparted by plasmonic Au[211]. The energy alignment between Au and TiO_2 forms a Z-scheme configuration, which improves charge separation and extends the lifetime of charge carriers. The core-shell architecture further maximizes the interfacial area, facilitating charge transfer and molecular interactions while improving structural stability[215]. Additionally, the porous TiO_2 shell enhances UV light scattering, leading to increased light absorption and a higher rate of electron-hole pair generation[211,236]. These features collectively make Au@TiO_2 nanostructures a powerful system for advancing plasmon-assisted catalysis.

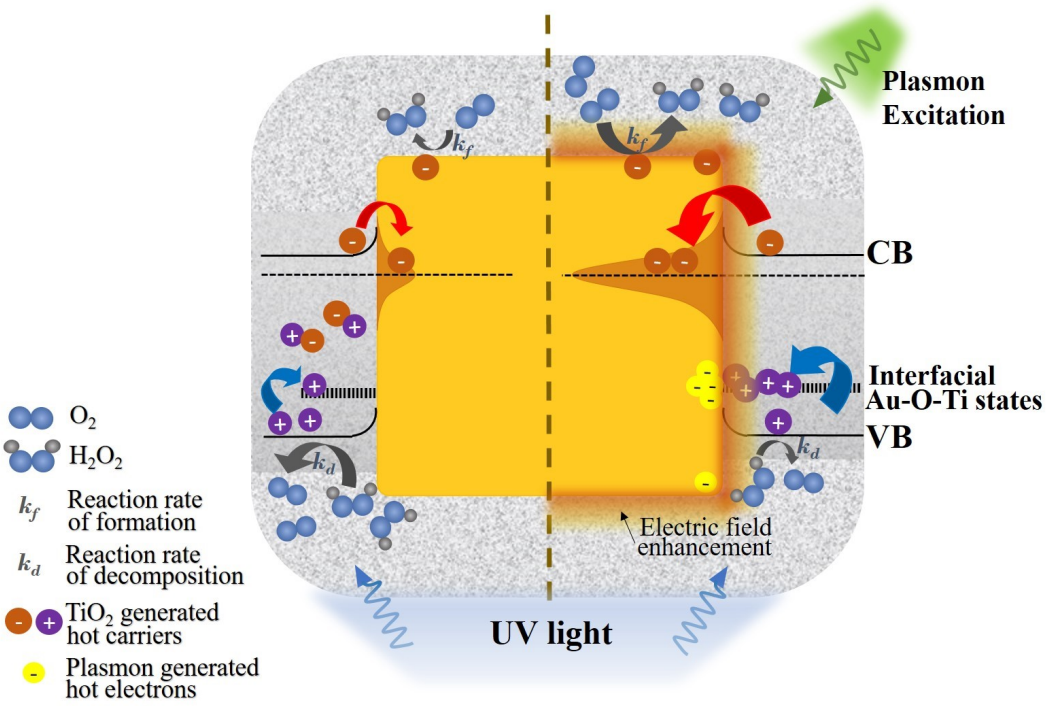

Figure 5.1: Schematic illustration of Au@TiO_2 hybrid nanosystem. Left: Under UV illumination alone, electrons in the TiO_2 shell are excited to the conduction band and subsequently transferred to the Au core, where they activate adsorbed O_2 molecules, facilitating H_2O_2 production. Meanwhile, holes tend to migrate to the interfacial Au–O–Ti states. **Right:** With additional LSPR excitation in the Au core, hot electrons are generated, enabling recombination with holes in TiO_2 and further promoting directional electron transfer from TiO_2 to Au. Simultaneously, LSPR-induced electric field enhancement amplifies this transfer process, collectively leading to a substantial increase in H_2O_2 production.

In this study, Au@TiO_2 core-shell nanostructures were synthesized, incorporating two distinct Au core morphologies: nanocubes (NC) and rhombic dodecahedra (RD). A schematic representation of the core-shell structure is shown in Figure 5.1. Both NC@TiO_2 and RD@TiO_2 demonstrated significant enhancements in photocatalytic H_2O_2 production via O_2 reduction. Notably, the catalytic performance of these core-shell nanostructures surpassed that of individual Au or TiO_2 components by more than fivefold under full-spectrum illumination. To evaluate the role of LSPR in these improvements, photocatalytic H_2O_2 production was investigated under both UV light alone and a combination of UV and 525 nm illumination. The results revealed a significant contribution of LSPR to the enhanced activity. For NC@TiO_2, the combination of UV and 525 nm light led to over a 50% increase in H_2O_2 yield compared to UV illumination alone. This improvement was accompanied by a 73% increase in the ratio of the formation constant to the decomposition constant (k_F/k_D). Similarly, RD@TiO_2 showed an 18% improvement in H_2O_2 yield and a 23% enhancement in the k_F/k_D ratio under the same conditions. Experimental results, supported by theoretical analyses, identified the underlying mechanism responsible for this enhanced catalytic performance. The plasmon-induced generation

of hot carriers and the amplified electric field facilitated electron transfer from TiO_2 to Au. This directional transfer effectively lowered the activation energy barrier for O_2 reduction, accelerating the overall H_2O_2 production process. These findings emphasize the transformative role of plasmonic effects in modifying charge carrier dynamics. They provide valuable insights for the rational design of efficient catalysts for H_2O_2 production. Furthermore, this study highlights the broader potential of plasmonic nanostructures in applications such as pollutant degradation and hydrogen energy storage, offering advancements in sustainable energy technologies.

5.2 Results and dicussion

Synthesis and characterization

Au@TiO_2 core-shell nanocrystals were prepared using two types of Au cores: nanocubes (NCs) and rhombic dodecahedra (RDs). The Au cores, with similar sizes, were synthesized using seed-mediated growth methods based on our previous work[115]. The TiO_2 shells were composed of aggregated nanoparticles with a porous structure. These shells enhance the adsorption of reactant molecules onto the Au cores. The shells were synthesized by reducing $TiCl_3$ and annealed following the methodology described by Li et al[116]. Further experimental details are provided in the Method section.

Transmission electron microscopy (TEM) and scanning electron microscopy (SEM) images revealed the monodispersed shapes of the NC@TiO_2 and RD@TiO_2 nanocrystals. These are shown in Figure 5.2(a, d) and Figure 5.3. The porous nature of the TiO_2 shells was confirmed by dissolving the Au cores with aqua regia, leaving behind the TiO_2 shells, as shown in Figure 5.4. Energy-dispersive X-ray spectroscopy (EDS) mapping further analyzed the structure and composition. Figure 5.1(b, e) highlights that the core is primarily Au with cubic and rhombic dodecahedral shapes, while the shell consists mainly of Ti and O. This confirms the successful formation of NC@TiO_2 and RD@TiO_2 nanostructures.

X-ray diffraction (XRD) spectra provided additional evidence to confirm the formation of anatase TiO_2 shells and the single face-centered cubic (FCC) phase of the Au cores, as shown in Figure 5.2(g). High-resolution TEM (HRTEM) further examined the surface structure. Figure 5.2(c, f) displays d-spacing values of 0.199 nm and 0.235 nm for Au cores, corresponding to Au (100) and (111) facets in the FCC phase (see Appendix A.1 for the specific values). The porous TiO_2 shells showed d-spacing values of 0.304 nm and 0.190 nm, consistent with anatase TiO_2 (101) and (200) (Appendix A.1).

UV–vis–NIR absorption spectroscopy was used to study the optical properties of the Au@TiO_2 nanocrystals. As shown in Figure 5.2(h), absorption peaks appeared at about 540 nm (Au nanoparticle LSPR) and <300 nm (anatase TiO_2 absorbance) for both core-shell structures. These results confirm the successful combination of Au cores and anatase TiO_2 shells.

X-ray photoelectron spectroscopy (XPS) was conducted to study the interfacial interaction between Au and TiO_2. The XPS survey spectra of NC@TiO_2 and RD@TiO_2 confirmed the presence of C, Au, Ti,

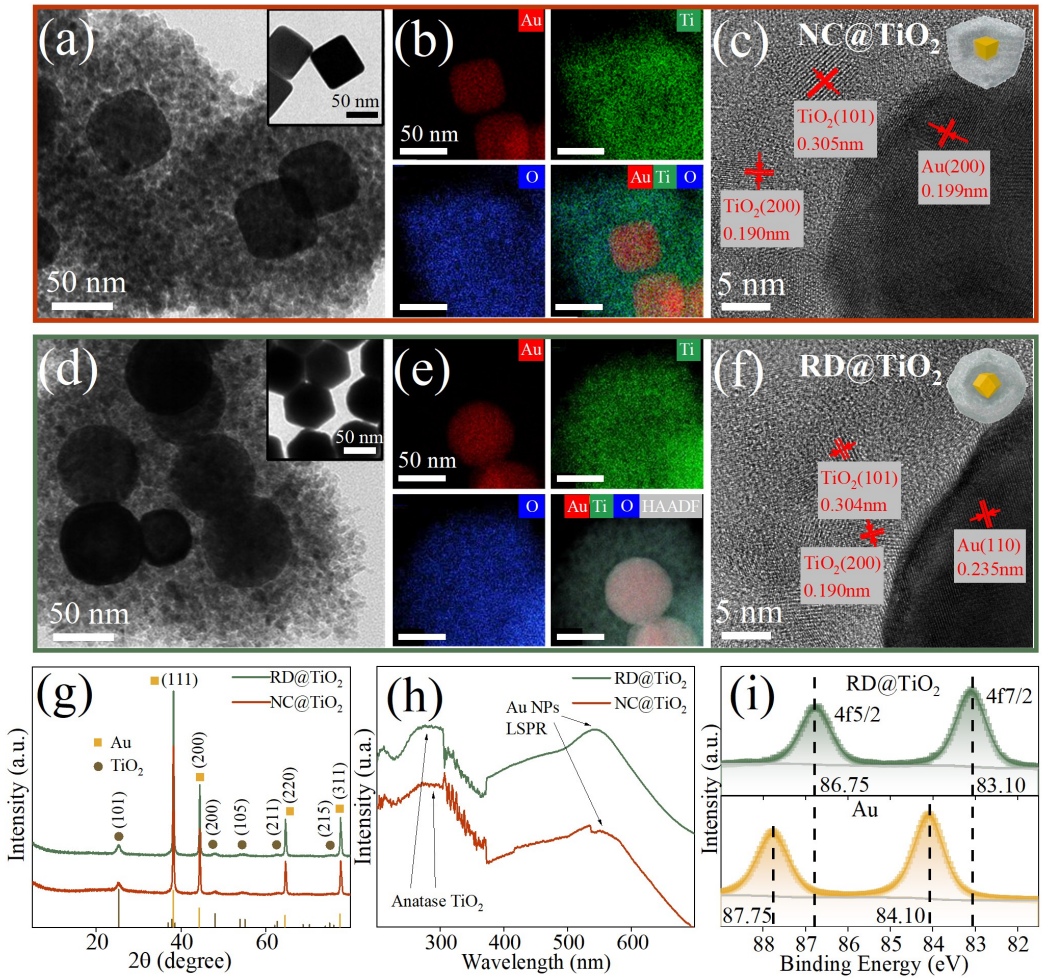

Figure 5.2: Characterization of Au nanoparticles.(a, d) TEM images of (a) NC@TiO_2, (d) RD@TiO_2 and their corresponding Au cores (inset).**(b, e)** EDS map of Au, Ti and O for (b) NC@TiO_2 and (e) RD@TiO_2. **(c, f)** HRTEM patterns of (c) NC@TiO_2 and (f) RD@TiO_2. The average distances between fringes and the corresponding facets are marked in red. (g) XRD patterns of NC@TiO_2 and RD@TiO_2 with the expected XRD pattern of Au in the FCC phase and TiO_2 in anatase phase for Cu Kα radiation. **(h)** UV-visible extinction spectra of NC@TiO_2 and RD@TiO_2 with LSPR absorption at 537 nm and 543 nm, respectively, as well as the TiO_2 absorption of < 300 nm. **(i)** High-resolution XPS spectra of Au 4f of pure Au and RD@TiO_2.

and O elements (Figure 5.5). The high-resolution Au 4f spectrum of RD@TiO_2 (Figure 5.2(i)) showed two peaks at 84.10 eV and 87.75 eV. These peaks correspond to Au $4f_{7/2}$ and $4f_{5/2}$, respectively, and exhibit a negative shift of 1.00 eV compared to pure gold.

The O 1s spectrum (Figure 5.13) was fitted into two peaks at 529.87 eV and 531.71 eV. These peaks are assigned to Ti-O and OH groups, respectively, and display a positive shift of 2.87 eV compared to pure TiO_2 (Figure 5.6)[237–240]. These shifts provide strong evidence of electron transfer from TiO_2 to Au, indicating the formation of a Schottky junction at the Au-TiO_2 interface. The Ti 2p spectrum (Figure 5.13) revealed two peaks at 458.75 eV and 464.35 eV, corresponding to Ti $2p_{3/2}$ and $2p_{1/2}$,

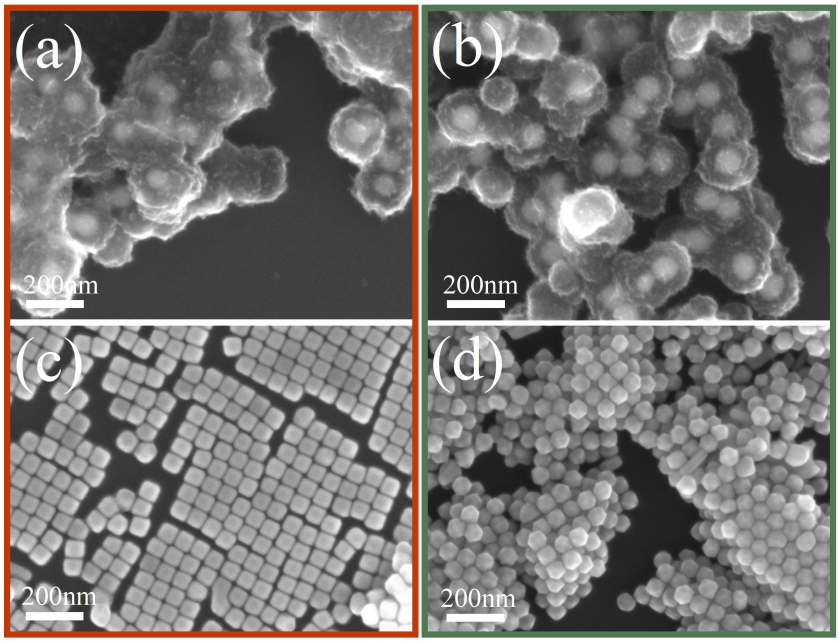

Figure 5.3: SEM images of **(a)** NC@TiO_2 and **(b)** RD@TiO_2 nanostructures and **(c-d)** their corresponding Au cores.

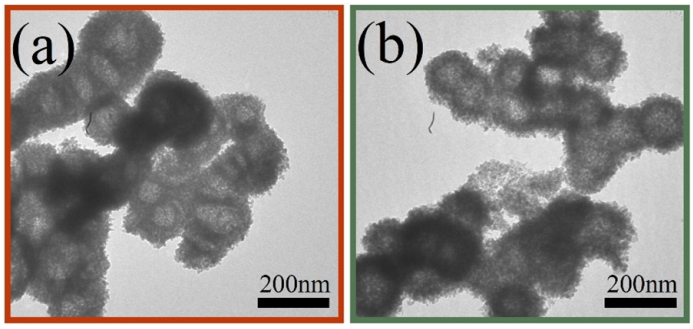

Figure 5.4: TEM images of **(a)** NC@TiO_2 and **(b)** RD@TiO_2 nanostructures after Aqua regia treatment. The holy TiO_2 shells with no Au core prove the porous structure of TiO_2 outside Au.

respectively. These peaks also show a positive shift of 2.75 eV compared to TiO_2. The spectra of NC@TiO_2 exhibited similar peak shifts (Figure 5.14), confirming the same electron transfer direction from TiO_2 to Au.

Based on these findings and previous studies[241], we propose an electron transfer pathway in Au@TiO_2 nanostructures. The conduction band of TiO_2 is at a higher energy level than the Fermi level of Au nanoparticles. As a result, electrons transfer from the conduction band of TiO_2 to Au. This directional electron transfer suppresses electron-hole recombination. Additionally, the formation of the Au–O–Ti interfacial state, located above the TiO_2 valence band, acts as an effective hole trap. This further reduces the recombination energy. Together, these effects enable efficient spatial separation of

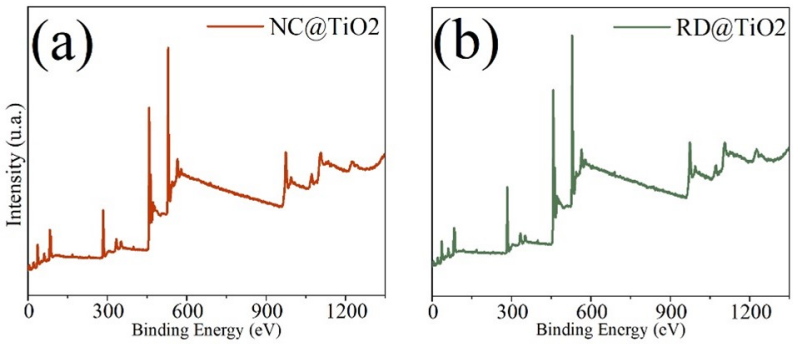

Figure 5.5: XPS survey spectrum of Au@TiO_2 nanostructures.

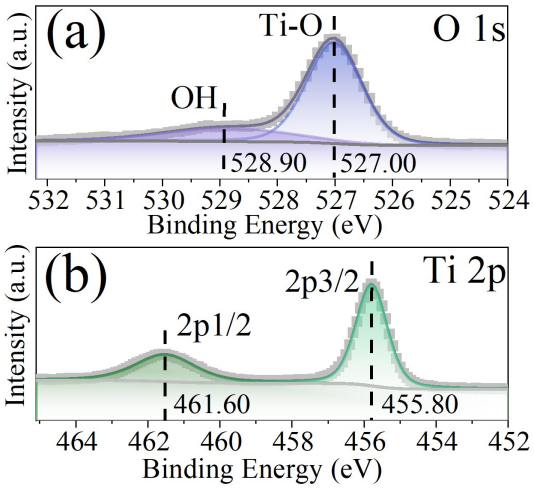

Figure 5.6: XPS specific spectrum of TiO_2 in dark and under 532 nm illumination.

photogenerated charge carriers and extend their lifetime. This mechanism is illustrated on the left side of Figure 5.1.

Photocatalytic H_2O_2 production performance

Photocatalytic H_2O_2 production is gaining attention as a sustainable solution for pollution treatment and hydrogen storage. To evaluate the catalytic performance, photocatalytic tests were performed on NC@TiO_2 and RD@TiO_2 nanostructures. The tests were conducted in deionized water with 10 vol% methanol at pH 3 under Xe lamp illumination (0.4 W/cm^2). Details of the experimental setup are provided in Methods and Figure 5.7.

The H_2O_2 production pathway was confirmed as O_2 reduction. This conclusion was based on the negligible yield of H_2O_2 when the solution was bubbled with N_2 (Figure 5.8).

Comparative analyses were conducted with pure Au and anatase TiO_2, which were synthesized using the same procedures applied to Au@TiO_2. As shown in Figure 5.9(ai), NC@TiO_2 achieved a

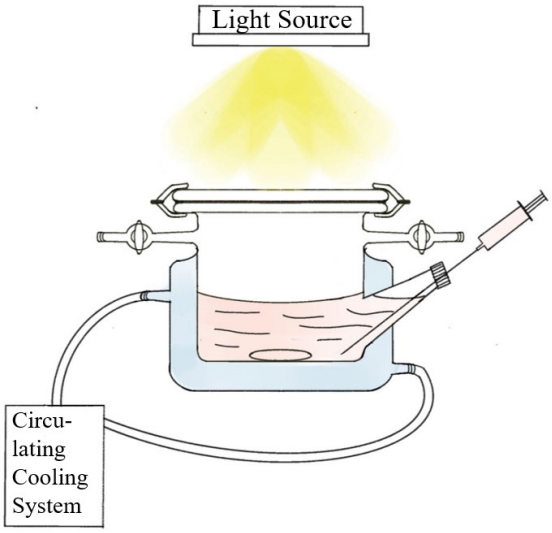

Figure 5.7: Setup scheme of photocatalytic H_2O_2 production measurement.

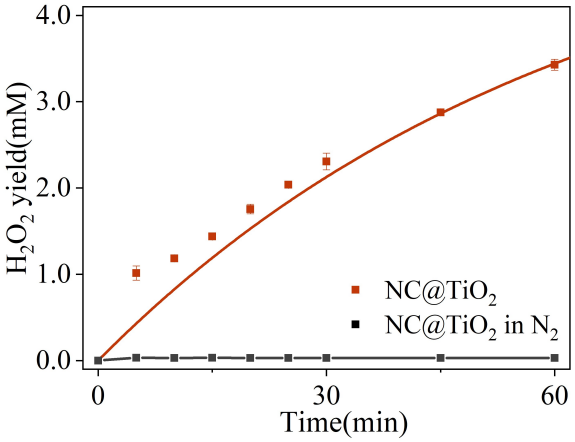

Figure 5.8: Control experiment of H_2O_2 production with N_2 bubbling.

remarkable H_2O_2 concentration of 5.4 mM after 180 minutes. RD@TiO_2 produced 3.7 mM under the same conditions. In contrast, TiO_2 generated only 1.1 mM, and pure gold showed negligible H_2O_2 production. These results highlight the significant role of Au compositing in enhancing the photocatalytic activity on TiO_2.

Further evaluation compared the catalytic activity of Au@TiO_2 with other representative materials. As shown in Figure 5.9(aii) and Table 5.1, NC@TiO_2 demonstrated the highest H_2O_2 generation rate, confirming the superiority of the Au@TiO_2 core-shell nanostructure. Recycling stability tests, illustrated in the inset of Figure 5.9(aii), revealed strong durability. NC@TiO_2 maintained relatively stable H_2O_2 production over five consecutive cycles, showing minimal decline in activity compared to the initial cycle. Notably, the substantial difference in catalytic performance between NC@TiO_2

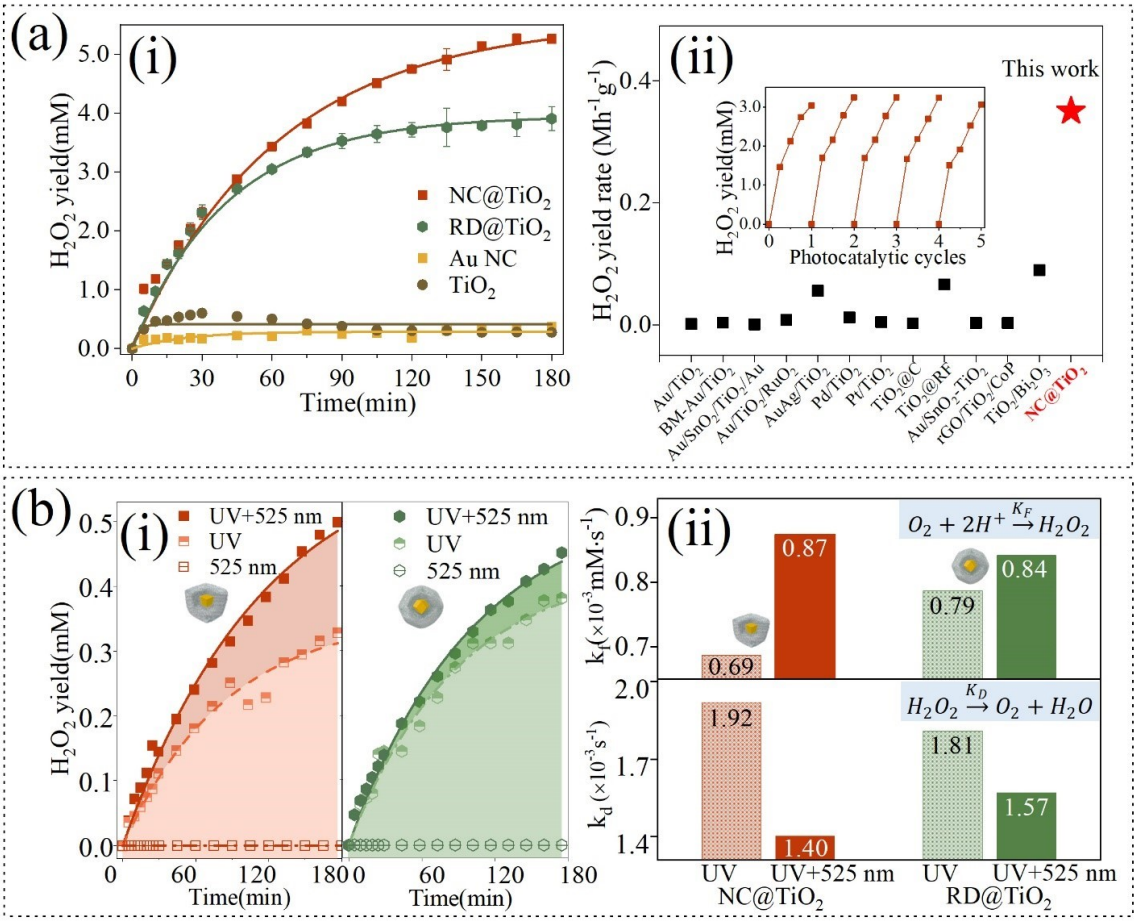

Figure 5.9: Photocatalytic H_2O_2 Production Activities (a) Photocatalytic H_2O_2 production under Xeon lamp illumination. **(i)** Time-dependent H_2O_2 production on NC@TiO_2, RD@TiO_2, pure Au NPs, and anatase TiO_2. The data were collected over three hours. **(ii)** Comparison of production rates with previously reported photocatalysts. The inset shows a stability test for NC@TiO_2 over five cycles, each lasting one hour. **(b)** Photocatalytic H_2O_2 production under UV and 525 nm LED illumination. **(i)** Time-dependent H_2O_2 production on NC@TiO_2 and NC@TiO_2. The tests were performed under UV light alone and UV combined with 525 nm LED illumination. **(ii)** Corresponding reaction rates for H_2O_2 formation (k_F) and decomposition (k_D). Rates are shown for both illumination conditions.

and RD@TiO_2 emphasizes the critical influence of Au core morphology within the heterojunction structure. Previous studies have shown distinct localized surface plasmon resonance (LSPR) behaviors between Au nanocubes and rhombic dodecahedra[115], which play a significant role in modulating their catalytic activity.

Building on these observations, the influence of plasmonic effects on H_2O_2 production was investigated by performing photocatalytic tests under two illumination conditions: UV light alone, and a combination of UV and 525 nm light. UV light activates the TiO_2 shell by exciting electrons into its conduction band, while 525 nm light selectively excites the LSPR of the Au cores. As shown in

Table 5.1: Summary of papers for photocatalytic H_2O_2 production.

Material	H_2O_2 Yield (mM/h·g)	Light Wavelength	Power (Density)	Ref
Au/TiO_2	1.5	> 300 nm	3.0 mW/cm^2 (UV light)	[210]
BM-Au/TiO_2	3.5	420 nm – 485 nm	4.0 mW/cm^2	[208]
$Au/SnO_2/TiO_2/Au$	1	420 nm – 485 nm	4.0 mW/cm^2	[216]
$Au/TiO_2/RuO_2$	8	> 300 nm	30 mW/cm^2	[242]
$AuAg/TiO_2$	56	> 280 nm	13.8 mW/cm^2	[207]
Pd/TiO_2	12	Full spectrum	100 mW/cm^2	[243]
Pt/TiO_2	5.1	> 300 nm	500W (Hg)	[244]
TiO_2@C	2.75	> 320 nm	300W (Xe)	[245]
TiO_2@RF	66.6	Full spectrum	100 mW/cm^2	[206]
Au/SnO_2-TiO_2	3.2	Full spectrum	300W (Xe)	[205]
$rGO/TiO_2/CoP$	3.2	> 320 nm	–	[246]
TiO_2/Bi_2O_3	90	Full spectrum	300W (Xe)	[209]
NC@TiO_2	686	Full spectrum	300W (Xe), 400 mW/cm^2	This work

Figure 5.9(bi), the addition of 525 nm illumination resulted in higher H_2O_2 yields for both NC@TiO_2 and RD@TiO_2 over the three-hour reaction period, confirming the role of LSPR in enhancing catalytic performance. Specifically, the H_2O_2 yield for NC@TiO_2 increased from 329 μM to 500 μM, a 52% improvement, while RD@TiO_2 experienced only an 18% enhancement, from 381 μM to 451 μM.

To further analyze the impact of plasmon excitation, the reaction rates for H_2O_2 formation (k_F) and decomposition (k_D) were calculated by fitting the production-time curves in Figure 5.9(bi) using the equation:

$$\text{Yield} = \frac{k_F}{k_D}\left(1 - e^{-k_D t}\right),$$

where t is the reaction time in seconds. Both NC@TiO_2 and RD@TiO_2 exhibited higher k_F and lower k_D upon LSPR excitation. Notably, the k_F/k_D ratio for NC@TiO_2 increased by 74% (from 3.58×10^3 to 6.23×10^3), whereas RD@TiO_2 showed only a 23% improvement (from 4.36×10^3 to 5.35×10^3). These results demonstrate the significant influence of LSPR on reaction kinetics and its role in enhancing photocatalytic H_2O_2 production. It is worth noting that less than 0.5 μM of H_2O_2 was generated under 525 nm illumination alone, confirming that LSPR assists the process by promoting electron transfer, while the primary electron excitation occurs in TiO_2. In subsequent sections, the mechanism through which LSPR enhances photocatalytic H_2O_2 production will be explored in detail.

Investigation of plasmonic effect in Au@TiO_2 hybrid system Theoretical studies utilizing density functional theory (DFT) calculations highlight the significant impact of electron transfer to the Au in reducing the Gibbs free energy for O_2 adsorption[247]. This reduction suggests a strong link between electron transfer and the observed increase in H_2O_2 production rate for NC@TiO_2 under

full-spectrum illumination. Given this correlation, our initial focus is directed toward examining the electron transfer to the Au core to understand the mechanisms responsible for the enhanced H_2O_2 production rate in the NC@TiO_2 system.

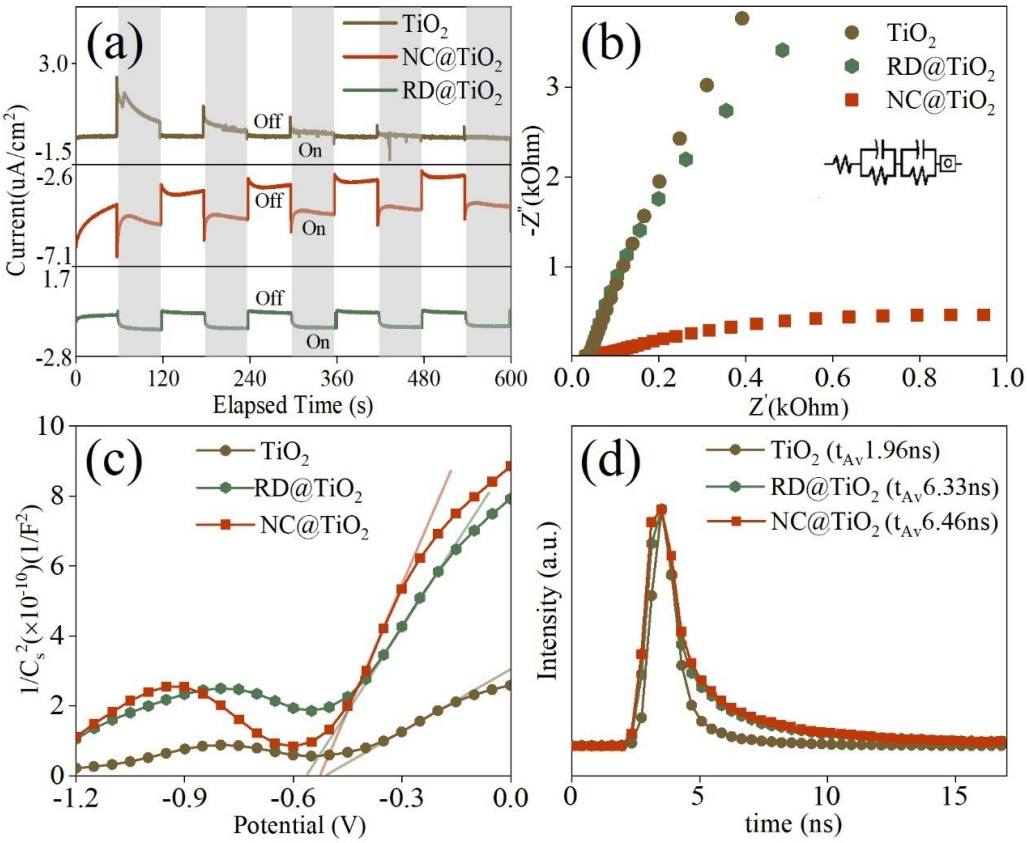

Figure 5.10: Mechanism investigation of the outstanding H_2O_2 production activity. (a) Chopped-light current plot, the starting point of plots, the starting current value is modified to separate the three curves so that readers can have an intuitive impression. **(b)** EIS Nyquist plot, **(c)** Mott-Schottky plots, **d.** TRPL result of NC@TiO_2, RD@TiO_2 and TiO_2.

Electrochemical measurements were firstly employed to elucidate the charge carrier behavior in these nanostructures. The chopped-light current response, shown in Figure 5.10(a), demonstrates that NC@TiO_2 exhibits the highest stable photocurrent, reaching 1.39 μA/cm^2 at -0.3 V versus Ag/AgCl under full-spectrum illumination. In comparison, RD@TiO_2 and pure TiO_2 generated significantly lower photocurrents of 0.62 μA/cm^2 and 0.10 μA/cm^2, respectively. The elevated photocurrent in NC@TiO_2 suggests a higher density of charge carriers, prompting further electrochemical investigations under Xe lamp illumination. The impedance spectroscopy (EIS) results, shown in Figure 5.10(b), indicate that NC@TiO_2 exhibits the lowest resistance of 811 Ω under full-spectrum illumination, which is only 19% of the resistance of RD@TiO_2 (4326 Ω) and 7% of pure TiO_2 (11,080 Ω). These results suggest that NC@TiO_2 features superior charge transport properties. Mott-Schottky (MS) analysis shown in Figure 5.10(c), performed at 1000 Hz, provides further insights. The carrier density, N_D, in the TiO_2

shell was calculated using the Mott-Schottky equation:

$$N_D = \frac{2}{\varepsilon\varepsilon_0 e \cdot \text{slope}},$$

where ε is the dielectric constant, ε_0 is the permittivity of free space, and e is the elementary charge. NC@TiO_2 exhibits the largest slope, corresponding to the lowest electron density in the TiO_2 shell (5.99×10^{10} cm^{-3}), compared to RD@TiO_2 (16.06×10^{10} cm^{-3}) and pure TiO_2 (24.37×10^{10} cm^{-3}). These findings, together with the high photocurrent and low impedance, confirm that electron transfer from the TiO_2 shell to the Au core is more efficient in NC@TiO_2 compared to RD@TiO_2. Additionally, NC@TiO_2 demonstrates a more positive flat-band potential (74 mV vs. NHE) compared to RD@TiO_2 (36 mV vs. NHE), as illustrated in Figure 5.10(c). This indicates a lower conduction band position in NC@TiO_2, which facilitates electron transfer to the Au core by reducing the Schottky barrier. A similar trend was observed at 1500 Hz, as shown in Figure 5.12. Furthermore, the extended lifetime of electron-hole (e-h) pairs in TiO_2 within the Au@TiO_2 nanostructures is evident in the time-resolved photoluminescence (TRPL) and steady-state photoluminescence (PL) spectra at 468 nm, as shown in Figure 5.10 (d) and Figure 5.11, respectively. The presence of Au cores increased the e-h pair lifetimes from under 2 ns to over 6 ns, representing a more than threefold improvement. However, minimal variation in hot electron lifetimes was observed between NC@TiO_2 and RD@TiO_2. These findings underscore the importance of charge transfer and structural design in optimizing photocatalytic performance.

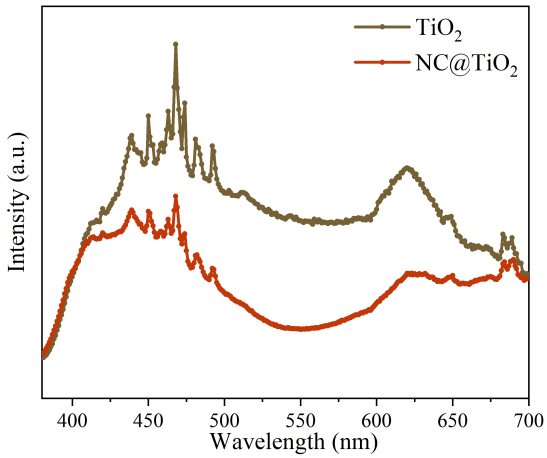

Figure 5.11: Stable photoluminescence spectrum of NC@TiO_2 and TiO_2.

To further understand the role of plasmon excitation in Au nanoparticles (NPs) on electron transfer within hybrid nanostructures, X-ray photoelectron spectroscopy (XPS) measurements were performed under 532 nm illumination. The data revealed a reverse electron transfer, specifically from the Au core to the TiO_2 shell, under localized surface plasmon resonance (LSPR) excitation. The XPS spectra for O 1s, Au 4f, and Ti 2p in RD@TiO_2 are presented in Figure 5.15(a) and Figure 5.13. Compared to dark

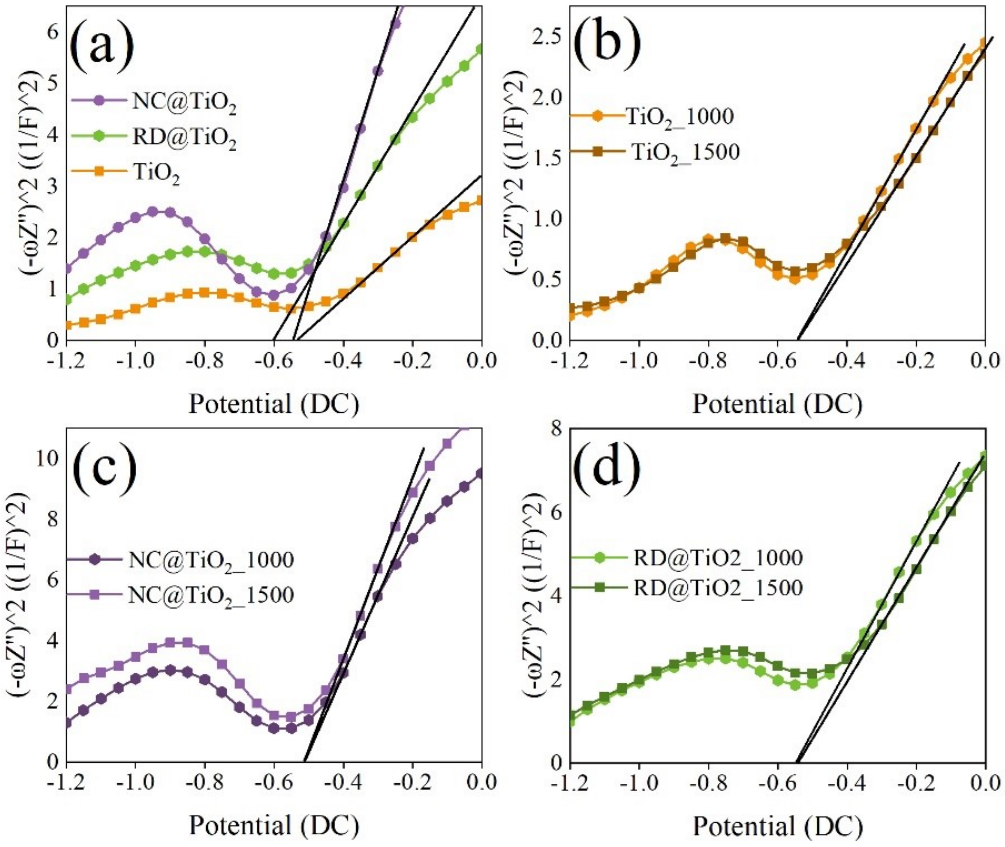

Figure 5.12: Mott-Schottky plots under illumination with 1500 Hz. (a) MS plots with NC@TiO_2, RD@TiO_2 and TiO_2 with setting potential as 1500 Hz. **(b-d)** MS plots of **(b)** TiO_2, **(c)** NC@TiO_2 and **(d)** RD@TiO_2 with setting potentials as 1000 and 1500 Hz, all materials show same flat-band potential under both frequencies.

conditions, the Au 4f peak in RD@TiO_2 exhibits a positive shift of 0.15 eV under illumination, while the O 1s peak shows a negative shift of 0.07 eV. A similar trend is observed in NC@TiO_2, as presented in Figure 5.14. These results confirm that LSPR excitation induces a reverse electron transfer from the Au core to the TiO_2 shell upon LSPR excitation.

This reverse electron transfer suggests a novel pathway facilitated by LSPR. As detailed in the synthesis and characterization section, under UV illumination, electrons generated in the TiO_2 conduction band transfer to Au, while the corresponding holes migrate to the Au-O-Ti interfacial states. In contrast, LSPR excitation generates additional hot electrons within the Au core. Among these, lower-energy hot electrons preferentially transfer to TiO_2, where they recombine with holes at the Au-O-Ti interface. This recombination mitigates electron-hole pair annihilation within TiO_2, thereby enhancing the transfer of high-energy electrons from TiO_2 to the Au core. The proposed mechanism is illustrated in the right panel of Figure 5.1.

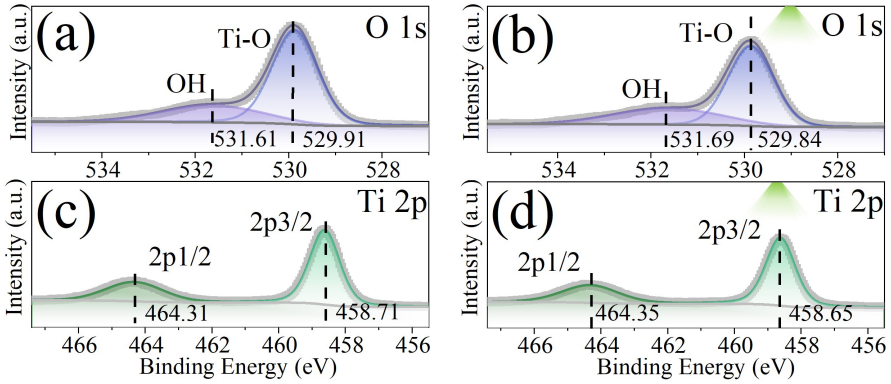

Figure 5.13: XPS specific spectrum of RD@TiO_2 in dark and under 532 nm illumination.

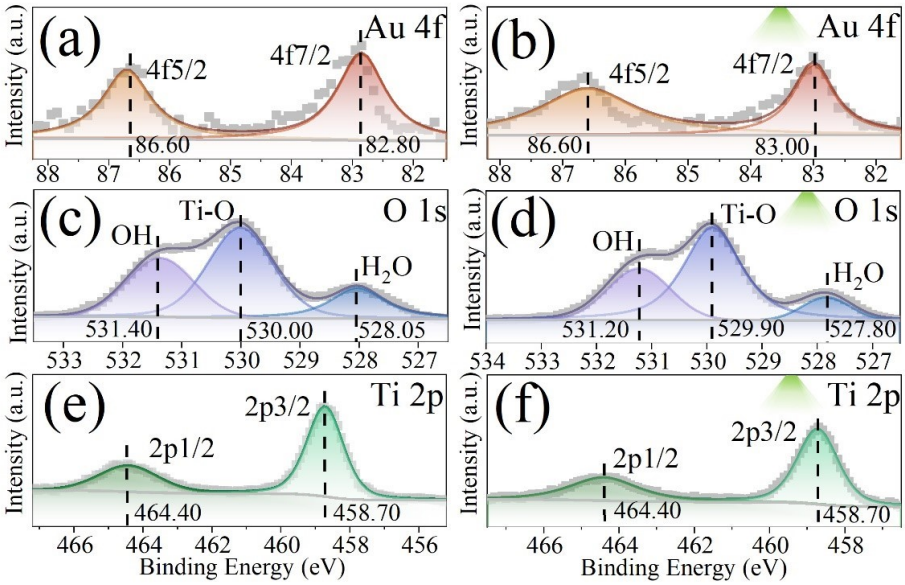

Figure 5.14: XPS specific spectrum of NC@TiO_2 in dark and under 532 nm illumination.

Beyond hot electron generation, LSPR also amplifies the local electric field, which is crucial for electron transfer. To explore this phenomenon, we performed Bader charge analysis on the charge distribution of the $Ti_{12}O_{18}$ cluster supported on Au(100) under different external electric fields. The model built for DFT calculations is shown in Figure 5.15(d) and the calculation results are shown in Figure 5.15(c). When the $Ti_{12}O_{18}$ cluster is supported on Au(100) with no external electric field applied, 1.226 electrons are transferred from $Ti_{12}O_{18}$ to Au(100). When the external electric field is increased to - 0.5 V/Å, the electron transfer from $Ti_{12}O_{18}$ to Au(100) increases to 1.766 electrons. These findings demonstrate that the electric field generated by the plasma effect can effectively facilitate the charge transfer between TiO_2 cluster and Au(100), thereby accelerating the injection of electrons from the TiO_2 conduction band into the Au(100) surface, thus promoting the occurrence of the oxygen reduction reaction. To further investigate, COMSOL simulations were used to evaluate the

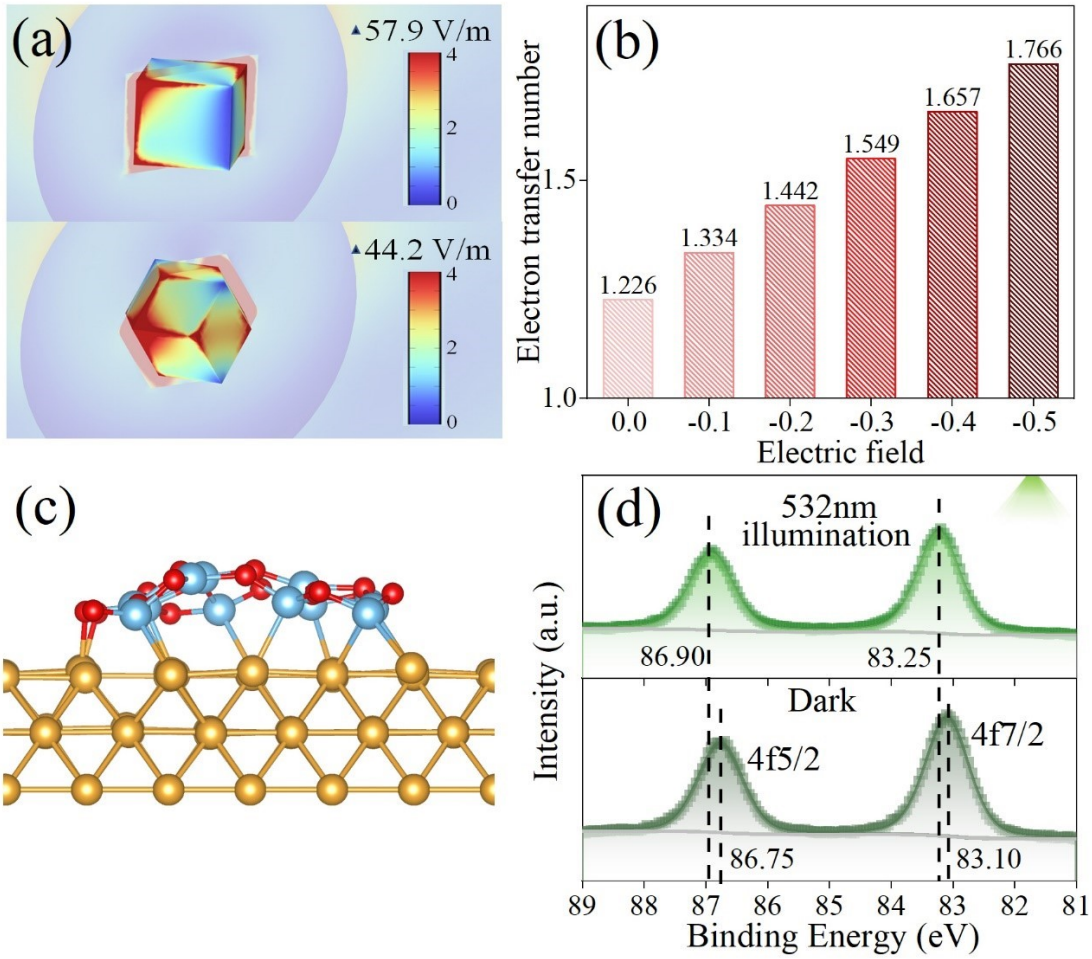

Figure 5.15: Mechanism understanding of plasmon enhancing photocatalytic H_2O_2 production. **(a)** Electric field enhancement on NC@TiO_2 and RD@TiO_2 upon plasmon excitation based on COMSOL simulations. **(b)** Effect of electric field enhancement upon the electron transfer from TiO_2 to Au. **(c)** The model of Au@TiO_2 nanostructure for DFT calculation. **(d)** High-resolution XPS spectra of Au 4f of RD@TiO_2 under dark conditions and 532 nm illumination.

electric field enhancement under LSPR excitation at 540nm for NC@TiO_2 and RD@TiO_2, as shown in Figure 5.15(b), and for their corresponding Au cores, as detailed in Figure 5.16. The simulations revealed that NC@TiO_2 exhibited an electric field enhancement of 57.9 V/m, approximately 30% greater than RD@TiO_2 (44.2 V/m). A similar trend was observed for isolated Au nanoparticles under LSPR excitation. In contrast, under UV illumination at 290 nm, negligible electric field enhancement was detected (Figure 5.17), highlighting the unique contribution of LSPR. The strong electric field induced by LSPR enhances electron transfer from TiO_2 to Au, reducing the energy barrier for O_2 activation and improving the efficiency of H_2O_2 production. The superior LSPR response of NC@TiO_2 leads to a stronger electric field, which contributes to its higher H_2O_2 yield compared to RD@TiO_2.

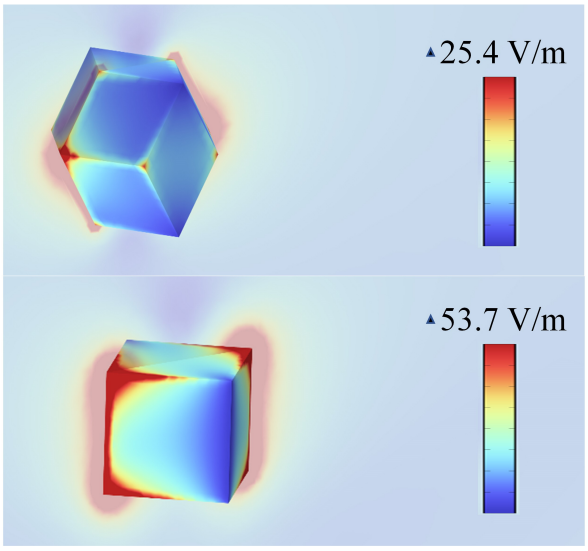

Figure 5.16: COMSOL simulation of Au nanoparticles with 540 nm illumination.

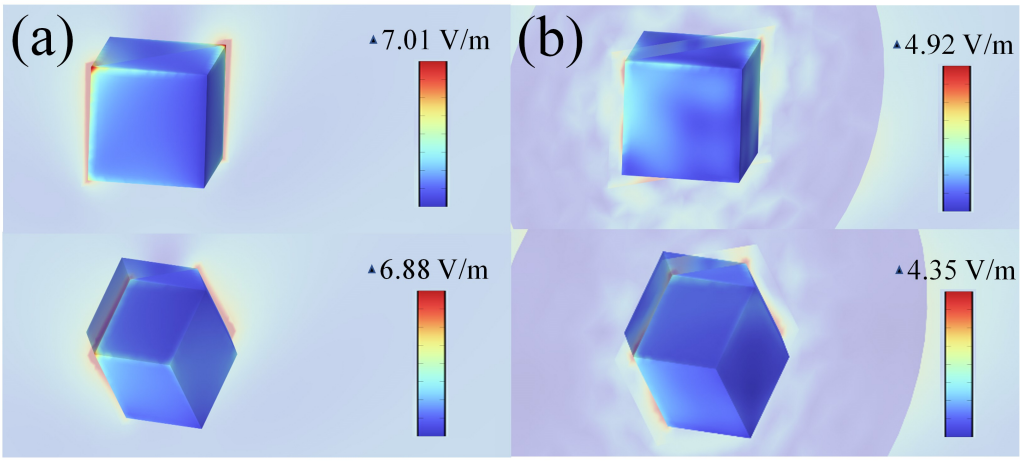

Figure 5.17: COMSOL simulation with UV excitation (290 nm) of **(a)** Au nanoparticles and **(b)** Au@TiO_2 nanostructures.

In summary, experimental and simulation-based analyses provide a comprehensive understanding of the mechanisms underlying the exceptional photocatalytic performance of Au@TiO_2 hybrid nanostructures, as well as the influence of Au core morphology on catalytic efficiency. Electron transfer to Au facilitates O_2 activation, the rate-limiting step in H_2O_2 production. LSPR contributes to this process through two primary mechanisms: first, hot electrons generated within Au transfer to TiO_2 and consume holes at the Au-O-Ti interface, thereby reducing electron-hole recombination and enabling more efficient electron transfer from TiO_2 to Au for O_2 activation. Simultaneously, residual hot electrons directly participate in O_2 reduction. Second, the electric field enhancement induced by LSPR accelerates electron transfer from TiO_2 to Au, as corroborated by density DFT calculations. The stronger LSPR response of Au NCs results in increased hot electron generation and

a more substantial surface electric field, leading to enhanced electron accumulation in the Au core and significantly improved H_2O_2 production. In contrast, Au RDs, with their weaker LSPR response, exhibit comparatively modest improvements in catalytic performance.

5.3 Summary

This study examined the impact of plasmonic resonance on the photocatalytic production of hydrogen peroxide (H_2O_2) in gold/porous anatase hybrid core-shell nanostructures featuring two distinct core geometries: cubes (NC@TiO_2) and rhombic dodecahedron (RD@TiO_2). The integration of Au with TiO_2 optimized energy band alignment, reduced the activation energy barrier for oxygen activation, and facilitated the formation of an interfacial Au-O-Ti state. These features lead to the electron transfer from the TiO_2 shell to the Au core, effectively promoting the separation of high-energy electron-hole pairs within TiO_2. As a result, NC@TiO_2 demonstrated an exceptional H_2O_2 production rate, achieving 5.4 mM in 3 hours, which is among the highest reported for similar hybrid systems.

The role of localized surface plasmon resonance (LSPR) in improving photocatalytic efficiency was particularly pronounced, with significant differences observed between the two morphologies. Under combined UV and 525 nm illumination, NC@TiO_2 exhibited a 52% increase in H_2O_2 production compared to UV-only conditions. In contrast, RD@TiO_2 achieved a comparatively modest 18% enhancement. Both experimental observations and theoretical modeling identified the superior plasmonic performance of NC@TiO_2 as the key factor underlying this difference. The intensified electric field generated by the LSPR of Au nanocubes facilitated more efficient electron transfer from TiO_2 to the Au core. Furthermore, hot electrons generated through plasmonic excitation contributed to oxygen activation and played a critical role in recombining with holes in the Au-O-Ti interfacial state. This recombination suppressed electron-hole pair annihilation in the TiO_2 shell, enabling a greater transfer of energetic electrons to the Au core. Consequently, NC@TiO_2 demonstrated a higher electron density within the Au core, effectively lowering the activation energy barrier for oxygen activation and driving superior H_2O_2 production.

This investigation highlights the fundamental influence of plasmonic excitation on charge carrier dynamics and the photocatalytic enhancement of hybrid Au@TiO_2 nanostructures. The stronger LSPR response observed for Au NCs, relative to RDs, underscores their superior catalytic performance in H_2O_2 production. Similar trends were observed in earlier studies of plasmon-driven electrocatalytic CO_2 reduction, where NCs demonstrated greater plasmonic response and realized a larger activity and selectivity enhancement in electrocatalytic CO_2 reduction system compared to RDs. These consistent observations across different catalytic applications suggest that the plasmonic properties of nanostructures are intrinsically linked to their morphology. This work offers guidance for the design of plasmonic catalysts with more desirable catalytic performances and highlights the broader potential of plasmonic systems for efficient energy conversion processes.

5.4 Methods

Characterization

Transmission electron microscopy (TEM) was performed using a JEM1011 microscope operating at 80 kV. High-resolution TEM (HRTEM) and elemental mapping images were obtained using a Titan G2 60–300 microscope. Scanning electron microscopy (SEM) was conducted with a TESCAN MIRA3 field emission microscope. X-ray diffraction (XRD) patterns were recorded using a D8 Advance diffractometer equipped with Cu Kα radiation (λ = 1.54 Å, Rigaku). X-ray photoelectron spectroscopy (XPS) measurements were carried out on a Thermo Scientific Nexsa G2 system, with binding energies calibrated to the C 1s peak at 284.8 eV. UV–Vis–NIR absorption spectra were acquired using a Lambda 750 spectrometer (PerkinElmer). Fourier transform infrared (FT-IR) spectra were collected in transmission mode using a Thermo Fisher Nicolet iS5 spectrometer. Photoluminescence (PL) and time-resolved photoluminescence (TRPL) measurements were performed for optical characterization, with further details provided in the main text.

Photocatalytic H_2O_2 Production Experiment

Photocatalytic H_2O_2 production was investigated in a 100 mL multi-channel reactor. To minimize H_2O_2 decomposition, the reaction temperature was maintained at 6 °C using a temperature-controlled water bath. For a typical experiment, 5 mg of catalyst was dispersed in a 20 mL methanol-water solution (10% v/v). The suspension was stirred in the dark for 30 minutes to ensure adsorption equilibrium before illumination with a light source under continuous magnetic stirring.

The concentration of H_2O_2 was determined using iodometric titration, following established protocols. Briefly, 500 μL of the reaction mixture was centrifuged to remove the catalyst. A 200 μL aliquot of the supernatant was diluted to 1 mL with deionized water and then mixed with 1 mL of 0.4 M KI and 1 mL of 0.1 M potassium hydrogen phthalate. After incubation for 3 hours, the reaction produced triiodide (I_3^-) under acidic conditions, which absorbs light at 350 nm. The absorbance at 350 nm was measured using UV-Vis spectroscopy to quantify the concentration of I_3^-, enabling calculation of the H_2O_2 concentration.

Electrochemical Measurements

Photoelectrochemical analyses were performed in a standard three-electrode setup containing 0.5 mol L^{-1} Na_2SO_4 aqueous solution (100 mL). The reference electrode was Ag/AgCl, and the counter electrode was platinum. For the working electrode preparation, 5 mg of catalyst powder was dispersed in a mixture of 1 mL ethanol and 1 mL deionized water, followed by the addition of 30 μL of Nafion. After sonication for 1 minute to ensure uniform dispersion, the resulting "ink" was prepared.

For chopped-light current-time (I-t) and electrochemical impedance spectroscopy (EIS) measurements, 50 μL of the ink was applied to a 0.5 cm $\times$ 1 cm area on ITO glass and allowed to dry naturally to form the working electrode. The experiments were conducted using an SP-300 electrochemical workstation (BioLogic) with a 500 W Xenon lamp (Oriel Instruments) as the light source.

For Mott-Schottky analysis, 20 μL of the ink was deposited on a 0.5 cm-diameter area of ITO glass and dried naturally. Measurements were performed using a Nova electrochemical workstation (Metrohm Autolab) with a 140 W xenon lamp (LDLS, Energetiq) as the illumination source. The electrochemical results were analyzed to assess the photoelectrochemical performance of the catalysts.

DFT computational details.

Spin-polarized density functional theory (DFT) calculations were performed using the Vienna Ab initio Simulation Package (VASP)[248,249]. The Perdew-Burke-Ernzerhof (PBE) functional within the generalized gradient approximation (GGA) was employed for electron exchange and correlation[250], and the projector augmented wave (PAW) method[251,252] was applied to describe the ionic cores. For geometry optimization, a Monkhorst-Pack K-point grid of 1 × 1 × 1 was utilized, while for static calculations, a 2 × 2 × 1 grid was adopted. The plane-wave cutoff energy was set to 400 eV, and the convergence criteria for electronic energy and forces were defined as 10-5 eV and 0.02 eV/Å, respectively. Van der Waals interactions were accounted for using Grimme's D3 correction[253]. A vacuum space of approximately 20 Å was incorporated to separate periodic images. The Au(100) surface was modeled with a 6 × 6 supercell comprising three layers, with the bottom layer fixed and the top two layers allowed to relax. For the Ti 3d orbitals, the effective Hubbard-U parameter was set to 4.2 eV.

6

Plasmon-Enhanced Single-Atom Catalysts for Plastic Photoreforming

6.1 Research background

Plastic pollution has become a persistent global challenge, posing severe environmental risks. Plastic waste is estimated to persist in ecosystems for extended periods, infiltrating the food chain and causing cascading effects on both local and global scales[254,255]. Addressing this issue, the plastic photoreforming - catalytic conversion of plastic waste into hydrogen (H_2) fuel and value-added chemicals presents a clean, environmentally sustainable strategy. This approach not only mitigates plastic pollution but also promotes plastic upcycling, benefits the hydrogen industry, and reduces reliance on nonrenewable fossil fuels.

A recent study by Dr. Tian and Dr. Zhang introduced a single-atom iron catalyst-H_2O_2 system, demonstrating high-efficiency degradation of ultrahigh-molecular-weight polyethylene (UHMWPE) through a hydrothermal process at 140–160 °C[117]. The reaction yielded alcohols, aldehydes/ketones, and carboxylic acids, with a carboxylic acid selectivity of 64%. However, the requirement for hydrothermal conditions limits its scalability, and further improvements in product selectivity are needed for industrial applications.

Solar-driven photocatalysis offers an alternative, environmentally friendly approach for converting pre-treated plastic waste into H_2 fuel and valuable chemicals under ambient conditions. However, achieving large-scale and sustainable photocatalytic conversion requires the development of photocatalysts with high activity, excellent selectivity, and long-term stability. Carbon nitride (CN)-supported single-atom catalysts have emerged as promising materials for various photocatalytic reactions due to their environmental friendliness, cost-effectiveness, strong light-harvesting ability, and facile synthesis[256]. Nonetheless, the conversion of plastic waste remains highly challenging, necessitating further technological and catalyst advancements.

In parallel, plasmonic catalysis has gained significant attention as a novel approach in heterogeneous photocatalysis due to its unique ability to enhance catalytic activity and selectivity[257]. Plasmonic catalysts utilize light to excite localized surface plasmons, resulting in significant electromagnetic field enhancement. The decay of surface plasmons generates high-energy electron-hole pairs on the catalyst surface, which can drive chemical transformations. Additionally, plasmonic catalysts have the potential to selectively activate chemical bonds in adsorbed molecules, directing specific reaction pathways.

This project aims to integrate the advantages of macroporous CN-supported Fe single-atom catalysts with plasmonic gold nanoparticles (Au-FeSA-MCN) to develop highly selective and efficient photocatalysts for solar-driven plastic conversion into H_2 and value-added chemicals (Figure 6.1). Common plastic waste will first undergo mild chemical pre-treatment with alkali or oxidants at elevated temperatures to break down polymer structures into monomers, oligomers, and oxidized organics. The catalytic performance of the plasmonic Au-FeSA-MCN photocatalysts will then be evaluated for their ability to convert pre-treated plastic waste into clean, carbon-free H_2 fuel and valuable chemical products.

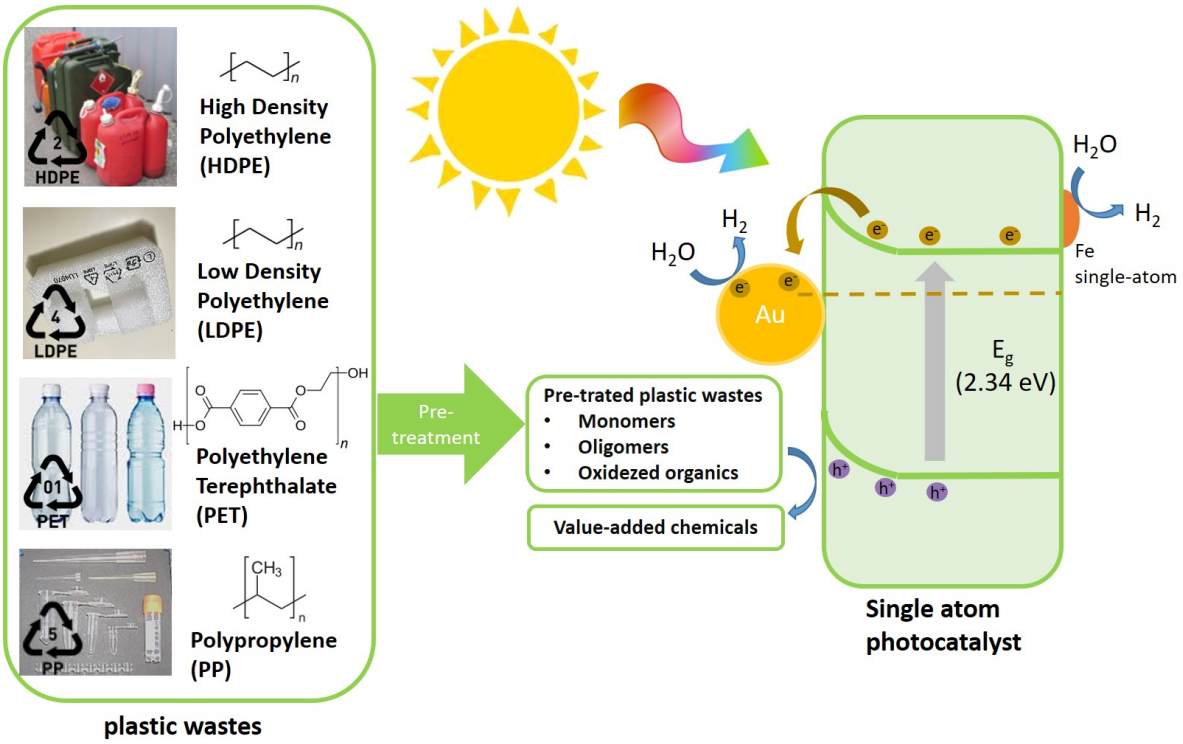

Figure 6.1: The basic mechanism of solar-driven plastic waste conversion on CN-supported Fe single-atom catalysts with plasmonic gold nanoparticles (Au-FeSA-MCN). The energy bandgap values are referenced from the publication[117].

6.2 Results and dicussion

In this study, we synthesized engineered macroporous FeSA-MCN using an advanced one-pot SiO_2-templated pyrolysis strategy, based on the method described in a previous publication[117]. Green and cost-effective organic precursors, including urea, melamine, dicyandiamide, and thiourea, were employed to produce MCN, while earth-abundant transition metal Fe was incorporated as single-atom sites on the CN framework, as illustrated in Figure 6.2 (a). The resulting FeSA-MCN exhibited an ordered macroporous structure (around 300 nm), which facilitates the later Au loading. To evaluate the photoelectrochemical properties of the materials, photocurrent measurements were conducted on both MCN and FeSA-MCN. The results demonstrated that Fe loading notably enhanced the photoresponse of MCN, with the photocurrent increasing from 0.15 to 0.25 mA/cm^2, as shown in Figure 6.3 (a). This enhancement suggests that Fe single-atom sites contribute to improved charge carrier dynamics.

Subsequently, Au nanocubes (NCs) were synthesized following a previously reported method[115] and loaded onto FeSA-MCN with a Au mass loading of 10 wt%. To strengthen the interfacial connection between FeSA-MCN and Au NCs, an annealing treatment was performed at 300°C for 2 hours. The role of annealing in enhancing the interfacial connection was confirmed by electrochemical measurements based on Au-MCN and MCN, with Au-MCN exhibiting a more pronounced photocurrent, almost doubled (from 0.26 to 0.48 mA/cm^2), as demonstrated in Figure 6.3 (b). As depicted in Figure 6.2(b-c), the Au NCs remained well-dispersed across the FeSA-MCN surface without noticeable aggregation. Interestingly, the UV-Vis spectrum of FeSA-MCN showed no significant changes compared to that of MCN, nor did it exhibit a distinct Au plasmon peak. However, a noticeable color change in the material was observed, as shown in Figure 6.2 (d-e), indicating successful Au incorporation. Electrochemical impedance spectroscopy (EIS) results further confirmed the incorporation of Au, as shown in Figure 6.3 (c-d). The loading of Au onto both MCN and FeSA-MCN resulted in lower resistance with smaller tangent slope compared to the materials without Au NCs. These results also suggest improved charge transfer efficiency by loading Au NCs.

The catalytic plastic photoreforming performance of the prepared materials was evaluated. The plastic samples were first pretreated using an alkaline solution (6 M KOH). The plastic bottles, primarily composed of polyethylene terephthalate (PET), were purchased from a supermarket, cut into small pieces (5 mm × 5 mm), thoroughly cleaned with deionized water and ethanol, and then dried to determine their initial weight. Subsequently, 2 grams of plastic pieces were immersed in 50 mL of 6 M KOH solution and stirred vigorously at 60°C for 3 days. After the pretreatment, the remaining plastic pieces were filtered, washed, and dried, while the supernatant was collected and diluted by half with deionized water for later catalytic performance measurements. By weighing the dried plastic residues, a weight loss of 0.3 grams was observed, confirming that a portion of the plastic had been converted into monomers soluble in the alkaline solution. The pre-treatment operation flow is shown in Figure 6.4.

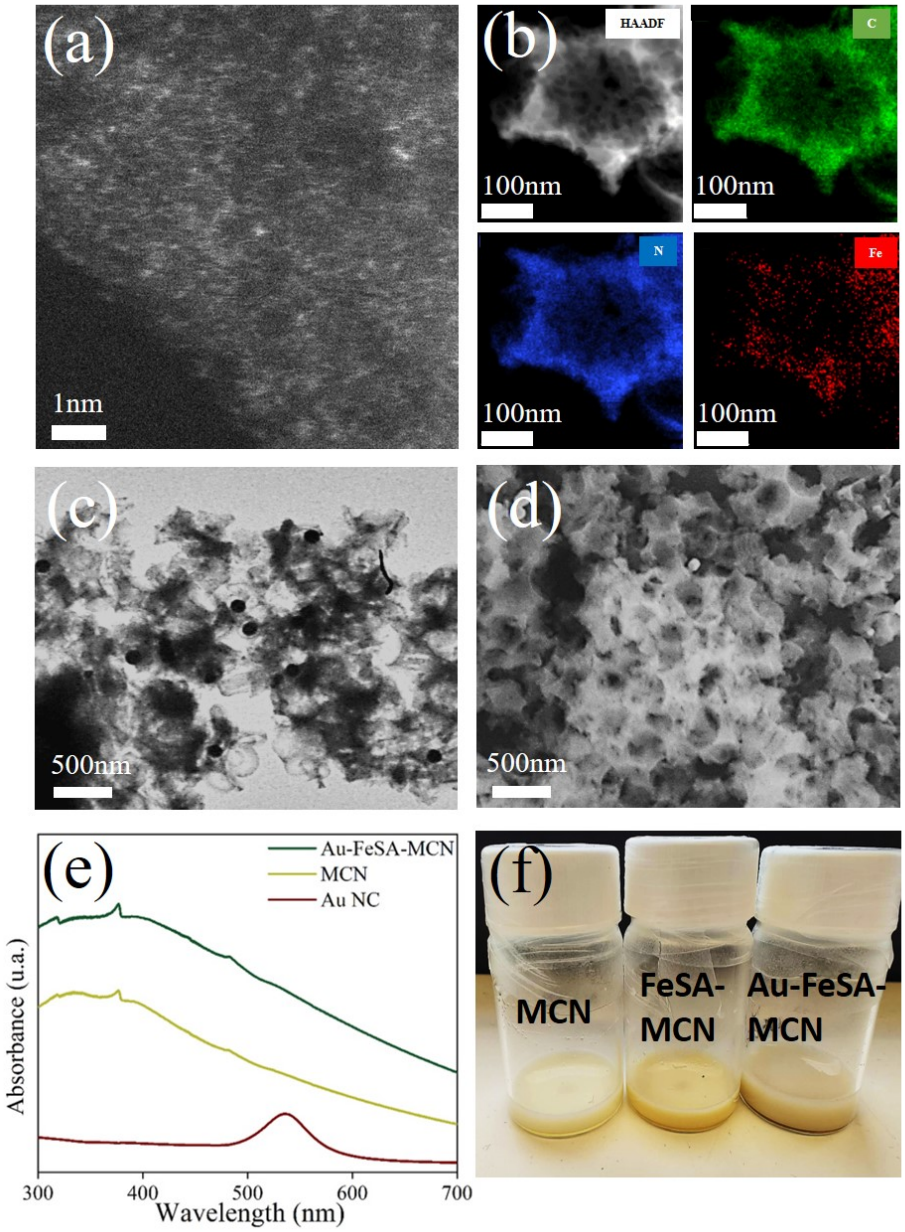

Figure 6.2: Structural characterization of catalysts. (a) Aberration-corrected (AC) HAADF-STEM image, **(b)** HAADF-STEM image and energy-dispersive X-ray spectroscopy (EDX) elemental mapping images of prepared FeSA-MCN. **(c)** TEM and **(d)** SEM images of Au-FeSA-MCN. **(e)** UV-vis absorption spectrum of MCN, Au NCs and Au-FeSA-MCN. **(f)** photo of the prepared samples. From left to right: MCN, FeSA-MCN and Au-FeSA-MCN.

To analyze the liquid-phase products formed during the plastic pretreatment, proton nuclear magnetic resonance (^{1}H NMR) spectroscopy was conducted. A solution mixture was prepared by combining 0.09 mL of plastic solution, 0.81 mL of deionized water, 0.1 mL of deuterium oxide (D_2O), and 1 µL of dimethyl sulfoxide (DMSO). This mixture was thoroughly homogenized and injected into

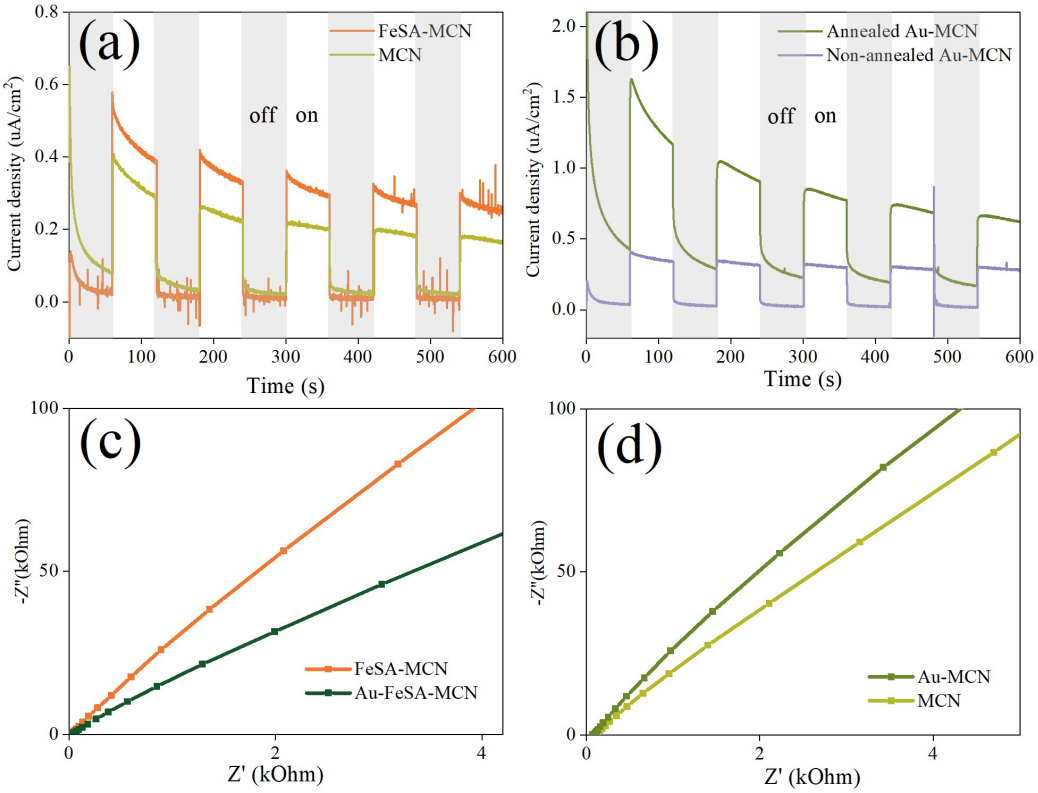

Figure 6.3: Electrochemical measurement results. (a-b) Chopped-light chronoamperometry with a 500 W Xeon lamp at the potential of open-circuit potential plus +0.2 V on catalysts. **(a)** Effect of Fe single atom loading. **(b)** Effect of annealing for Au NCs loading. **(c-d)** Electrochemical impedance spectroscopy with measurements taken at the open-circuit potential obtained from OCPT experiments. The frequency was ranged from 10^5 Hz to 0.1 Hz. **(c)** Effect of loading Au in FeSA-MCN. **(d)** Effect of loading Au in MCN.

an NMR tube for analysis. By referencing previous literature[258], the detected products were identified as primarily ethylene glycol, exhibiting a peak at approximately 3.53 ppm, and terephthalate, with a peak around 7.74 ppm. The peak at 2.58 ppm corresponds to the NMR internal standard, DMSO. A representative ^{1}H NMR spectrum is shown in Figure 6.6 (a).

In a standard plastics photoreforming experiment, 12 mL of plastic solution was combined with 5 mg of catalyst through a 1-minute sonication process to ensure uniform dispersion. The resulting mixture was transferred to a 22 mL reactor equipped with a magnetic stirring bar, as depicted in Figure 6.5 (a). Continuous magnetic stirring was maintained throughout the measurement to ensure consistent mixture homogeneity. The reactor's open window was sealed with a high-light-transmittance glass, through which a 1000 W Xenon lamp provided illumination. A circulating cooling system maintained the reaction temperature at 40°C. The reactor was completely sealed, with a rubber stopper in the lid, facilitating real-time collection of gaseous and liquid products.

We then evaluated H_2 production with gas chromatography. For each measurement, 400 uL gas mixture above the solution surface was extracted and injected into the GC. The H_2 production over

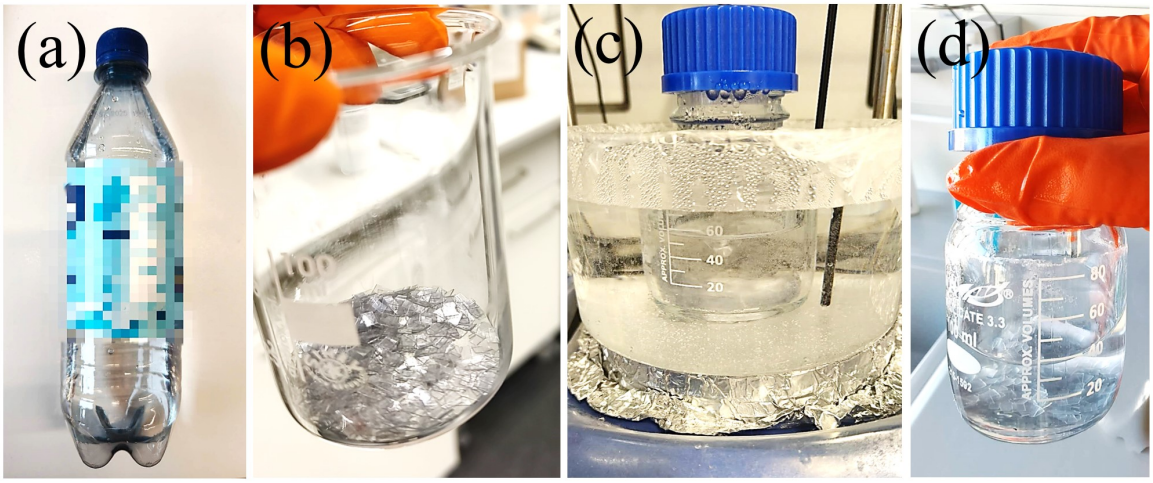

Figure 6.4: Plastic preparation. (a) Plastic bottles were purchased from a supermarket, **(b)** then cut into small pieces (5 mm × 5 mm), **(c)** 2 g of plastic pieces were immersed in 50 mL of 2 M KOH solution and stirred at 60°C. **(d)** After 3 days, the pretreatment was completed, and the remaining plastic pieces were filtered. The supernatant was collected and diluted by half for catalytic performance measurements.

a 3-hour period using pure MCN, Au-loaded MCN, and Au-loaded macroporous CN-supported Fe single-atom catalysts was illustrated in Figure 6.5 (b). Despite the potential of Au to enhance the photocatalytic H_2 production performance of MCN according to literature[259], loading Au nanocrystals on pure MCN failed to yield substantial improvements. However, when Au NCs were loaded on FeSA-MCN, a notable enhancement in H_2 production was observed. After 3 hours, H_2 production with Au-FeSA-MCN catalysts reached 0.14 umol, compared to 0.10 umol for MCN and Au-MCN. These results suggest a synergistic interaction between Au and Fe single atoms.

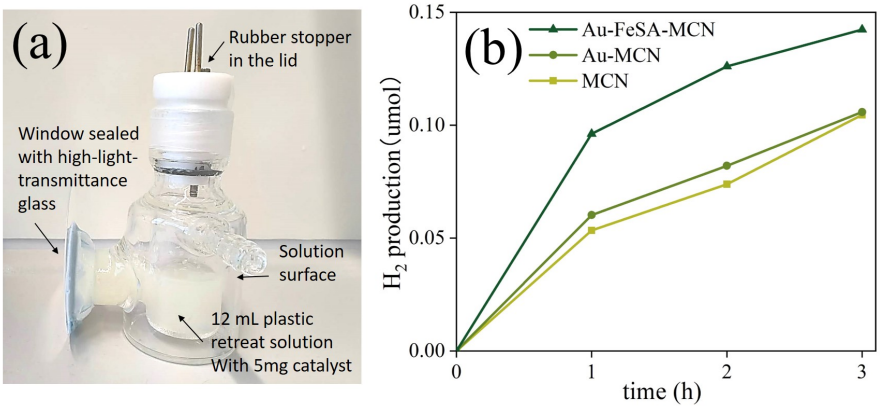

Figure 6.5: H_2 production. (a) Measurement setup for the plastic photoreforming measurement. **(b)** H_2 production of Au-FeSA-MCN, Au-MCN and MCN within 3 hours.

Liquid products in the mixture were analyzed via ^{1}H NMR, following the same sample preparation procedure as used for plastic solution content measurement. The content of ethylene glycol and

terephthalate within a photocatalytic measurement of 3 hours are shown in Figure 6.6 (b) and (c), respectively. A decreasing trend was observed for both monomers over time, suggesting the catalytic activity of our materials in facilitating plastic degradation. The data for terephthalate with Au-MCN at 2 hours was missing due to a measurement error, and the monoment content for MCN system was only tested once after photocatalysis measurement finished. Among the tested catalysts, Au-FeSA-MCN exhibited the best plastic photoreforming performance compared to Au-MCN and pure MCN, highlighting its potential for efficient plastic upcycling and hydrogen generation.

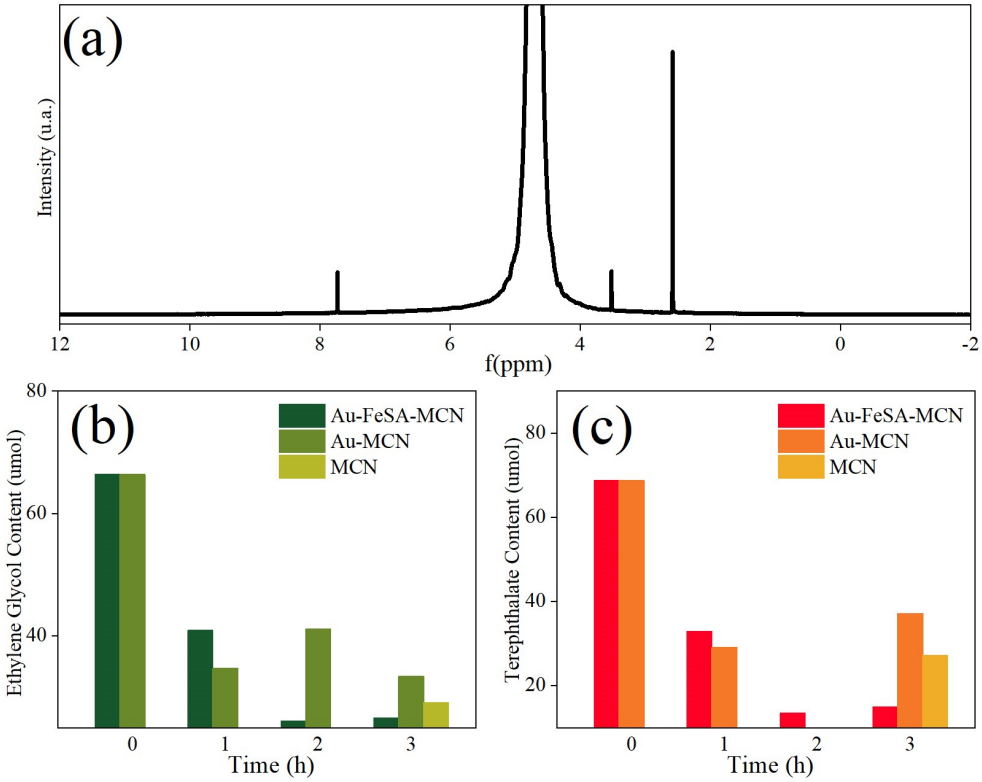

Figure 6.6: Products Formed from Plastic. (a) A typical ^{1}H NMR spectrum of the plastic products. Content of **(b)** ethylene glycol and **(c)** terephthalate in the plastic solution in the time period of 3 hours.

6.3 Discussion and outlook

In this study, we developed a novel catalyst, macroporous CN-supported Fe single-atom catalysts with plasmonic gold nanoparticles (Au-FeSA-MCN), for plastic photoreforming to convert plastics into valuable chemicals while producing H_2. Following alkali pretreatment, ethylene glycol and terephthalate emerged as the primary plastic conversion products. By quantifying H_2 production and liquid product concentrations, we evaluated the catalytic performance of our prepared materials.

The results revealed a potential synergistic interaction between Au nanoparticles and Fe single atoms, demonstrating the promising capabilities of Au-FeSA-MCN in plastic photoreforming. However, several challenges remain unresolved. For example, the Au and Fe single-atom loading ratio should be optimized to further enhance the H_2 yield and plastic degradation efficiency. Moreover, charge carrier transfer dynamics, particularly at interfaces between different components, is crucial in catalytic processes. Further investigation and optimization of this process provide more potential in increasing the catalytic performance of the materials.

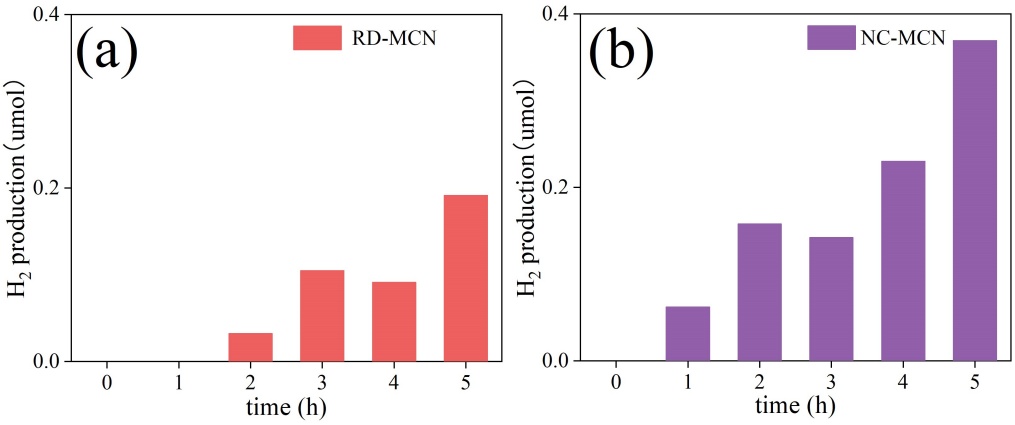

Figure 6.7: Photocatalytic H_2 production within 5h on NC-MCN and RD-MCN.

Interestingly, in our investigation of Au-MCN catalysis for plastic photoreforming, we observed that the morphology of Au nanoparticles has a significant impact on the catalytic performance of the composites, as illustrated in Figure 6.7. Both Au NCs and rhombic dodecahedrons (RDs) were loaded at a fixed mass ratio of 10 wt%. However, their catalytic activities for H_2 production showed a clear difference — after 5 hours of illumination, RD-MCN generated 0.19 µmol of H_2, while NC-MCN produced 0.37 µmol. To be mentioned, the experimental setup for these two tests (5 mL solution with 8 mg of catalyst) differed from the previously mentioned testing conditions.

Studies described in Chapter 4 and 5 have demonstrated that Au NCs exhibit a stronger plasmonic response than RDs. Consistently, the results from our Au-MCN system align with this trend, further indicating that localized surface plasmon resonance (LSPR) plays a key role in catalytic activity. Given this observation, it is likely that LSPR also contributes to the enhanced performance of the Au-FeSA-MCN system. To fully understand the mechanisms by which plasmons influence plastic photoreforming performance, further studies are required. The precise mechanisms by which plasmons enhance catalytic performance necessitate further comprehensive investigation through ex-situ and in-situ characterizations and theoretical calculations.

7

Conclusion and Outlook

This thesis presents a comprehensive exploration of plasmonic nanocatalysts for energy conversion, beginning with a foundational theoretical framework, progressing through the development of synthesis and characterization techniques, and concluding with the application of these materials to address critical challenges in sustainable energy systems. The research underscores the transformative potential of plasmonic nanostructures to enhance catalytic efficiency and selectivity by leveraging sunlight as a renewable energy source.

The initial investigation centered on facet-dependent plasmonic electrocatalysis, revealing how LSPR modifies active sites, shifting them from facet-dependent configurations to low-coordination geometries. This adjustment was shown to improve both the reaction kinetics and the selectivity in CO_2 reduction reactions (CO_2RR). The property of LSPR changing the reaction active sites was further proved in hydrogen evolution reactions (HER).

Subsequent work explored the integration of gold nanoparticles with porous anatase TiO_2 shells. This study demonstrated the benefits of combining metal and semiconductor systems, not only in stabilizing nanoparticles and enhancing scattering, but more importantly, in promoting efficient sunlight absorption and directional charge transfer under LSPR excitation. This effect significantly boosted the photocatalytic H_2O_2 production rate, further emphasizing the ability of plasmonic catalysts to optimize solar energy utilization beyond conventional photovoltaics.

Another significant contribution was the development of a novel plastic photoreforming system, which combined gold nanoparticles with single-atom catalysts. This innovative approach simultaneously addressed environmental challenges by degrading plastic waste and generating hydrogen, exemplifying a dual-purpose strategy for sustainability.

Despite these advances, several challenges persist. A deeper understanding of charge carrier dynamics under LSPR excitation is essential for further enhancing catalytic performance. Moreover, the scalable and cost-effective synthesis of plasmonic nanostructures, while preserving their unique properties, remains a critical barrier to industrial applications. Addressing these challenges will be pivotal for the practical deployment of plasmonic nanocatalysts in real-world systems.

The integration of plasmonic nanomaterials with biomolecules, such as enzymes, presents an exciting avenue for future research. Such hybrid systems could exploit the broad solar absorption

capability of plasmonic nanomaterials and the high specificity of enzymatic catalysis, creating highly selective and efficient catalytic systems under mild and environmentally friendly conditions.

In summary, this thesis highlights the vital role of plasmonic nanostructures in advancing energy conversion technologies. By fully utilizing the resonance-driven light absorption properties of plasmonic nanomaterials, these systems offer a promising route to efficient and scalable solar-driven catalysis. Bridging theoretical insights with practical applications, this work lays a foundation for future advancements in the field. Achieving the full potential of plasmonic nanocatalysts will require interdisciplinary approaches, with a focus on improving material stability, scalability, and environmental sustainability. These efforts will contribute significantly to the realization of efficient and sustainable catalytic systems for energy conversion.

A
Appendix

A.1 XRD rulers

Table A.1: XRD ruler of Au in the FCC phase for Mo Kα radiation.

2-Theta (°)	d (Å)	I (f)	(h k l)	Theta (°)	$\frac{1}{2d}$	$\frac{2\pi}{d}$	n^2
17.323	2.355	100	(1 1 1)	8.661	0.2123	2.668	3
20.033	2.039	52	(2 0 0)	10.017	0.2452	3.0815	4
28.475	1.442	32	(2 2 0)	14.238	0.3467	4.3573	8
33.516	1.230	36	(3 1 1)	16.758	0.4065	5.1083	11
35.061	1.1774	12	(2 2 2)	17.531	0.4247	5.3365	12
40.710	1.0196	6	(4 0 0)	20.355	0.4904	6.1624	16
44.541	0.9358	23	(3 3 1)	22.271	0.5343	6.7142	19
45.768	0.9120	22	(4 2 0)	22.884	0.5482	6.8895	20
50.429	0.8325	23	(4 2 2)	25.214	0.6006	7.5474	24

Table A.2: XRD ruler of Au with Cu as target for FCC phase.

2-Theta(°)	d(Å)	I(f)	(h k l)	Theta(°)	$\frac{1}{2d}$	$\frac{2\pi}{d}$	n^2
38.184	2.355	100	(1 1 1)	8.661	0.2123	2.668	3
44.392	2.039	52	(2 0 0)	10.017	0.2452	3.0815	4
64.576	1.442	32	(2 2 0)	14.238	0.3467	4.3573	8
77.547	1.230	36	(3 1 1)	16.758	0.4065	5.1083	11
81.721	1.1774	12	(2 2 2)	17.531	0.4247	5.3365	12
98.133	1.0196	6	(4 0 0)	20.355	0.4904	6.1624	16
110.798	0.9358	23	(3 3 1)	22.271	0.5343	6.7142	19
115.259	0.912	22	(4 2 0)	22.884	0.5482	6.8895	20
135.416	0.8325	23	(4 2 2)	25.214	0.6006	7.5474	24

Table A.3: XRD ruler of TiO_2 with Cu as target for anatase phase.

2-Theta(°)	**d(Å)**	**I(f)**	**(h k l)**	**Theta(°)**	$\frac{1}{2d}$	$\frac{2\pi}{d}$	n^2
25.281	3.520	100	(1 0 1)	12.64	0.1420	1.7850	12.64
36.946	2.431	10	(1 0 3)	18.473	0.2057	2.5846	18.473
37.800	2.378	20	(0 0 4)	18.900	0.2103	2.6422	18.900
38.575	2.332	10	(1 1 2)	19.288	0.2144	2.6943	19.288
48.049	1.892	35	(2 0 0)	24.024	0.2643	3.3209	24.024
53.890	1.6999	20	(1 0 5)	26.945	0.2941	3.6962	26.945
55.060	1.6665	20	(2 1 1)	27.530	0.3000	3.7703	27.530
62.119	1.493	4	(2 1 3)	31.059	0.3349	4.2084	31.059
62.688	1.4808	14	(2 0 4)	31.344	0.3377	4.2431	31.344
68.760	1.3641	6	(1 1 6)	34.380	0.3665	4.6061	34.380
70.309	1.3378	6	(2 2 0)	35.154	0.3737	4.6967	35.154
74.029	1.2795	2	(1 0 7)	37.014	0.3908	4.9107	37.014
75.029	1.2649	10	(2 1 5)	37.515	0.3953	4.9673	37.515
76.017	1.2509	4	(3 0 1)	38.009	0.3997	5.0229	38.009
80.725	1.1894	2	(0 0 8)	40.362	0.4204	5.2827	40.362
82.136	1.1725	2	(3 0 3)	41.068	0.4264	5.3588	41.068
82.659	1.1664	6	(2 2 4)	41.33	0.4287	5.3868	41.33
83.146	1.1608	4	(3 1 2)	41.573	0.4307	5.4128	41.573
93.217	1.060	2	(2 1 7)	46.609	0.4717	5.9275	46.609
94.178	1.0517	4	(3 0 5)	47.089	0.4754	5.9743	47.089
95.139	1.0436	4	(3 2 1)	47.57	0.4791	6.0207	47.57
98.315	1.0182	2	(1 0 9)	49.158	0.4911	6.1709	49.158
99.801	1.007	2	(2 0 8)	49.9	0.4965	6.2395	49.9
101.217	0.9967	2	(3 2 3)	50.609	0.5017	6.3040	50.609
107.444	0.9555	4	(3 1 6)	53.722	0.5233	6.5758	53.722
108.959	0.9464	4	(4 0 0)	54.479	0.5283	6.6390	54.479
112.836	0.9246	2	(3 0 7)	56.418	0.5408	6.7956	56.418
113.857	0.9192	2	(3 2 5)	56.928	0.5440	6.8355	56.928
114.904	0.9138	2	(4 1 1)	57.452	0.5472	6.8759	57.452
118.434	0.8966	4	(2 1 9)	59.217	0.5577	7.0078	59.217
120.099	0.889	2	(2 2 8)	60.049	0.5624	7.0677	60.049
121.72	0.8819	2	(4 1 3)	60.86	0.5670	7.1246	60.86
122.331	0.8793	2	(4 0 4)	61.165	0.5686	7.1457	61.165
131.029	0.8464	2	(4 2 0)	65.514	0.5907	7.4234	65.514
135.991	0.8308	2	(3 2 7)	67.996	0.6018	7.5628	67.996
137.384	0.8268	4	(4 1 5)	68.692	0.6047	7.5994	68.692
143.878	0.8102	2	(3 0 9)	71.939	0.6171	7.7551	71.939
150.028	0.7974	4	(4 2 4)	75.014	0.6270	7.8796	75.014
152.622	0.7928	2	(0 0 12)	76.311	0.6307	7.9253	76.311

A.2 Large-scale Atomistic Simulation of Hot Carrier Generation.

1. Details on the numerical calculation of the hot carrier generation rate.

The large-scale atomistic simulations for hot carrier generation were conducted using a two-step method, as recently proposed by Jin et al[181]. The first step involves calculating the electric field within the nanoparticle (NP), and the second step utilizes this information to determine the rate of hot carrier generation via Fermi's Golden Rule (FGR).

In the first stage, the nanoparticle is modeled as a dielectric material subjected to an external electric field. The dielectric constant, $\epsilon(\omega)$, of the nanoparticle is derived from experimental bulk gold data[260], with ω representing the frequency of the applied electric field. Within the quasistatic approximation, the electric field inside the nanoparticle is calculated by solving Laplace's equation for the electric potential. Commercial software, such as COMSOL, is employed to solve these equations, imposing boundary conditions where the external electric field is uniform at infinite distances.

As demonstrated in Figure 3 (g-i), the simulation results show the absolute electric field strength across different nanoparticle geometries, with the incident field aligned along the z-axis and tuned to the localized surface plasmon resonance (LSPR). The nanoparticle sizes were selected to include around 200,000 gold atoms, a range that satisfies the conditions for the quasistatic approximation. Notably, significant field enhancement was observed at the corners and edges of all geometries, consistent with expectations from theoretical models of nanoparticle plasmonics.

Once the electric field distribution is obtained, it serves as a perturbation that drives the system out of equilibrium. The second step involves calculating the electron-hole pair generation rate using FGR. Instead of directly computing eigenfunctions and eigenenergies, the Kernel Polynomial Method (KPM)[261] is applied, which offers computational efficiency for large systems. The electronic structure is modeled through a tight-binding Hamiltonian using a two-center Slater-Koster parametrization of bulk gold[181]. This model considers nine orbitals, including the 5d, 6s, and 6p orbitals, with spin treated as a degeneracy factor. The atomic-scale NP model is constructed by specifying the boundary planes of the facets and filling the interior with a face-centered cubic lattice. This detailed method enables accurate calculation of the hot carrier generation rate for each nanoparticle geometry.

2. Fermi's golden rule applied to hot carrier generation.

The electric potential ϕ acts as the external perturbation, exciting electrons from an initial state i with energy ϵ_i to a final state f with energy $\epsilon_f = \epsilon_i + \hbar\omega$. The rate ΓifΓif at which these transitions occur is determined using Fermi's golden rule, applying second-order perturbation theory:

$$\Gamma_{if} = \frac{2\pi}{\hbar} |\langle i|\Phi|f\rangle|^2 \, \delta(\epsilon_i - \epsilon_f + \hbar\omega) \tag{A.1}$$

The number of hot electrons generated with energy E is calculated by summing over all possible transitions to states with final energy E, from occupied states below the Fermi surface to unoccupied states above it:

$$N_e(E,\omega) = \sum_{if} \Gamma_{if} f(\epsilon_i)(1 - f(\epsilon_f))\delta(\epsilon_f - E) \tag{A.2}$$

Each electron generated with energy E produces a corresponding hole with energy $E - \hbar\omega$. Therefore, the rate of hot hole generation is given by:

$$N_h(E,\omega) = N_e(E + \hbar\omega, \omega) \tag{A.3}$$

3. Fermi's golden rule and KPM

Knowledge of the eigenstates and eigenenergies typically requires the exact diagonalization of the corresponding Hamiltonian HH, which is computationally demanding and often limits the system size to a few thousand atoms. However, methods like the Kernel Polynomial Method (KPM)[261] have gained significant traction in the last decade by circumventing these limitations[262]. KPM operates in real-space and utilizes stochastic evaluations of the trace to avoid diagonalization, offering an advantageous balance between computational efficiency and accuracy. This method has been successfully applied to hot carrier generation studies[181]. FGR can be expressed in real space as:

$$N_e(E,\omega) = \frac{2\pi}{\hbar} \int_{-\infty}^{\infty} d\epsilon \int_{-\infty}^{\infty} d\epsilon' \, \mathrm{Tr}\left[\delta(\epsilon - H)\Phi\delta(\epsilon' - H)\Phi^\dagger\right] \delta(\epsilon' - E)\delta(\epsilon' - \epsilon - \hbar\omega) \tag{A.4}$$

The Dirac delta operators are computed using an expansion in a series of Chebyshev polynomials T_n :

$$\delta(\epsilon - H) = \frac{1}{\Delta} \frac{1}{\sqrt{1 - \tilde{\epsilon}^2}} \sum_{n=0}^{M} w_n^M T_n(\tilde{\epsilon}) T_n(\tilde{H}) \tag{A.5}$$

This kind of expansion requires rescaling of the energy scales to ensure the rescaled Hamiltonian's spectrum lies within the range $]-1, 1[$. The spectrum bounds Emax and Emin are found beforehand and used to rescale ϵ and H, denoted by a tilde. w is a weight factor arising from the Kernel Polynomial Method to deal with Gibbs oscillations and guarantee uniform convergence of the series. The trace is calculated with a Stochastic Trace Evaluation (STE). Defining a random vector in the Hilbert space:

$$|\xi\rangle = \frac{1}{\sqrt{N}} \sum_{i=1}^{N} \xi_i |i\rangle \tag{A.6}$$

such that the random numbers ξ_i are uncorrelated with variance 1 ensures that, on average, the trace of any operator can be evaluated by simply calculating its expectation value with this random vector: $\mathrm{Tr}(A) = \langle\xi|A|\xi\rangle$. This process introduces an errorbar to the calculation but for large systems is considerably more efficient than evaluating the trace explicitly.

References

[1] Simone Ezendam et al. “Hybrid plasmonic nanomaterials for hydrogen generation and carbon dioxide reduction”. In: *ACS Energy Letters* 7.2 (2022), pp. 778–815 (cited on pages 5, 15, 20, 21).

[2] Stefan A Maier et al. *Plasmonics: fundamentals and applications*. Vol. 1. Springer, 2007 (cited on pages 5, 6, 8).

[3] Gustav Mie. “Beiträge zur Optik trüber Medien, speziell kolloidaler Metallösungen”. In: *Annalen der physik* 330.3 (1908), pp. 377–445 (cited on page 9).

[4] Craig F Bohren and Donald R Huffman. *Absorption and scattering of light by small particles*. John Wiley and Sons, 2008 (cited on page 10).

[5] Pedro HC Camargo and Emiliano Cortés. *Plasmonic catalysis: from fundamentals to applications*. John Wiley and Sons, 2021 (cited on page 10).

[6] JR Mejia-Salazar and Osvaldo N Oliveira Jr. “Plasmonic biosensing: Focus review”. In: *Chemical reviews* 118.20 (2018), pp. 10617–10625 (cited on page 10).

[7] Briliant Adhi Prabowo, Agnes Purwidyantri, and Kou-Chen Liu. “Surface plasmon resonance optical sensor: A review on light source technology”. In: *Biosensors* 8.3 (2018), p. 80 (cited on page 10).

[8] Kadir Aslan, Joseph R Lakowicz, and Chris D Geddes. “Plasmon light scattering in biology and medicine: new sensing approaches, visions and perspectives”. In: *Current opinion in chemical biology* 9.5 (2005), pp. 538–544 (cited on page 10).

[9] Changhui Liu et al. “Recent advances of plasmonic nanofluids in solar harvesting and energy storage”. In: *Journal of Energy Storage* 72 (2023), p. 108329 (cited on page 10).

[10] Yixin Zhao and Clemens Burda. “Development of plasmonic semiconductor nanomaterials with copper chalcogenides for a future with sustainable energy materials”. In: *Energy and Environmental Science* 5.2 (2012), pp. 5564–5576 (cited on page 10).

[11] Jiaxin Li et al. “Light-assisted metal–air batteries: progress, challenges, and perspectives”. In: *Angewandte Chemie International Edition* 61.51 (2022), e202213026 (cited on page 10).

[12] Umar Aslam, Steven Chavez, and Suljo Linic. “Controlling energy flow in multimetallic nanostructures for plasmonic catalysis”. In: *Nature nanotechnology* 12.10 (2017), pp. 1000–1005 (cited on pages 10, 14).

[13] Emiliano Cortés et al. “Challenges in plasmonic catalysis”. In: *ACS nano* 14.12 (2020), pp. 16202–16219 (cited on pages 10, 16, 20).

[14] Yueyue Dong et al. “Plasmonic catalysis: New opportunity for selective chemical bond evolution”. In: *ACS Catalysis* 13.10 (2023), pp. 6730–6743 (cited on pages 10, 14, 15).

[15] Mark L Brongersma, Naomi J Halas, and Peter Nordlander. “Plasmon-induced hot carrier science and technology”. In: *Nature nanotechnology* 10.1 (2015), pp. 25–34 (cited on page 11).

[16] Emiliano Cortés. “Efficiency and Bond Selectivity in Plasmon-Induced Photochemistry”. In: *Advanced Optical Materials* 5.15 (2017), p. 1700191 (cited on page 11).

[17] Yuchao Zhang et al. “Surface-plasmon-driven hot electron photochemistry”. In: *Chemical reviews* 118.6 (2017), pp. 2927–2954 (cited on page 12).

[18] Daniel C Ratchford. “Plasmon-induced charge transfer: Challenges and outlook”. In: *ACS nano* 13.12 (2019), pp. 13610–13614 (cited on pages 12, 13).

[19] Aaron Bayles et al. “Al@ TiO2 Core–shell nanoparticles for plasmonic photocatalysis”. In: *ACS nano* 16.4 (2022), pp. 5839–5850 (cited on page 13).

[20] Keisuke Kimura et al. “TiO2 crystal form-dependence of the Au/TiO2 plasmon photocatalyst’s activity”. In: *The Journal of Physical Chemistry C* 116.12 (2012), pp. 7111–7117 (cited on page 13).

[21] Quan Doan Mai et al. “Silver nanoparticles-based SERS platform towards detecting chloramphenicol and amoxicillin: an experimental insight into the role of HOMO–LUMO energy levels of the analyte in the SERS signal and charge transfer process”. In: *The Journal of Physical Chemistry C* 126.17 (2022), pp. 7778–7790 (cited on page 13).

[22] Emily A Sprague-Klein et al. “Modulating the electron affinity of small bipyridyl molecules on single gold nanoparticles for plasmon-driven electron transfer”. In: *The Journal of Physical Chemistry C* 125.40 (2021), pp. 22142–22153 (cited on page 13).

[23] Kaifeng Wu et al. “Efficient hot-electron transfer by a plasmon-induced interfacial charge-transfer transition”. In: *Science* 349.6248 (2015), pp. 632–635 (cited on page 13).

[24] Behnaz Ostovar et al. “The role of the plasmon in interfacial charge transfer”. In: *Science Advances* 10.27 (2024), eadp3353 (cited on page 13).

[25] Anatoly V Zayats and Igor I Smolyaninov. “Near-field photonics: surface plasmon polaritons and localized surface plasmons”. In: *Journal of Optics A: Pure and Applied Optics* 5.4 (2003), S16 (cited on page 13).

[26] Vincenzo Amendola et al. “Surface plasmon resonance in gold nanoparticles: a review”. In: *Journal of physics: Condensed matter* 29.20 (2017), p. 203002 (cited on page 13).

[27] Xiang-Tian Kong, Zhiming Wang, and Alexander O Govorov. “Plasmonic nanostars with hot spots for efficient generation of hot electrons under solar illumination”. In: *Advanced Optical Materials* 5.15 (2017) (cited on page 13).

[28] Zhenglong Zhang et al. “Plasmon-driven catalysis on molecules and nanomaterials”. In: *Accounts of chemical research* 52.9 (2019), pp. 2506–2515 (cited on page 13).

[29] Andrew J Wilson and Prashant K Jain. “Light-induced voltages in catalysis by plasmonic nanostructures”. In: *Accounts of chemical research* 53.9 (2020), pp. 1773–1781 (cited on page 13).

[30] Dana Cialla et al. “Surface-enhanced Raman spectroscopy (SERS): progress and trends”. In: *Analytical and bioanalytical chemistry* 403 (2012), pp. 27–54 (cited on page 13).

[31] Wenbo Hou and Stephen B Cronin. “A review of surface plasmon resonance-enhanced photocatalysis”. In: *Advanced Functional Materials* 23.13 (2013), pp. 1612–1619 (cited on page 14).

[32] Jon P Camden et al. “Probing the structure of single-molecule surface-enhanced Raman scattering hot spots”. In: *Journal of the American Chemical Society* 130.38 (2008), pp. 12616–12617 (cited on page 14).

[33] Joseph R Lakowicz. “Plasmonics in biology and plasmon-controlled fluorescence”. In: *Plasmonics* 1 (2006), pp. 5–33 (cited on page 14).

[34] Alexander O Govorov et al. “Theory of circular dichroism of nanomaterials comprising chiral molecules and nanocrystals: plasmon enhancement, dipole interactions, and dielectric effects”. In: *Nano letters* 10.4 (2010), pp. 1374–1382 (cited on page 14).

[35] Yonatan Dubi, Ieng Wai Un, and Yonatan Sivan. “Thermal effects–an alternative mechanism for plasmon-assisted photocatalysis”. In: *Chemical Science* 11.19 (2020), pp. 5017–5027 (cited on page 14).

[36] Minmin Gao, Peh Kang Nuo Connor, and Ghim Wei Ho. “Plasmonic photothermic directed broadband sunlight harnessing for seawater catalysis and desalination”. In: *Energy and Environmental Science* 9.10 (2016), pp. 3151–3160 (cited on page 14).

[37] Simone Ezendam et al. “Anti Stokes thermometry of plasmonic nanoparticle arrays”. In: *Advanced Optical Materials* 12.3 (2024), p. 2301496 (cited on page 14).

[38] Julian Gargiulo et al. “Impact of bimetallic interface design on heat generation in plasmonic Au/Pd nanostructures studied by single-particle thermometry”. In: *Nature Communications* 14.1 (2023), p. 3813 (cited on page 14).

[39] Huabin Zhang et al. “Surface-plasmon-enhanced photodriven CO2 reduction catalyzed by metal-organic-framework-derived iron nanoparticles encapsulated by ultrathin carbon layers”. In: *Adv. Mater* 28.19 (2016), pp. 3703–3710 (cited on page 14).

[40] Julian Gargiulo et al. “From optical to chemical hot spots in plasmonics”. In: *Accounts of chemical research* 52.9 (2019), pp. 2525–2535 (cited on page 15).

[41] Britt Hvolbæk et al. “Catalytic activity of Au nanoparticles”. In: *Nano today* 2.4 (2007), pp. 14–18 (cited on page 15).

[42] Guangfu Liao et al. “Ag-Based nanocomposites: synthesis and applications in catalysis”. In: *Nanoscale* 11.15 (2019), pp. 7062–7096 (cited on page 15).

[43] Weiting Yu, Marc D Porosoff, and Jingguang G Chen. “Review of Pt-based bimetallic catalysis: from model surfaces to supported catalysts”. In: *Chemical reviews* 112.11 (2012), pp. 5780–5817 (cited on page 15).

[44] Matias Herran et al. “Plasmonic bimetallic two-dimensional supercrystals for H2 generation”. In: *Nature Catalysis* 6.12 (2023), pp. 1205–1214 (cited on page 15).

[45] Mark W Knight et al. “Aluminum plasmonic nanoantennas”. In: *Nano letters* 12.11 (2012), pp. 6000–6004 (cited on page 15).

[46] Yan Chen et al. “Aluminum-Based Plasmonic Photocatalysis”. In: *Particle and Particle Systems Characterization* 34.8 (2017), p. 1600357 (cited on page 15).

[47] Yugang Sun and Younan Xia. “Shape-controlled synthesis of gold and silver nanoparticles”. In: *science* 298.5601 (2002), pp. 2176–2179 (cited on page 16).

[48] Tianmeng Sun et al. “Engineered nanoparticles for drug delivery in cancer therapy”. In: *Nanomaterials and Neoplasms* (2021), pp. 31–142 (cited on page 16).

[49] Xianmao Lu et al. “Chemical synthesis of novel plasmonic nanoparticles”. In: *Annual review of physical chemistry* 60 (2009), pp. 167–192 (cited on page 16).

[50] Younan Xia et al. “Shape-controlled synthesis of metal nanocrystals: simple chemistry meets complex physics?” In: *Angewandte Chemie International Edition* 48.1 (2009), pp. 60–103 (cited on pages 16, 17).

[51] Kyle D Gilroy et al. “Shape-controlled synthesis of colloidal metal nanocrystals by replicating the surface atomic structure on the seed”. In: *Advanced Materials* 30.25 (2018), p. 1706312 (cited on page 16).

[52] Younan Xia et al. “One-dimensional nanostructures: synthesis, characterization, and applications”. In: *Advanced materials* 15.5 (2003), pp. 353–389 (cited on pages 16, 17).

[53] Younan Xia et al. “Seed-mediated growth of colloidal metal nanocrystals”. In: *Angewandte Chemie International Edition* 56.1 (2017), pp. 60–95 (cited on page 16).

[54] Chi M Phan and Hoang M Nguyen. “Role of capping agent in wet synthesis of nanoparticles”. In: *The Journal of Physical Chemistry A* 121.17 (2017), pp. 3213–3219 (cited on page 17).

[55] Manjeet Singh, I Sinha, and RK Mandal. “Role of pH in the green synthesis of silver nanoparticles”. In: *Materials Letters* 63.3-4 (2009), pp. 425–427 (cited on page 17).

[56] Chih-Wei Tsai and Ernie HG Langner. “The effect of synthesis temperature on the particle size of nano-ZIF-8”. In: *Microporous and Mesoporous Materials* 221 (2016), pp. 8–13 (cited on page 17).

[57] Rebecca A French et al. “Influence of ionic strength, pH, and cation valence on aggregation kinetics of titanium dioxide nanoparticles”. In: *Environmental science and technology* 43.5 (2009), pp. 1354–1359 (cited on page 17).

[58] SH Che Man et al. “Nano-sized graphene oxide as sole surfactant in miniemulsion polymerization for nanocomposite synthesis: Effect of pH and ionic strength”. In: *Polymer* 55.16 (2014), pp. 3490–3497 (cited on page 17).

[59] Lin Hu, Ruirui Zhang, and Qianwang Chen. “Synthesis and assembly of nanomaterials under magnetic fields”. In: *Nanoscale* 6.23 (2014), pp. 14064–14105 (cited on page 17).

[60] Marek Grzelczak et al. “Shape control in gold nanoparticle synthesis”. In: *Colloidal Synthesis of Plasmonic Nanometals* (2020), pp. 197–220 (cited on page 17).

[61] Kwangjin An and Gabor A Somorjai. “Size and shape control of metal nanoparticles for reaction selectivity in catalysis”. In: *ChemCatChem* 4.10 (2012), pp. 1512–1524 (cited on page 17).

[62] CL Tien. “Thermal radiation properties of gases”. In: *Advances in heat transfer*. Vol. 5. Elsevier, 1969, pp. 253–324 (cited on page 17).

[63] NOAA Global Monitoring Laboratory. *Trends in Atmospheric Carbon Dioxide*. Accessed: 2025-01-08. 2025. URL: https://gml.noaa.gov/ccgg/trends/ (cited on pages 17, 18).

[64] Scott C Doney et al. “Ocean acidification: the other CO2 problem”. In: *Annual review of marine science* 1.1 (2009), pp. 169–192 (cited on page 17).

[65] Our World in Data. *Emissions By Fuel*. Accessed: 2025-01-08. 2025. URL: https://ourworldindata.org/emissions-by-fuel (cited on page 17).

[66] Liming Wang et al. “Surface strategies for catalytic CO 2 reduction: from two-dimensional materials to nanoclusters to single atoms”. In: *Chemical Society Reviews* 48.21 (2019), pp. 5310–5349 (cited on page 18).

[67] Xiaoxia Chang, Tuo Wang, and Jinlong Gong. “CO 2 photo-reduction: insights into CO 2 activation and reaction on surfaces of photocatalysts”. In: *Energy and Environmental Science* 9.7 (2016), pp. 2177–2196 (cited on pages 18–20).

[68] Jeffrey M Barlow and Jenny Y Yang. “Thermodynamic considerations for optimizing selective CO2 reduction by molecular catalysts”. In: *ACS central science* 5.4 (2019), pp. 580–588 (cited on page 18).

[69] Chi Chen, Juliet F Khosrowabadi Kotyk, and Stafford W Sheehan. “Progress toward commercial application of electrochemical carbon dioxide reduction”. In: *Chem* 4.11 (2018), pp. 2571–2586 (cited on page 18).

[70] Nikhil Dhabarde et al. “Review of photocatalytic and photo-electrocatalytic reduction of CO2 on carbon supported films”. In: *International Journal of Hydrogen Energy* 47.72 (2022), pp. 30908–30936 (cited on pages 18, 20).

[71] Yawen Wang et al. “Catalysts in electro-, photo-and photoelectrocatalytic CO2 reduction reactions”. In: *Journal of Photochemistry and Photobiology C: Photochemistry Reviews* 40 (2019), pp. 117–149 (cited on pages 18, 19).

[72] Stephanie Nitopi et al. “Progress and perspectives of electrochemical CO2 reduction on copper in aqueous electrolyte”. In: *Chemical reviews* 119.12 (2019), pp. 7610–7672 (cited on page 18).

[73] Qiu-Jin Wu et al. “Thermo-, electro-, and photocatalytic CO2 conversion to value-added products over porous metal/covalent organic frameworks”. In: *Accounts of Chemical Research* 55.20 (2022), pp. 2978–2997 (cited on page 19).

[74] Marianna Bellardita et al. “(Photo) electrocatalytic versus heterogeneous photocatalytic carbon dioxide reduction”. In: *ChemPhotoChem* 5.9 (2021), pp. 767–791 (cited on page 19).

[75] Andreas Wagner, Constantin D Sahm, and Erwin Reisner. “Towards molecular understanding of local chemical environment effects in electro-and photocatalytic CO2 reduction”. In: *Nature Catalysis* 3.10 (2020), pp. 775–786 (cited on page 19).

[76] Junseok Lee, Dan C Sorescu, and Xingyi Deng. “Electron-induced dissociation of CO2 on TiO2 (110)”. In: *Journal of the American Chemical Society* 133.26 (2011), pp. 10066–10069 (cited on page 19).

[77] Siyuan Fang et al. “Photocatalytic CO2 reduction”. In: *Nature Reviews Methods Primers* 3.1 (2023), p. 61 (cited on page 20).

[78] Siwei Li et al. “Recent advances in plasmonic nanostructures for enhanced photocatalysis and electrocatalysis”. In: *Advanced Materials* 33.6 (2021), p. 2000086 (cited on page 20).

[79] Youngsang Kim et al. “Surface-Plasmon-Assisted Photoelectrochemical Reduction of CO2 and NO3- on Nanostructured Silver Electrodes”. In: *Advanced Energy Materials* 8.22 (2018), p. 1800363 (cited on page 20).

[80] Erin B Creel et al. “Directing selectivity of electrochemical carbon dioxide reduction using plasmonics”. In: *ACS Energy Letters* 4.5 (2019), pp. 1098–1105 (cited on page 20).

[81] Mahmoud Sayed, Liuyang Zhang, and Jiaguo Yu. “Plasmon-induced interfacial charge-transfer transition prompts enhanced CO2 photoreduction over Cu/Cu2O octahedrons”. In: *Chemical Engineering Journal* 397 (2020), p. 125390 (cited on page 20).

[82] Elizabeth R Corson et al. “Reduction of carbon dioxide at a plasmonically active copper–silver cathode”. In: *Chemical Communications* 56.69 (2020), pp. 9970–9973 (cited on page 20).

[83] Hassan Nazir et al. “Is the H2 economy realizable in the foreseeable future? Part I: H2 production methods”. In: *International Journal of Hydrogen Energy* 45.27 (2020), pp. 13777–13788 (cited on page 21).

[84] Xiaoxin Zou and Yu Zhang. “Noble metal-free hydrogen evolution catalysts for water splitting”. In: *Chemical Society Reviews* 44.15 (2015), pp. 5148–5180 (cited on page 21).

[85] Piyali Chatterjee et al. “Photovoltaic/photo-electrocatalysis integration for green hydrogen: A review”. In: *Energy Conversion and Management* 261 (2022), p. 115648 (cited on page 22).

[86] Andrzej Lasia. “Mechanism and kinetics of the hydrogen evolution reaction”. In: *international journal of hydrogen energy* 44.36 (2019), pp. 19484–19518 (cited on page 22).

[87] Cynthia G Zoski. *Handbook of electrochemistry*. Elsevier, 2006 (cited on page 22).

[88] Yawen Wang et al. “Plasmonic metal nanostructures as efficient light absorbers for solar water splitting”. In: *Advanced Energy and Sustainability Research* 2.11 (2021), p. 2100092 (cited on page 22).

[89] Yan Wei et al. “Site-selective modification of AgPt on multibranched Au nanostars for plasmon-enhanced hydrogen evolution and methanol oxidation reaction in visible to near-infrared region”. In: *Journal of Power Sources* 425 (2019), pp. 17–26 (cited on page 23).

[90] Lili Du et al. “Plasmon-promoted electrocatalytic water splitting on metal–semiconductor nanocomposites: the interfacial charge transfer and the real catalytic sites”. In: *Chemical Science* 10.41 (2019), pp. 9605–9612 (cited on page 23).

[91] Rohul H Adnan and Aishah A Jalil. “Gold photocatalysis in sustainable hydrogen peroxide generation”. In: *Materials Today Chemistry* 27 (2023), p. 101322 (cited on page 23).

[92] Yanyan Sun, Lei Han, and Peter Strasser. “A comparative perspective of electrochemical and photochemical approaches for catalytic H 2 O 2 production”. In: *Chemical Society Reviews* 49.18 (2020), pp. 6605–6631 (cited on pages 23, 24).

[93] Yang Ding et al. “Emerging semiconductors and metal-organic-compounds-related photocatalysts for sustainable hydrogen peroxide production”. In: *Matter* 5.7 (2022), pp. 2119–2167 (cited on page 23).

[94] Zhong Chen et al. “Photocatalytic H2O2 production systems: design strategies and environmental applications”. In: *Chemical Engineering Journal* 451 (2023), p. 138489 (cited on pages 24, 25).

[95] Huilin Hou, Xiangkang Zeng, and Xiwang Zhang. “Production of hydrogen peroxide by photocatalytic processes”. In: *Angewandte Chemie International Edition* 59.40 (2020), pp. 17356–17376 (cited on page 24).

[96] Yasuhiro Shiraishi et al. “Highly selective production of hydrogen peroxide on graphitic carbon nitride (g-C3N4) photocatalyst activated by visible light”. In: *Acs Catalysis* 4.3 (2014), pp. 774–780 (cited on page 24).

[97] Yajie Zhao et al. “Efficient production of H2O2 via two-channel pathway over ZIF-8/C3N4 composite photocatalyst without any sacrificial agent”. In: *Applied Catalysis B: Environmental* 278 (2020), p. 119289 (cited on page 24).

[98] Miwako Teranishi, Shin-ichi Naya, and Hiroaki Tada. “In situ liquid phase synthesis of hydrogen peroxide from molecular oxygen using gold nanoparticle-loaded titanium (IV) dioxide photocatalyst”. In: *Journal of the American Chemical Society* 132.23 (2010), pp. 7850–7851 (cited on page 24).

[99] Daijiro Tsukamoto et al. “Photocatalytic H2O2 production from ethanol/O2 system using TiO2 loaded with Au–Ag bimetallic alloy nanoparticles”. In: *ACS catalysis* 2.4 (2012), pp. 599–603 (cited on page 25).

[100] Xianqiang Xiong et al. “Sustained production of H 2 O 2 in alkaline water solution using borate and phosphate-modified Au/TiC 2 photocatalysts”. In: *Photochemical and Photobiological Sciences* 17 (2018), pp. 1018–1022 (cited on page 25).

[101] Our World in Data. *Plastic Pollution*. Accessed: 2025-01-08. 2025. URL: https://ourworldindata.org/plastic-pollution (cited on pages 25–27).

[102] Tanveer M Adyel. “Accumulation of plastic waste during COVID-19”. In: *Science* 369.6509 (2020), pp. 1314–1315 (cited on page 25).

[103] Wenjie Tian et al. “Microplastic materials in the environment: Problem and strategical solutions”. In: *Progress in Materials Science* 132 (2023), p. 101035 (cited on page 25).

[104] Taylor Uekert, Hatice Kasap, and Erwin Reisner. “Photoreforming of nonrecyclable plastic waste over a carbon nitride/nickel phosphide catalyst”. In: *Journal of the American Chemical Society* 141.38 (2019), pp. 15201–15210 (cited on pages 25, 26).

[105] Ellen MacArthur. “The new plastics economy: Rethinking the future of plastics and catalysing action”. In: *Ellen MacArthur Foundation: Cowes, UK* 68 (2017) (cited on page 25).

[106] Elaine Barnard, Jose Jonathan Rubio Arias, and Wim Thielemans. “Chemolytic depolymerisation of PET: a review”. In: *Green Chemistry* 23.11 (2021), pp. 3765–3789 (cited on page 25).

[107] Tomoji Kawai and Tadayoshi Sakata. “Photocatalytic hydrogen production from water by the decomposition of poly-vinylchloride, protein, algae, dead insects, and excrement”. In: *Chemistry Letters* 10.1 (1981), pp. 81–84 (cited on page 26).

[108] Xingchen Jiao et al. “Photocatalytic conversion of waste plastics into C2 fuels under simulated natural environment conditions”. In: *Angewandte Chemie International Edition* 59.36 (2020), pp. 15497–15501 (cited on page 26).

[109] Tengfei Li et al. “Bridging plastic recycling and organic catalysis: photocatalytic deconstruction of polystyrene via a C–H oxidation pathway”. In: *ACS catalysis* 12.14 (2022), pp. 8155–8163 (cited on pages 26, 27).

[110] Taylor Uekert et al. “Plastic waste as a feedstock for solar-driven H 2 generation”. In: *Energy and Environmental Science* 11.10 (2018), pp. 2853–2857 (cited on page 26).

[111] Shafeer Kalathil, Melanie Miller, and Erwin Reisner. “Microbial fermentation of polyethylene terephthalate (PET) plastic waste for the production of chemicals or electricity”. In: *Angewandte Chemie International Edition* 61.45 (2022), e202211057 (cited on page 27).

[112] Nasir Uddin et al. “Ultrabroadband plasmon driving selective photoreforming of methanol under ambient conditions”. In: *Proceedings of the National Academy of Sciences* 120.3 (2023), e2212075120 (cited on page 28).

[113] Ting-Ting Zhao et al. “A comparative investigation of electrocatalysis at Pt monolayers on shape-controlled Au nanocrystals: facet effect versus strain effect”. In: *Journal of Materials Chemistry A* 4.41 (2016), pp. 15845–15850 (cited on pages 29, 30, 37).

[114] Yue Yu et al. “Guiding principles in the galvanic replacement reaction of an underpotentially deposited metal layer for site-selective deposition and shape and size control of satellite nanocrystals”. In: *Chemistry of Materials* 25.23 (2013), pp. 4746–4756. ISSN: 0897-4756 (cited on pages 29, 37).

[115] Yicui Kang et al. “Effect of crystal facets in plasmonic catalysis”. In: *Nature Communications* 15.1 (2024). (Max), p. 3923. ISSN: 2041-1723 (cited on pages 30, 35, 64, 66, 71, 85).

[116] Tian-Ming Chen et al. “Synthesis of Au@ TiO 2 core–shell nanoparticles with tunable structures for plasmon-enhanced photocatalysis”. In: *Nanoscale Advances* 1.11 (2019), pp. 4522–4528 (cited on pages 30, 66).

[117] Jingkai Lin et al. “Tandem microplastic degradation and hydrogen production by hierarchical carbon nitride-supported single-atom iron catalysts”. In: *Nature Communications* 15.1 (2024), p. 8769 (cited on pages 31, 83–85).

[118] James Barber. “Photosynthetic energy conversion: natural and artificial”. In: *Chemical Society Reviews* 38.1 (2009), pp. 185–196 (cited on page 35).

[119] Yoshio Hori et al. “Electrocatalytic process of CO selectivity in electrochemical reduction of CO2 at metal electrodes in aqueous media”. In: *Electrochimica Acta* 39.11-12 (1994), pp. 1833–1839. ISSN: 0013-4686 (cited on page 35).

[120] Fuping Pan and Yang Yang. “Designing CO 2 reduction electrode materials by morphology and interface engineering”. In: *Energy and Environmental Science* 13.8 (2020), pp. 2275–2309 (cited on page 35).

[121] Jing Li et al. “Thermally Evaporated Ag–Au Bimetallic Catalysts for Efficient Electrochemical CO2 Reduction”. In: *Particle and Particle Systems Characterization* 38.11 (2021), p. 2100148. ISSN: 0934-0866 (cited on page 35).

[122] Saioa Cobo et al. “A Janus cobalt-based catalytic material for electro-splitting of water”. In: *Nature materials* 11.9 (2012), pp. 802–807. ISSN: 1476-1122 (cited on page 35).

[123] Suljo Linic, Phillip Christopher, and David B Ingram. “Plasmonic-metal nanostructures for efficient conversion of solar to chemical energy”. In: *Nature materials* 10.12 (2011), pp. 911–921. ISSN: 1476-1122 (cited on page 35).

[124] Umar Aslam et al. “Catalytic conversion of solar to chemical energy on plasmonic metal nanostructures”. In: *Nature Catalysis* 1.9 (2018), pp. 656–665. ISSN: 2520-1158 (cited on pages 35, 36).

[125] Junwei Fu et al. “Activation of CO2 on graphitic carbon nitride supported single-atom cobalt sites”. In: *Chemical Engineering Journal* 415 (2021), p. 128982. ISSN: 1385-8947 (cited on page 35).

[126] Li Zhu et al. “Tuning the intermediate reaction barriers by a CuPd catalyst to improve the selectivity of CO2 electroreduction to C2 products”. In: *Chinese journal of catalysis* 42.9 (2021), pp. 1500–1508. ISSN: 1872-2067 (cited on page 35).

[127] Nenad M Marković et al. “Hydrogen electrochemistry on platinum low-index single-crystal surfaces in alkaline solution”. In: *Journal of the Chemical Society, Faraday Transactions* 92.20 (1996), pp. 3719–3725. ISSN: 1364-5455 (cited on page 35).

[128] Phil De Luna et al. “Catalyst electro-redeposition controls morphology and oxidation state for selective carbon dioxide reduction”. In: *Nature Catalysis* 1.2 (2018), pp. 103–110. ISSN: 2520-1158 (cited on page 35).

[129] Seunghoon Lee et al. “Core–shell nanoparticle clusters enable synergistic integration of plasmonic and catalytic functions in a single platform”. In: *Small* 13.43 (2017), p. 1701633. ISSN: 1613-6810 (cited on page 35).

[130] Clemens Burda et al. “Chemistry and properties of nanocrystals of different shapes”. In: *Chemical reviews* 105.4 (2005), pp. 1025–1102. ISSN: 0009-2665 (cited on page 35).

[131] Kebin Zhou and Yadong Li. “Catalysis based on nanocrystals with well-defined facets”. In: *Angewandte Chemie International Edition* 51.3 (2012), pp. 602–613. ISSN: 1433-7851 (cited on page 35).

[132] Cui Wang et al. “Facet-dependent long-term stability of gold aerogels toward ethylene glycol oxidation reaction”. In: *ACS applied materials and interfaces* 12.35 (2020), pp. 39033–39042. ISSN: 1944-8244 (cited on page 35).

[133] Bon Seung Goo et al. “Surface engineering of palladium nanocrystals: Decoupling the activity of different surface sites on nanocrystal catalysts”. In: *Angewandte Chemie* 134.23 (2022), e202202923. ISSN: 0044-8249 (cited on page 35).

[134] Naoto Todoroki et al. “Surface atomic arrangement dependence of electrochemical CO2 reduction on gold: online electrochemical mass spectrometric study on low-index Au (hkl) surfaces”. In: *ACS Catalysis* 9.2 (2019), pp. 1383–1388. ISSN: 2155-5435 (cited on pages 35, 36, 41).

[135] Ezra L Clark et al. “Influence of Atomic Surface Structure on the Activity of Ag for the Electrochemical Reduction of CO2 to CO”. In: *ACS catalysis* 9.5 (2019), pp. 4006–4014. ISSN: 2155-5435 (cited on page 36).

[136] Min Liu et al. “Enhanced electrocatalytic CO2 reduction via field-induced reagent concentration”. In: *Nature* 537.7620 (2016), pp. 382–386. ISSN: 0028-0836 (cited on page 36).

[137] Stefano Dal Forno, Luigi Ranno, and Johannes Lischner. “Material, size, and environment dependence of plasmon-induced hot carriers in metallic nanoparticles”. In: *The Journal of Physical Chemistry C* 122.15 (2018), pp. 8517–8527. ISSN: 1932-7447 (cited on page 36).

[138] Guigao Liu et al. “Crystal-facet-dependent hot-electron transfer in plasmonic-Au/semiconductor heterostructures for efficient solar photocatalysis”. In: *Journal of materials chemistry C* 3.29 (2015), pp. 7538–7542 (cited on page 36).

[139] Marco Bernardi et al. “Theory and computation of hot carriers generated by surface plasmon polaritons in noble metals”. In: *Nature communications* 6.1 (2015), p. 7044. ISSN: 2041-1723 (cited on page 36).

[140] Qingfeng Zhang and Hui Wang. “Facet-dependent catalytic activities of Au nanoparticles enclosed by high-index facets”. In: *ACS Catalysis* 4.11 (2014), pp. 4027–4033. ISSN: 2155-5435 (cited on page 36).

[141] Phillip Christopher and Suljo Linic. “Shape-and size-specific chemistry of Ag nanostructures in catalytic ethylene epoxidation”. In: *ChemCatChem* 2.1 (2010), pp. 78–83. ISSN: 1867-3880 (cited on page 36).

[142] Chun-Ya Chiu et al. “Facet-dependent catalytic activity of gold nanocubes, octahedra, and rhombic dodecahedra toward 4-nitroaniline reduction”. In: *The Journal of Physical Chemistry C* 116.44 (2012), pp. 23757–23763. ISSN: 1932-7447 (cited on page 36).

[143] Oluwasegun J Wahab et al. “Screening Surface Structure–Electrochemical Activity Relationships of Copper Electrodes under CO2 Electroreduction Conditions”. In: *ACS catalysis* 12.11 (2022), pp. 6578–6588. ISSN: 2155-5435 (cited on page 36).

[144] Nagahiro Hoshi, Takeshi Mizumura, and Yoshio Hori. “Significant difference of the reduction rates of carbon dioxide between Pt (111) and Pt (110) single crystal electrodes”. In: *Electrochimica acta* 40.7 (1995), pp. 883–887. ISSN: 0013-4686 (cited on page 36).

[145] Ming Zhao et al. “Ru octahedral nanocrystals with a face-centered cubic structure,111 facets, thermal stability up to 400 C, and enhanced catalytic activity”. In: *Journal of the American Chemical Society* 141.17 (2019), pp. 7028–7036. ISSN: 0002-7863 (cited on page 36).

[146] Na Tian et al. “Synthesis of tetrahexahedral platinum nanocrystals with high-index facets and high electro-oxidation activity”. In: *science* 316.5825 (2007), pp. 732–735. ISSN: 0036-8075 (cited on page 36).

[147] Anna Klinkova et al. “Rational design of efficient palladium catalysts for electroreduction of carbon dioxide to formate”. In: *Acs Catalysis* 6.12 (2016), pp. 8115–8120. ISSN: 2155-5435 (cited on page 36).

[148] Nagahiro Hoshi et al. “Structural effect on the rate of CO2 reduction on single crystal electrodes of palladium”. In: *Journal of Electroanalytical Chemistry* 421.1-2 (1997), pp. 15–18. ISSN: 1572-6657 (cited on page 36).

[149] Kun Jiang et al. “Metal ion cycling of Cu foil for selective C–C coupling in electrochemical CO2 reduction”. In: *Nature Catalysis* 1.2 (2018), pp. 111–119. ISSN: 2520-1158 (cited on page 36).

[150] Federico Calle-Vallejo and Marc TM Koper. “Theoretical considerations on the electroreduction of CO to C2 species on Cu (100) electrodes”. In: *Angewandte Chemie* 125.28 (2013), pp. 7423–7426. ISSN: 0044-8249 (cited on page 36).

[151] Gian Luca De Gregorio et al. “Facet-dependent selectivity of Cu catalysts in electrochemical CO2 reduction at commercially viable current densities”. In: *ACS catalysis* 10.9 (2020), pp. 4854–4862. ISSN: 2155-5435 (cited on page 36).

[152] Pranit Iyengar et al. “Elucidating the facet-dependent selectivity for CO2 electroreduction to ethanol of Cu–Ag tandem catalysts”. In: *Acs Catalysis* 11.8 (2021), pp. 4456–4463. ISSN: 2155-5435 (cited on page 36).

[153] Nagahiro Hoshi, Makiko Kato, and Yoshio Hori. “Electrochemical reduction of CO2 on single crystal electrodes of silver Ag (111), Ag (100) and Ag (110)”. In: *Journal of electroanalytical chemistry* 440.1-2 (1997), pp. 283–286. ISSN: 1572-6657 (cited on page 36).

[154] Rui Lin et al. “Quantitative study of charge carrier dynamics in well-defined WO3 nanowires and nanosheets: insight into the crystal facet effect in photocatalysis”. In: *Journal of the American Chemical Society* 140.29 (2018), pp. 9078–9082. ISSN: 0002-7863 (cited on page 36).

[155] Donge Wang et al. “Crystal facet dependence of water oxidation on BiVO4 sheets under visible light irradiation”. In: *Chemistry–A European Journal* 17.4 (2011), pp. 1275–1282. ISSN: 0947-6539 (cited on page 36).

[156] Yang Li et al. “Facet-selective charge carrier transport, deactivation mechanism and stabilization of a Cu 2 O photo-electro-catalyst”. In: *Physical Chemistry Chemical Physics* 18.10 (2016), pp. 7023–7026 (cited on page 36).

[157] Ting-Ting Zhao et al. “A comparative investigation of electrocatalysis at Pt monolayers on shape-controlled Au nanocrystals: facet effect versus strain effect”. In: *Journal of Materials Chemistry A* 4.41 (2016), pp. 15845–15850 (cited on page 36).

[158] Yue Yu et al. “Guiding principles in the galvanic replacement reaction of an underpotentially deposited metal layer for site-selective deposition and shape and size control of satellite nanocrystals”. In: *Chemistry of Materials* 25.23 (2013), pp. 4746–4756. ISSN: 0897-4756 (cited on pages 36, 48).

[159] Suljo Linic, Phillip Christopher, and David B Ingram. “Plasmonic-metal nanostructures for efficient conversion of solar to chemical energy”. In: *Nature materials* 10.12 (2011), pp. 911–921. ISSN: 1476-1122 (cited on page 36).

[160] Andiappan Marimuthu, Jianwen Zhang, and Suljo Linic. “Tuning selectivity in propylene epoxidation by plasmon mediated photo-switching of Cu oxidation state”. In: *Science* 339.6127 (2013), pp. 1590–1593. ISSN: 0036-8075 (cited on page 36).

[161] Andrei Stefancu et al. “Interface-Dependent Selectivity in Plasmon-Driven Chemical Reactions”. In: *ACS nano* 17.3 (2023), pp. 3119–3127. ISSN: 1936-0851 (cited on page 36).

[162] Julian Gargiulo et al. “From optical to chemical hot spots in plasmonics”. In: *Accounts of chemical research* 52.9 (2019), pp. 2525–2535. ISSN: 0001-4842 (cited on pages 36, 48).

[163] Emiliano Cortés et al. “Optical metasurfaces for energy conversion”. In: *Chemical Reviews* 122.19 (2022), pp. 15082–15176. ISSN: 0009-2665 (cited on page 36).

[164] Shaunak Mukherjee et al. “Hot electrons do the impossible: plasmon-induced dissociation of H2 on Au”. In: *Nano letters* 13.1 (2013), pp. 240–247. ISSN: 1530-6984 (cited on page 36).

[165] Shaunak Mukherjee et al. “Hot-electron-induced dissociation of H2 on gold nanoparticles supported on SiO2”. In: *Journal of the American Chemical Society* 136.1 (2014), pp. 64–67. ISSN: 0002-7863 (cited on page 36).

[166] Jun Guo et al. “Boosting hot electrons in hetero-superstructures for plasmon-enhanced catalysis”. In: *Journal of the American Chemical Society* 139.49 (2017), pp. 17964–17972. ISSN: 0002-7863 (cited on page 36).

[167] Canyu Hu et al. “Surface plasmon enabling nitrogen fixation in pure water through a dissociative mechanism under mild conditions”. In: *Journal of the American Chemical Society* 141.19 (2019), pp. 7807–7814. ISSN: 0002-7863 (cited on page 36).

[168] Xia Guo et al. “Plasmon-enhanced electrocatalytic hydrogen/oxygen evolution by Pt/Fe–Au nanorods”. In: *Journal of Materials Chemistry A* 6.17 (2018), pp. 7364–7369 (cited on page 36).

[169] Weiwei Lu et al. “Photoelectrocatalytic reduction of CO2 for efficient methanol production: Au nanoparticles as electrocatalysts and light supports”. In: *Industrial and Engineering Chemistry Research* 59.10 (2020), pp. 4348–4357 (cited on page 36).

[170] Simone Ezendam et al. “Hybrid plasmonic nanomaterials for hydrogen generation and carbon dioxide reduction”. In: *ACS Energy Letters* 7.2 (2022), pp. 778–815. ISSN: 2380-8195 (cited on page 36).

[171] Rachel Nixon, Enrique Contreras, and Prashant K Jain. “Electrochemistry with plasmons”. In: *Trends in Chemistry* (2023). ISSN: 2589-7209 (cited on page 36).

[172] Lin Nan et al. “Investigating Plasmonic Catalysis Kinetics on Hot-Spot Engineered Nanoantennae”. In: *Nano Letters* 23.7 (2023), pp. 2883–2889. ISSN: 1530-6984 (cited on page 36).

[173] Emiliano Cortés. *Light-activated catalysts point the way to sustainable chemistry*. Generic. 2023 (cited on page 36).

[174] Mark L Brongersma, Naomi J Halas, and Peter Nordlander. “Plasmon-induced hot carrier science and technology”. In: *Nature nanotechnology* 10.1 (2015), pp. 25–34. ISSN: 1748-3387 (cited on page 44).

[175] Jacob B Khurgin. “How to deal with the loss in plasmonics and metamaterials”. In: *Nature nanotechnology* 10.1 (2015), pp. 2–6. ISSN: 1748-3387 (cited on page 44).

[176] LD Landau. “61–On the vibrations of the electronic plasma”. In: *The Collected Papers of LD Landau* (1965), pp. 445–460 (cited on page 44).

[177] Simone Ezendam et al. “Anti Stokes Thermometry of Plasmonic Nanoparticle Arrays”. In: *Advanced Optical Materials* (2023), p. 2301496. ISSN: 2195-1071 (cited on page 46).

[178] Erin B Creel et al. “Directing selectivity of electrochemical carbon dioxide reduction using plasmonics”. In: *ACS Energy Letters* 4.5 (2019), pp. 1098–1105. ISSN: 2380-8195 (cited on page 47).

[179] Elizabeth R Corson et al. “A temperature-controlled photoelectrochemical cell for quantitative product analysis”. In: *Review of Scientific Instruments* 89.5 (2018), p. 055112. ISSN: 0034-6748 (cited on page 47).

[180] Lin Yuan et al. “Morphology-dependent reactivity of a plasmonic photocatalyst”. In: *ACS nano* 14.9 (2020), pp. 12054–12063. ISSN: 1936-0851 (cited on page 47).

[181] Dimitris A Papaconstantopoulos. *Handbook of the band structure of elemental solids*. Springer, 1986. ISBN: 0306423383 (cited on pages 47, 95, 96).

[182] Katherine Sytwu et al. "Driving energetically unfavorable dehydrogenation dynamics with plasmonics". In: *Science* 371.6526 (2021), pp. 280–283. ISSN: 0036-8075 (cited on page 48).

[183] Tuomas P Rossi, Paul Erhart, and Mikael Kuisma. "Hot-carrier generation in plasmonic nanoparticles: the importance of atomic structure". In: *ACS nano* 14.8 (2020), pp. 9963–9971. ISSN: 1936-0851 (cited on page 49).

[184] Wenlei Zhu et al. "Active and selective conversion of CO2 to CO on ultrathin Au nanowires". In: *Journal of the American Chemical Society* 136.46 (2014), pp. 16132–16135. ISSN: 0002-7863 (cited on pages 49, 55).

[185] Wenlei Zhu et al. "Monodisperse Au nanoparticles for selective electrocatalytic reduction of CO2 to CO". In: *Journal of the American Chemical Society* 135.45 (2013), pp. 16833–16836. ISSN: 0002-7863 (cited on pages 49, 55).

[186] Katherine Sytwu et al. "Visualizing facet-dependent hydrogenation dynamics in individual palladium nanoparticles". In: *Nano Letters* 18.9 (2018), pp. 5357–5363. ISSN: 1530-6984 (cited on page 49).

[187] Carice Chong et al. "Catalyst-on-hotspot nanoarchitecture: plasmonic focusing of light onto Co-photocatalyst for efficient light-to-chemical transformation". In: *Small* (2024), p. 2309983 (cited on page 55).

[188] Damien Voiry et al. *Best practices for reporting electrocatalytic performance of nanomaterials*. 2018 (cited on page 59).

[189] Andrew J Wilson, Varun Mohan, and Prashant K Jain. "Mechanistic understanding of plasmon-enhanced electrochemistry". In: *The Journal of Physical Chemistry C* 123.48 (2019), pp. 29360–29369. ISSN: 1932-7447 (cited on page 60).

[190] Georg Kresse and Jürgen Furthmüller. "Efficient iterative schemes for ab initio total-energy calculations using a plane-wave basis set". In: *Physical review B* 54.16 (1996), p. 11169 (cited on page 60).

[191] Georg Kresse and Daniel Joubert. "From ultrasoft pseudopotentials to the projector augmented-wave method". In: *Physical review b* 59.3 (1999), p. 1758 (cited on page 60).

[192] John P Perdew, Kieron Burke, and Matthias Ernzerhof. "Generalized gradient approximation made simple". In: *Physical review letters* 77.18 (1996), p. 3865 (cited on page 60).

[193] John P Perdew and Yue Wang. "Accurate and simple analytic representation of the electron-gas correlation energy". In: *Physical review B* 45.23 (1992), p. 13244 (cited on page 60).

[194] Kang Liu et al. "Single-atom transition metals supported on black phosphorene for electrochemical nitrogen reduction". In: *Nanoscale* 12.8 (2020), pp. 4903–4908 (cited on page 60).

[195] André Torres-Pinto et al. "Recent strategies for hydrogen peroxide production by metal-free carbon nitride photocatalysts". In: *Catalysts* 9.12 (2019), p. 990. ISSN: 2073-4344 (cited on page 63).

[196] Yanyan Sun, Lei Han, and Peter Strasser. "A comparative perspective of electrochemical and photochemical approaches for catalytic H 2 O 2 production". In: *Chemical Society Reviews* 49.18 (2020), pp. 6605–6631 (cited on page 63).

[197] Samira Siahrostami et al. "Enabling direct H2O2 production through rational electrocatalyst design". In: *Nature materials* 12.12 (2013), pp. 1137–1143. ISSN: 1476-1122 (cited on page 63).

[198] Alexander T Murray et al. “Electrosynthesis of hydrogen peroxide by phase-transfer catalysis”. In: *Joule* 3.12 (2019), pp. 2942–2954. ISSN: 2542-4785 (cited on page 63).

[199] Yang Ding et al. “Emerging semiconductors and metal-organic-compounds-related photocatalysts for sustainable hydrogen peroxide production”. In: *Matter* 5.7 (2022), pp. 2119–2167. ISSN: 2590-2393 (cited on page 63).

[200] Liang Zhou et al. “Ultrathin g-C3N4 nanosheet with hierarchical pores and desirable energy band for highly efficient H2O2 production”. In: *Applied Catalysis B: Environmental* 267 (2020), p. 118396. ISSN: 0926-3373 (cited on page 63).

[201] Zedong Zhu et al. “Visible light-driven photocatalytically active g-C3N4 material for enhanced generation of H2O2”. In: *Applied Catalysis B: Environmental* 232 (2018), pp. 19–25. ISSN: 0926-3373 (cited on page 63).

[202] Xiaoyu Chang et al. “Enhancing light-driven production of hydrogen peroxide by anchoring Au onto C3N4 catalysts”. In: *Catalysts* 8.4 (2018), p. 147. ISSN: 2073-4344 (cited on page 63).

[203] Xiwei Wang et al. “Synthesis of full-spectrum-response Cu2 (OH) PO4/g-C3N4 photocatalyst with outstanding photocatalytic H2O2 production performance via a “two channel route””. In: *ACS Sustainable Chemistry and Engineering* 6.11 (2018), pp. 14542–14553. ISSN: 2168-0485 (cited on page 63).

[204] Niv Kaynan et al. “Sustainable photocatalytic production of hydrogen peroxide from water and molecular oxygen”. In: *Journal of Materials Chemistry A* 2.34 (2014), pp. 13822–13826 (cited on pages 63, 64).

[205] Guifu Zuo et al. “Efficient photocatalytic hydrogen peroxide production over TiO2 passivated by SnO2”. In: *Catalysts* 9.7 (2019), p. 623. ISSN: 2073-4344 (cited on pages 63, 72).

[206] Chunhong Xia et al. “Spatial Specific Janus S-Scheme Photocatalyst with Enhanced H2O2 Production Performance”. In: *Small* 19.29 (2023), p. 2300292. ISSN: 1613-6810 (cited on pages 63, 72).

[207] Daijiro Tsukamoto et al. “Photocatalytic H2O2 production from ethanol/O2 system using TiO2 loaded with Au–Ag bimetallic alloy nanoparticles”. In: *ACS catalysis* 2.4 (2012), pp. 599–603. ISSN: 2155-5435 (cited on pages 63, 72).

[208] Miwako Teranishi et al. “Gold-nanoparticle-loaded carbonate-modified titanium (IV) oxide surface: visible-light-driven formation of hydrogen peroxide from oxygen”. In: *Angewandte Chemie* 128.41 (2016), pp. 12965–12969. ISSN: 0044-8249 (cited on pages 63, 64, 72).

[209] Bowen He et al. “Cooperative coupling of H2O2 production and organic synthesis over a floatable polystyrene-sphere-supported TiO2/Bi2O3 S-Scheme photocatalyst”. In: *Advanced Materials* 34.38 (2022), p. 2203225. ISSN: 0935-9648 (cited on pages 63, 72).

[210] Miwako Teranishi, Shin-ichi Naya, and Hiroaki Tada. “In situ liquid phase synthesis of hydrogen peroxide from molecular oxygen using gold nanoparticle-loaded titanium (IV) dioxide photocatalyst”. In: *Journal of the American Chemical Society* 132.23 (2010), pp. 7850–7851. ISSN: 0002-7863 (cited on pages 63, 72).

[211] Kihyeun Kim et al. “Solid-phase photocatalysts: physical vapor deposition of Au nanoislands on porous TiO2 films for millimolar H2O2 production within a few minutes”. In: *ACS Catalysis* 9.10 (2019), pp. 9206–9211. ISSN: 2155-5435 (cited on pages 63, 64).

[212] Yusuke Isaka et al. “Two-phase system utilizing hydrophobic metal–organic frameworks (MOFs) for photocatalytic synthesis of hydrogen peroxide”. In: *Angewandte Chemie* 131.16 (2019), pp. 5456–5460. ISSN: 0044-8249 (cited on page 63).

[213] Yudai Kawase et al. “Ti cluster-alkylated hydrophobic MOFs for photocatalytic production of hydrogen peroxide in two-phase systems”. In: *Chemical Communications* 55.47 (2019), pp. 6743–6746 (cited on page 63).

[214] Liang Chen et al. “Acetylene and diacetylene functionalized covalent triazine frameworks as metal-free photocatalysts for hydrogen peroxide production: a new two-electron water oxidation pathway”. In: *Advanced Materials* 32.2 (2020), p. 1904433. ISSN: 0935-9648 (cited on page 63).

[215] Wei Li et al. “Core–shell structured titanium dioxide nanomaterials for solar energy utilization”. In: *Chemical Society Reviews* 47.22 (2018), pp. 8203–8237 (cited on page 64).

[216] Kenta Awa et al. “A three-component plasmonic photocatalyst consisting of gold nanoparticle and TiO2–SnO2 nanohybrid with heteroepitaxial junction: hydrogen peroxide synthesis”. In: *The Journal of Physical Chemistry C* 124.14 (2020), pp. 7797–7802. ISSN: 1932-7447 (cited on pages 64, 72).

[217] Suljo Linic, Steven Chavez, and Rachel Elias. “Flow and extraction of energy and charge carriers in hybrid plasmonic nanostructures”. In: *Nature Materials* 20.7 (2021), pp. 916–924. ISSN: 1476-1122 (cited on page 64).

[218] Fanglin Che et al. “Elucidating the roles of electric fields in catalysis: a perspective”. In: *ACS Catalysis* 8.6 (2018), pp. 5153–5174. ISSN: 2155-5435 (cited on page 64).

[219] Gianfranco Pacchioni, Julian R Lomas, and Francesc Illas. “Electric field effects in heterogeneous catalysis”. In: *Journal of Molecular Catalysis A: Chemical* 119.1-3 (1997), pp. 263–273. ISSN: 1381-1169 (cited on page 64).

[220] Zhihao Sun et al. “Experimental study on electrohydrodynamic flows of a dielectric liquid in a needle-plate configuration under direct/alternating current electric field”. In: *Journal of Electrostatics* 106 (2020), p. 103454. ISSN: 0304-3886 (cited on page 64).

[221] Min Liu et al. “Enhanced electrocatalytic CO2 reduction via field-induced reagent concentration”. In: *Nature* 537.7620 (2016), pp. 382–386. ISSN: 0028-0836 (cited on page 64).

[222] Chao Cai et al. “Heteroatoms induce localization of the electric field and promote a wide potential-window selectivity towards CO in the CO2 electroreduction”. In: *Angewandte Chemie International Edition* 61.44 (2022), e202212640. ISSN: 1433-7851 (cited on page 64).

[223] Qin Chen et al. “Ordered Ag nanoneedle arrays with enhanced electrocatalytic CO2 reduction via structure-induced inhibition of hydrogen evolution”. In: *Nano Letters* 22.15 (2022), pp. 6276–6284. ISSN: 1530-6984 (cited on page 64).

[224] Yajiao Zhou et al. “Porous Zn Conformal Coating on Dendritic-Like Ag with Enhanced Selectivity and Stability for CO2 Electroreduction to CO”. In: *Advanced Sustainable Systems* 7.1 (2023), p. 2200374. ISSN: 2366-7486 (cited on page 64).

[225] Zhi-Qiang Zhao et al. “Light Field-Enhanced Single-Site Cu Electrocatalyst for Nitrogen Fixation”. In: *Small* 19.10 (2023), p. 2206626. ISSN: 1613-6810 (cited on page 64).

[226] Peng Liu et al. “Tip-enhanced electric field: a new mechanism promoting mass transfer in oxygen evolution reactions”. In: *Advanced Materials* 33.9 (2021), p. 2007377. ISSN: 0935-9648 (cited on page 64).

[227] Shu Jiang, Chengzhou Zhu, and Shaojun Dong. “Cobalt and nitrogen-cofunctionalized graphene as a durable non-precious metal catalyst with enhanced ORR activity”. In: *Journal of Materials Chemistry A* 1.11 (2013), pp. 3593–3599 (cited on page 64).

[228] Teng Zhang et al. “Adsorption and catalytic activation of O2 molecule on the surface of Au-doped graphene under an external electric field”. In: *The Journal of Physical Chemistry C* 116.37 (2012), pp. 19918–19924. ISSN: 1932-7447 (cited on page 64).

[229] Yixuan Wang and Perla B Balbuena. “Roles of proton and electric field in the electroreduction of O2 on Pt (111) surfaces: Results of an ab-initio molecular dynamics study”. In: *The Journal of Physical Chemistry B* 108.14 (2004), pp. 4376–4384. ISSN: 1520-6106 (cited on page 64).

[230] Zhansheng Lu et al. “Tuning the activation of O2 on Pt single-atom catalyst using external-electric field: A first-principles study”. In: *Physica B: Condensed Matter* 638 (2022), p. 413934. ISSN: 0921-4526 (cited on page 64).

[231] Andiappan Marimuthu, Jianwen Zhang, and Suljo Linic. “Tuning selectivity in propylene epoxidation by plasmon mediated photo-switching of Cu oxidation state”. In: *Science* 339.6127 (2013), pp. 1590–1593. ISSN: 0036-8075 (cited on page 64).

[232] Fatemeh Kiani et al. “Transport and interfacial injection of d-band hot holes control plasmonic chemistry”. In: *ACS Energy Letters* 8.10 (2023), pp. 4242–4250. ISSN: 2380-8195 (cited on page 64).

[233] Calvin Boerigter et al. “Evidence and implications of direct charge excitation as the dominant mechanism in plasmon-mediated photocatalysis”. In: *Nature communications* 7.1 (2016), p. 10545. ISSN: 2041-1723 (cited on page 64).

[234] Li Zhu et al. “Tuning the intermediate reaction barriers by a CuPd catalyst to improve the selectivity of CO2 electroreduction to C2 products”. In: *Chinese journal of catalysis* 42.9 (2021), pp. 1500–1508. ISSN: 1872-2067 (cited on page 64).

[235] Tianfu Guan et al. “Decoding the Self-Assembly Plasmonic Interface Structure in a PbS Colloidal Quantum Dot Solid for a Photodetector”. In: *ACS nano* 17.22 (2023), pp. 23010–23019. ISSN: 1936-0851 (cited on page 64).

[236] Dachao Hong et al. “Plasmonic Ag@ TiO2 core–shell nanoparticles for enhanced CO2 photoconversion to CH4”. In: *ACS Sustainable Chemistry and Engineering* 7.23 (2019), pp. 18955–18964. ISSN: 2168-0485 (cited on page 64).

[237] Sergey Chenakin and Norbert Kruse. “Combining XPS and ToF-SIMS for assessing the CO oxidation activity of Au/TiO2 catalysts”. In: *Journal of catalysis* 358 (2018), pp. 224–236. ISSN: 0021-9517 (cited on page 67).

[238] MP Casaletto et al. “XPS study of supported gold catalysts: the role of Au0 and Au+ δ species as active sites”. In: *Surface and Interface Analysis: An International Journal devoted to the development and application of techniques for the analysis of surfaces, interfaces and thin films* 38.4 (2006), pp. 215–218. ISSN: 0142-2421 (cited on page 67).

[239] Zineb Matouk et al. “X-ray Photoelectron Spectroscopy (XPS) Analysis of Ultrafine Au Nanoparticles Supported over Reactively Sputtered TiO2 Films”. In: *Nanomaterials* 12.20 (2022), p. 3692. ISSN: 2079-4991 (cited on page 67).

[240] Mengfan Xue et al. “Bipolarized intrinsic faradaic layer on a semiconductor surface under illumination”. In: *National Science Review* 10.4 (2023), nwac249. ISSN: 2095-5138 (cited on page 67).

[241] Shengyang Wang et al. “Positioning the water oxidation reaction sites in plasmonic photocatalysts”. In: *Journal of the American Chemical Society* 139.34 (2017), pp. 11771–11778. ISSN: 0002-7863 (cited on page 68).

[242] Mio Nagamitsu, Kenta Awa, and Hiroaki Tada. “Hydrogen peroxide synthesis from water and oxygen using a three-component nanohybrid photocatalyst consisting of Au particle-loaded rutile TiO 2 and RuO 2 with a heteroepitaxial junction”. In: *Chemical Communications* 56.59 (2020), pp. 8190–8193 (cited on page 72).

[243] Chiheng Chu et al. “Electronic tuning of metal nanoparticles for highly efficient photocatalytic hydrogen peroxide production”. In: *ACS Catalysis* 9.1 (2018), pp. 626–631 (cited on page 72).

[244] Lichao Wang et al. “Simultaneous hydrogen and peroxide production by photocatalytic water splitting”. In: *Chinese Journal of Catalysis* 40.3 (2019), pp. 470–475 (cited on page 72).

[245] Taehyung Lee et al. “Formation of TiO2@ carbon core/shell nanocomposites from a single molecular layer of aromatic compounds for photocatalytic hydrogen peroxide generation”. In: *ACS applied materials and interfaces* 11.44 (2019), pp. 41196–41203 (cited on page 72).

[246] Gun-hee Moon et al. “Solar production of H 2 O 2 on reduced graphene oxide–TiO 2 hybrid photocatalysts consisting of earth-abundant elements only”. In: *Energy and Environmental Science* 7.12 (2014), pp. 4023–4028 (cited on page 72).

[247] Zhaoming Fu, Bowen Yang, and Ruqian Wu. “Understanding the activity of single-atom catalysis from frontier orbitals”. In: *Physical review letters* 125.15 (2020), p. 156001 (cited on page 72).

[248] Georg Kresse and Jürgen Furthmüller. “Efficiency of ab-initio total energy calculations for metals and semiconductors using a plane-wave basis set”. In: *Computational materials science* 6.1 (1996), pp. 15–50. ISSN: 0927-0256 (cited on page 81).

[249] Georg Kresse and Jürgen Furthmüller. “Efficient iterative schemes for ab initio total-energy calculations using a plane-wave basis set”. In: *Physical review B* 54.16 (1996), p. 11169 (cited on page 81).

[250] John P Perdew, Kieron Burke, and Matthias Ernzerhof. “Generalized gradient approximation made simple”. In: *Physical review letters* 77.18 (1996), p. 3865 (cited on page 81).

[251] Georg Kresse and Daniel Joubert. “From ultrasoft pseudopotentials to the projector augmented-wave method”. In: *Physical review b* 59.3 (1999), p. 1758 (cited on page 81).

[252] Peter E Blöchl. “Projector augmented-wave method”. In: *Physical review B* 50.24 (1994), p. 17953 (cited on page 81).

[253] Stefan Grimme et al. “A consistent and accurate ab initio parametrization of density functional dispersion correction (DFT-D) for the 94 elements H-Pu”. In: *The Journal of chemical physics* 132.15 (2010). ISSN: 0021-9606 (cited on page 81).

[254] Ren Wei and Wolfgang Zimmermann. “Microbial enzymes for the recycling of recalcitrant petroleum-based plastics: how far are we?” In: *Microbial biotechnology* 10.6 (2017), pp. 1308–1322 (cited on page 83).

[255] Olubukola S Alimi et al. “Microplastics and nanoplastics in aquatic environments: aggregation, deposition, and enhanced contaminant transport”. In: *Environmental science and technology* 52.4 (2018), pp. 1704–1724 (cited on page 83).

[256] Huayang Zhang et al. “Functional carbon nitride materials for water oxidation: from heteroatom doping to interface engineering”. In: *Nanoscale* 12.13 (2020), pp. 6937–6952 (cited on page 83).

[257] Suljo Linic, Phillip Christopher, and David B Ingram. “Plasmonic-metal nanostructures for efficient conversion of solar to chemical energy”. In: *Nature materials* 10.12 (2011), pp. 911–921 (cited on page 84).

[258] Taylor Uekert, Hatice Kasap, and Erwin Reisner. “Photoreforming of nonrecyclable plastic waste over a carbon nitride/nickel phosphide catalyst”. In: *Journal of the American Chemical Society* 141.38 (2019), pp. 15201–15210 (cited on page 87).

[259] M Caux et al. “Photo-catalytic hydrogen production over Au/gC 3 N 4: Effect of gold particle dispersion and morphology”. In: *Physical Chemistry Chemical Physics* 21.29 (2019), pp. 15974–15987 (cited on page 88).

[260] William M Haynes. *CRC handbook of chemistry and physics*. CRC press, 2016. ISBN: 1315380471 (cited on page 95).

[261] Alexander Weiße et al. “The kernel polynomial method”. In: *Reviews of modern physics* 78.1 (2006), p. 275 (cited on pages 95, 96).

[262] Simão M João et al. “KITE: high-performance accurate modelling of electronic structure and response functions of large molecules, disordered crystals and heterostructures”. In: *Royal Society Open Science* 7.2 (2020), p. 191809. ISSN: 2054-5703 (cited on page 96).

Acknowledgments

The PhD journey was not always easy — there were challenges, but also many rewarding moments. Along the way, I have learned so much, not only in science but also in many other aspects of life. I am truly grateful to everyone who has supported, guided, and encouraged me throughout this journey.

First and foremost, sincere gratitude is expressed to **Prof. Dr. Emiliano Cortés**. Throughout the research, he consistently provided the resources and guidance needed. Every discussion with him sparked new ideas, and his insights during the writing and revision process often added the perfect final touch. His meticulous and timely support during the international exchange and funding applications was invaluable.

Gratitude is also extended to **Prof. Min Liu** for hosting the author during the exchange, providing a platform for experiments, and offering valuable advice. Thanks are also given to **Prof. Junwei Fu** for insightful discussions. The support and companionship of **Yao Tan, Qin Chen, Dr. Jun Wang**, and many other friends are sincerely appreciated. The four months in Changsha were an unforgettable and joyful experience.

Acknowledgment is given to the **E-conversion cluster** for funding the PhD research and supporting the international exchange. The time on the Student Board was both interesting and enjoyable, and organizing the winter retreat with other members was a truly memorable experience.

A heartfelt thank you is extended to the **Committee** for taking the time to read the thesis and for their willingness to participate in the defense despite their busy schedules.

Sincere gratitude is also expressed to the collaborators, **Dr. Simão M. João** and **Dr. Tianfu Guan**. It was a pleasure working together.

A huge thank you is extended to **Everyone in the chair** for fostering such a warm and supportive environment. During difficult times, having people around made things easier, and in happy moments, sharing good news doubled the joy – of course, the cakes helped too!

Special thanks go to **Li Zhu** and **Chenghao Fan** – discussions on projects, casual chats, and travels for conferences and visits were all wonderful experiences. Thanks are given to **Dr. Rui Lin** for his support at the start of the research. Gratitude is also extended to **Christoph Gruber** and **Dr. Simone Ezendam** for their surprising kindness and warmth. Their consideration for those around made me feel much less reserved when I first joined the group. Thanks also go to **Diya Xie, Queqing**

Miao, Jiaqi Chen, and Tao Jiang for being meal companions during the thesis writing period. The many shared meals made the process less stressful. A heartfelt thank you is extended to **Haiyang Hu** for sharing the journey of preparing our thesis.

Special gratitude is extended to **Dr. Wenjie Tian** and **Dr. Huayang Zhang**. Their selfless guidance and insightful discussions not only helped immensely in the research but also demonstrated the kind of passionate, hardworking, patient, and humble scientist that I aspire to become. Deep gratitude is also extended to **Reinhold Rath, Namvar Jahanmehr, Denise Wedemeyer, and Martina Edenhofer** – their assistance with technical challenges and administrative processes was truly invaluable.

To my **Friends**, thank you for your support and encouragement. The fun times we shared made this journey much more enjoyable.

Thank you, **Bailan He**. Having dinner with you after work recharges me and gives me the energy to face each new day. I am grateful to share happiness with you and to have you by my side during difficult moments. Your support means much more to me than you might realize, love you. Thanks also to our cat, Huhu - you brought us so much joy, and I appreciate that you didn't step on my keyboard too often while I was writing my thesis.

Finally, I want to express my heartfelt gratitude to my **Parents** and **Grandparents**. Your unwavering support and encouragement have meant everything to me. Every time we talked on the phone, you asked about not only my life but also the research, somehow making me work faster:) Thank you for encouraging me to go far and see the bigger world. The more I see, the more I appreciate and admire you. I am incredibly lucky to have you. Love you all.